PALEOMAGNETISM OF IGENOUS ROCKS FROM SHATSKY RISE

A Thesis

by

MARGARET PUERINGER

Submitted to the Office of Graduate Studies of
Texas A&M University
in partial fulfillment of the requirements for the degree of

MASTER OF SCIENCE

Approved by:

Chair of Committee,	William W. Sager
Committee Members,	Bradford M. Clement
	Mark E. Everett
	Debbie J. Thomas
Head of Department,	John R. Giardino

May 2013

Major Subject: Geophysics

ABSTRACT

Shatsky Rise is oceanic plateau in the northwest part of the Pacific Ocean, and the formation of Shatsky Rise is poorly known. To get a better understanding of the formation Integrated Ocean Drilling Program (IODP) Expedition 324 drilled five sites: Sites U1347 and U1348 on Tamu Massif, Site U1349 and U1350 on Ori Massif, and Site U1346. Paleomagnetic measurements of the basaltic flows recovered can give insight into the timing and paleolatitude of each site. Relating the change in principle component inclination over depth at each site to the paleosecular variation of the geomagnetic field can better constrain the timing of the eruptions. Measurements were carried out by different sources during IODP Expedition 324 and after. This study is an amalgamation of the results from Sites U1346, U1347, U1349, and U1350. Samples from each site were divided into half and demagnetized using alternating field (AF) demagnetization and thermal (TH) demagnetization. After the drilling overprint was removed most samples displayed univectorial decay in the orthogonal vector plot. AF demagnetized samples displayed a low median destructive field (MDF) behavior, <10 mT, and a moderate MDF behavior, >10-20 mT. Thermal demagnetized samples displayed three behaviors: a rapid decline in magnetic intensity after moderate temperature steps behavior, a linear decline in magnetic intensity behavior, and some samples displayed a small segment of self-reversal at 300°-350°. Using the Cox and Gordon (1984) method Sites U1346, U1347, and U1349 displayed very little variation in principal component inclinations over depth, implying a relatively rapid lava

emplacement of 10^2-10^3 years. Site U1350 display more variation, implying a longer eruptive time frame of 10^4-10^5years. With the assumption of a normal polarity the paleolatitude estimates are -11.0° +22.2°/-21.4° for Site U1346, 11.3° 27.4°/-28.5° for Site U1347, -5.0° +20.8°/-20.6° for Site U1349 and 1.6° ±7.7 ° for Site U1350. The site paleolatitudes imply that Ori Massif (Sites U1350 and U1349) formed at the equator and Tamu Massif (Site U1347) and Shirshov Massif (Site U1346) formed slightly north and south of the equator respectively. All results are consistent with the interpretation that Shatsky Rise formed near the equator.

ACKNOWLEDGEMENTS

I would like to thank my advisor/committee chair, William Sager, and my other committee members Mark Everett, Debbie Thomas, and Brad Clement for helping me through my research and getting me to the place where I am at now. Additional thanks to Bernard Housen, Masahiro Ooga, Claire Carvallo, and Masako Tominaga.

I would also like to thank my family and friends for the support and love they have showed me throughout my time at Texas A & M University.

TABLE OF CONTENTS

LIST OF FIGURES

LIST OF TABLES

CHAPTER I

INTRODUCTION

This manuscript is the total research on the paleomagnetism of the igneous rocks from Shatsky Rise. There are two manuscripts that make up the two chapters of the thesis. The first chapter is a data report for the Integrated Ocean Drilling Program (IODP) looking at the paleomagnetic measurements that were made onshore at the Northwestern Paleomagnetism Laboratory and shipboard *R/V JOIDES Resolution* during IODP Expedition 324. This paper entails the methods of the paleomagnetic analysis of the onshore measurements and finding the principle component inclination, then compiling/comparing with the shipboard results. The second chapter is an amalgamation of the paleomagnetic results and the basaltic magnetic properties of the basaltic flows recovered from Shatsky Rise. This paper calculates and discusses the change in colatitude vs. depth, paleolatitude, and possible eruptive time frame for Sites U1346, U1347, U1349, and U1350. Altogether we hope to provide new data to help understand the formation of Shatsky Rise.

CHAPTER II

MANUSCRIPT #1: DATA REPORT: PALEOMAGNETIC MEASUREMENTS OF IGNEOUS ROCKS FROM SHATSKY RISE EXPEDITION 324

Overview

Integrated Ocean Drilling Program (IODP) Expedition 324 cored five sites on Shatsky Rise, an oceanic plateau, to gain a better understanding of its formation processes. To augment and improve the shipboard paleomagnetic results, an additional 135 samples from Sites U1346, U1347, U1348, and U1350 were measured at the Northwest Paleomagnetism Laboratory at Western Washington University. Samples from all sites were demagnetized using either alternating field or thermal demagnetization in approximately equal numbers. Most samples display a downward-directed overprint likely caused by the drill string magnetic field. This overprint was typically removed by ~10-15 mT alternating field demagnetization or ~300° C thermal demagnetization. Alternating field demagnetization generally worked well to isolate a characteristic remanence direction, with samples mostly showing low (<10 mT) to moderate (10-20 mT) median destructive field values. Thermal demagnetization was also mostly successful in isolating a characteristic remanence at temperatures >350-400°C. Some samples showed small sections of self-reversal during thermal demagnetization. Changes in inclination over depth showed little variation at Site U1346 and U1347, but more variation was recorded at Site U1350. Hysteresis analysis showed

that samples from all sites reside in the single-domain to pseudo-single domain region of the Day plot.

Introduction

Shatsky Rise is an oceanic plateau, which is a large igneous province (LIP) on the Pacific plate that is thought to be the product of a mantle-melting anomaly interacting with a triple junction. It was formed in Late Jurassic to Early Cretaceous time (Sager et al., 1999; Nakanishi et al., 1999). Three volcanic massifs, Tamu, Ori, and Shirshov, and the Papanin Ridge are the major structures of Shatsky Rise (Figure 1.1). Based on magnetic lineations surrounding Shatsky Rise (Fig. 1), the age and volume of the plateau decreases from the Tamu Massif to the Papanin Ridge (Sager et al., 1999).

Since Shatsky Rise volcanism was poorly understood, Expedition 324 cored Shatsky Rise to obtain samples of igneous rocks to better understand its formation. Basaltic lava flows were recovered at four sites (U1346, U1347, U1349, and U1350), whereas volcaniclastic material was recovered at a fifth site (U1348)(Figure 1.1) (Sager et al., 2010; 2011a, 2011b). Prior to Expedition 324, significant basaltic material had been cored only once, at ODP Site 1213 on the south flank of Tamu Massif (Figure 1.1). At this site, basalt from three massive flows was recovered over a 47-m section (Figure 1.2)(Koppers et al., 2010). At Site U1347, which is also on Tamu Massif, a basement section of 159.9 m length produced both pillow and massive flows, but at Site U1348, on the north flank of Tamu Massif, only volcaniclastics were recovered from ~120 m of section (Figure 1.2). Two holes from Ori Massif both yielded basalt flows: thin massive flows from 85.3 m of section at Site U1349 and 172.7 m of pillow and thin massive

flows from Site U1350 (Fig. 2). Site U1346, on Shirshov Massif, yielded a 52.6 m section of pillow lavas with two small massive flows (Figure 1.2).

One of the goals of Expedition 324 is to understand the volcanism that built Shatsky Rise. Paleomagnetic measurements can aid in this understanding because the measured paleomagnetic inclinations give clues about the timing and paleolatitude of eruptions. In this study, the remanent magnetization of igneous rock samples was measured to determine changes in inclination with depth at each site. Changes in remanent inclination versus depth from an igneous section constrain the eruptive time span by the amount of observed geomagnetic field secular variation. The main focus of this report is results from basalt lava flows from Sites U1346, U1347, and U1350. A small number of samples from Site U1348 were measured to see if the hyaloclastite samples from that hole would produce reliable results (they did not). We did not measure samples from Site U1349 because another member of the shipboard party is working on that site. Paleomagnetic analysis for 120 basalt samples was done onboard the *JOIDES Resolution* during Expedition 324. In our data tables, we combine those results with ours for completeness.

Methods

A total of 135 samples were measured in the Pacific Northwest Paleomagnetism Laboratory, which contains a Lodestar Magnetics Shielded Room, at Western Washington University (WWU). All samples were 2 cm x 2 cm cubes cut from the working half of Expedition 324 basalt cores. The magnetic susceptibility was measured on all samples prior to demagnetization, using an AGICO KLY3-S Magnetic

Susceptibility Bridge. Subsequently, the natural remanent magnetization (NRM) was measured in an AGICO JR6 dual speed spinner magnetometer. Because the demagnetization results from some samples of massive flows were erratic in shipboard measurements, samples from massive units were dunked in liquid nitrogen for 20 min 1-4 times to remove overprint magnetizations resulting from multidomain magnetite and hematite. All samples were demagnetized using either alternating field (AF) demagnetization with a DTech D2000 AF demagnetizer or thermal demagnetization in an ASC Model TD48 or ASC Model TD48-SC thermal demagnetizing oven. A vibrating sample magnetometer (VSM), Princeton Measurements Corporation MicroMag Model 3900, was used to produce hysteresis loops on four samples from each site that were judged representative of the site's flow units.

Pilot batches of samples using AF and thermal demagnetization from all sites showed little difference in the efficacy of removing overprint magnetizations, so approximately half of the samples from each site were demagnetized thermally (62 samples) and the other half using AF (73 samples). Initially, thermal pilot samples were separated into two batches of 12 samples, one set being demagnetized in an argon atmosphere and the other natural atmosphere to compare the effects of oxidation. Since there was no difference in the results from the two treatments, the remaining samples were demagnetized in a natural atmosphere. AF demagnetization started at 5 mT with steps of 5 mT up to 60-120 mT. Thermal demagnetization started at 80°C with steps of 40°C to 500°C and steps of 20° - 25°C above 500°C. Complications arose with the JR6 magnetometer with some of the thermally demagnetized samples having magnetizations

too low to measure with this magnetometer above a certain step. If it was not possible to demagnetize a sample past 70% of the original magnetic intensity, the result was not considered a valid measurement of the characteristic remanence.

After samples were demagnetized, the data were analyzed using Remasoft 3.0 software. Equal angle spherical projections, demagnetization intensity plots, and Zijderveld plots (see Tauxe, 1998) were made for each sample. Principal component analysis (PCA) directions (Kirschvink, 1980) were calculated from demagnetization data, typically using higher-level demagnetization steps that trend toward the Zijderveld plot origin. This result is considered the characteristic or primary magnetization for the sample. PCA solutions were calculated both anchored to the origin and not anchored (Tables 1.1, 1.2, and 1.3). VSM hysteresis loops were analyzed with the Micromag AGM-VSM program. A Day plot (Day et al., 1977) was produced using the hysteresis values saturation remanent magnetization (M_{rs})/saturation magnetization (M_s) vs. remanent coercivity (H_{cr})/ coercivity (H_c).

Measurements done during Expedition 324 included AF and thermal demagnetization and bulk magnetic susceptibility measurements recorded during the thermal demagnetization process. Although paleomagnetic work was done on board the ship for all sites, in this report we concentrate only on the data from Sites U1346, U1347, U1348, and U1350. For completeness, we include the shipboard results in our data tables (Tables 1.1, 1.2, 1.3).

Results

Site U1346

A total of 31 samples were measured from Site U1346 cores, but only 29 samples produced good results (Table 1.1). All samples are aphyric basalts from pillow flows. Both AF and thermal demagnetization techniques were used to isolate the primary magnetization. WWU measurements were divided into seven samples measured with AF demagnetization and eight examined with thermal demagnetization. Most samples have a drilling overprint that is removed at ~5-10 mT during AF demagnetization and at ~200° - 300 °C for thermally demagnetized samples. The AF demagnetized rocks show two responses, one type with low median destructive field (MDF), <10 mT, and the other with a higher MDF, >10 mT (Figures 1.3, 1.4). After the drilling overprint is removed the samples usually display univectorial decay to the origin, with a few samples showing erratic behavior at high demagnetizing steps. The samples that show a MDF of <10 mT are >90% demagnetized by 20-30 mT (Figure 1.4), whereas the samples with a MDF >10 mT are >90% demagnetized by 40-50 mT (Figure 1.3). Some thermally demagnetized samples show a small range of temperatures with partial self-reversal at ~300^{o}C (e.g., Doubrovine and Tarduno, 2004; 2005) and/or a large overprint that is removed at ~200^{o}C (Figure 1.5). After removal of the overprint or at temperatures above the self-reversal portion of the demagnetization, most of the samples display univectorial decay to the origin. All thermally demagnetized samples were >90% demagnetized at 450 ° - 500 °C. Of the 15 samples measured at WWU, 13 samples produced good results, judged as samples giving a consistent principal direction that points toward the origin with a maximum angular deviation (MAD) of <10°. The other 16 samples measured

during Expedition 324 showed similar behaviors in both AF and thermal demagnetizations (Sager et al., 2010). Four samples were dunked in liquid nitrogen as a test to determine its effect on sample overprints. There was very little change in the magnetic intensity of the rocks, at most 0.5 A/m (Table 1.4). There were no noticeable effects of the low-temperature treatment on sample behavior during demagnetization.

Sample inclinations calculated using anchored and unanchored PCA solutions showed negligibly different values. The inclinations vary little throughout the length of the cored section, except for one outlier sample with an inclination of 27° (Figure 1.6). Ignoring the single outlier, the average inclination is -21° with a standard deviation of 5.7°. The lack of downhole variation and the low standard deviation imply that the entire section is recording essentially the same magnetic direction, so very little paleosecular variation was recorded and the section was likely erupted in a short period of time.

Site U1347

From Site U1347 cores, 126 samples were measured: 61 during Expedition 324 and 65 at WWU. Only 119 samples produced good results (Table 1.2). The samples are aphyric and plagioclase phyric basalts from massive flows and pillow flow units. To isolate primary magnetization, both AF and thermal demagnetization techniques were applied to different subsets of the samples. At WWU 32 of the 65 samples were demagnetized using AF demagnetization and 33 were demagnetized using thermal demagnetization. The demagnetized samples have varying amounts of drilling overprint. In the AF demagnetized samples, the drilling overprint is typically directed vertically downward (a sign of drill pipe remagnetization (e.g., Fuller et al., 2006)) and is removed after 10-15 mT. For thermally demagnetized samples the overprint is usually removed

progressively up to 310° - 360°C. For both demagnetization types, there were a small number of samples from which the overprint was apparently never removed entirely. Two responses observed with AF demagnetization are samples with low MDF <10 mT and samples with higher MDF >10 mT (Figures 1.7, 1.8). The low-MDF samples are >90% demagnetized at 30 mT (Figure 1.9) and the higher MDF samples are >90% demagnetized at 40-60 mT (Figure 1.8). Once the overprint is removed, most samples display univectoral decay toward the Zijderveld plot origin (Figures 1.7, 1.8). In the lower cores (324-U1347A-25R to 29R), which sampled thick massive flows, sample directions become erratic at AF steps above 50 mT.

The thermally demagnetized samples displayed two different demagnetization behaviors. For one group, the intensity versus temperature curve shows a sharp decline around 300°C. In the other group, a nearly linear decrease in magnetic intensity is seen throughout the measurements (Figures 1.9, 1.10). Some samples showed erratic directions in steps above 520°C, especially samples from cores 324-U1347A-25R to 29R. For a few samples, small partial self-reversal sections occurred in demagnetization steps around 300°C (e.g., Doubrovine and Tarduno 2004; 2005) (Figure 1.11). Typically, the sample increased in intensity for only 1-3 demagnetization steps and the intensity increase was only 10% -15% of the NRM.

Of the samples measured at WWU, 59 of the 65 produced good PCA solutions. Once again, there was little difference between solutions calculated with and without being anchored to the origin. The good results have a MAD of <10° and display a consistent direction after overprint removal. Shipboard AF demagnetization results were

similar, but the thermally demagnetized samples displayed much more erratic behavior. Of the shipboard measurements, characteristic remanence directions for 48 of the 60 with MAD <10° were judged to have produced reliable results (Table 1.2).

Low-temperature treatment was applied to 39 samples at WWU (Table 1.5). The massive flow units had the greatest change in magnetic intensity. Samples that showed a large drop of intensity were dunked more than once to assure full removal of multidomain magnetite and hematite overprints. Since this treatment was used to reduce the effect of overprint acquired by multi-domain magnetic grains, this result implies that multidomain grains contribute significantly to the magnetization of these units. The thin inflation units displayed little change in intensity with low-temperature dunking, implying that they have few multi-domain grains contributing to their magnetization.

Site U1347 characteristic remanence inclinations are mostly low and positive (Figure 1.12). Samples from the top ~15 m of the basement (~160-175 mbsf) and the bottom ~40 m, below ~270 mbsf, show higher scatter than elsewhere, mostly owing to greater scatter in thermal demagnetization results. Samples appear to show at least three groups of inclinations. Between ~175 and 210 mbsf, the average inclination is 20° - 30° and the same is true for the section between ~240 and 270 mbsf. In between, the average inclination appears shallower, ~10° - 15°. Sample inclination scatter is high in the topmost ~15 m and bottom ~40 m, so we cannot tell whether those samples give a significantly different inclination than the middle section without further analysis.

Site U1348

Only five volcaniclastic samples from Site U1348 were measured as a test. Only three samples were strong enough to measure the NRM. Of the three samples, two were measure using thermal demagnetization and one was measured using AF demagnetization. Demagnetization did not produce consistent magnetization directions, so the Site U1348 section was considered unsuitable for further study.

Site U1350

A total of 109 samples were measured from Site U1350 cores: 42 samples were measured during Expedition 324 and 67 were measured at WWU. 102 samples produced good results (Table 1.3). At WWU 33 samples were demagnetized using AF demagnetization and 34 using thermal demagnetization. The AF demagnetized samples showed two responses similar to the previous sites: low MDF, <10 mT (Figures 1.13), and higher MDF, >10 mT (Figures 1.13, 1.14). Both types of samples display univectorial decay after the overprint is removed. The amount of overprint correlates with the MDF. A low-MDF sample typically displays a large overprint, whereas a high-MDF sample displays smaller overprint. The thermally demagnetized samples displayed two behaviors, one with a small partial self-reversal at 300°C (e.g., Doubrovine and Tarduno, 2004; 2005) and one without (Figures 1.15, 1.16). Some thermally demagnetized samples showed erratic behavior above 500°C. There were varying degrees of overprint, but for most samples the overprint did not have a significant effect on the measured direction. After the overprint was removed, samples with both thermal demagnetization behaviors show univectorial decay to the origin. Of the 67 samples, 63 yielded a consistent primary magnetization with a MAD of <10°. As with samples from

other sites, there was no significant difference between PCA solutions using the origin as an anchor and those without an anchor. The 42 samples that were measured during Expedition 324 gave similar AF results, but the thermally demagnetized samples measured on the ship show a much more erratic behavior than those measured at WWU. Results from samples with consistent directional behavior were similar to those measured at WWU. A total of 39 of the 42 samples gave a MAD of <10° and are considered to have produced reliable results (Table 1.3). In all, 32 samples were treated with liquid nitrogen dunking to remove the effects of multidomain grains, but the effects were negligible (Table 1.6).

A plot of inclination versus depth shows that inclinations are all close to zero with slightly negative inclinations being the norm (Figure 1.19). AF and thermal demagnetized sample inclinations give similar values but results from thermal demagnetization are more erratic between ~195 and 235 mbsf. Inclinations at the top and bottom of the hole appear indistinguishable, but the section between ~195 and 235 mbsf may have a more positive average inclination. Because this is also the section with higher scatter, this inference cannot be confirmed without further analysis. It may be that all samples from Site U1350 record the same inclination.

Hysteresis

Hysteresis loops of four samples each from sites U1346, U1347, and U1350 were made with the VSM. All hysteresis loops show rapid saturation of the magnetization with increasing field strength and only a small amount of hysteresis. This type of

response is typical of titanomagnetite grains. On a Day plot (Day et al., 1977) M_{rs}/M_s versus H_{cr}/H_c values for most samples plot in the field that defines pseudo-single-domain behavior (Table 1.7; Figure 1.21). This observation implies that the grains in the samples are either pseudo-single-domain sized grains or a mixture of multidomain and single-domain grains. Samples from Sites U1346 and U1347 display a distribution that is nearly linear from upper left (lower H_{cr}/H_c, higher M_{rs}/M_s) to lower right (higher H_{cr}/H_c, lower M_{rs}/M_s), similar to mixtures of single and multi-domain grains, suggesting that these samples have a simple distribution of similar magnetic grains of different sizes (Dunlop, 2002a, b). The distribution of the Site U1350 samples is not linear, suggesting a more complex set of magnetic grains. In addition, samples from Site U1347 plot farthest toward the upper left, while samples from Site U1346 plot toward the bottom right. This observation implies that single and pseudo-single domain behavior is strongest for Sites U1347 and U1350, whereas the samples from Site U1346 display more influence from multi-domain grains.

CHAPTER III

MANUSCRIPT #2: PALEOMAGNETISM OF IGNEOUS ROCKS FROM SHATSKY RISE AND IMPLICATIONS FOR OCEANIC PLATEAU VOLCANISM

Overview

The eruptive history of Shatsky Rise, a large oceanic plateau in the northwestern Pacific Ocean, is poorly understood. Although some authors concluded that Shatsky Rise volcanic edifices erupted rapidly, there are few solid data to support this conclusion. Similarly, Shatsky Rise is thought to have formed near the equator, but paleolatitude data from the plateau are few. Samples of lava flows were cored from Shatsky Rise at four sites (U1346, U1347, U1349, and U1350) by Integrated Ocean Drilling Program Expedition 324. Paleomagnetic data from these cores are useful for understanding the formation of this large igneous province. Examining changes in paleomagnetic inclinations, we can gain a better understanding of eruptive rates by comparison of observed shifts in inclination with expected paleosecular variation. A total of 362 samples were measured for the four sites and results were grouped by site, flow, and paleoinclination units. At three sites (U1346, U1347, and U1349), little change in paleomagnetic directions were observed, implying that the cored sections were erupted rapidly over periods of 10^2-10^3 years. Only Site U1350 displayed directional changes consistent with significant paleosecular variation, but even this section does not completely average out secular variation, implying that the time span was $<10^4$-10^5 years. On the whole, the paleomagnetic data are consistent with the idea that Shatsky

Rise formed by rapid, voluminous eruptions. Determinations of paleolatitudes are complicated by the low paleolatitude of the sites, which makes unique determination of polarity and hemisphere impossible. Sites U1346 and U1349 both gave consistently negative inclination values while Site U1347 produced positive values and Site U1350 gave both negative and positive inclination groups. We surmise that Sites U1349 and U1350, with the smallest inclination values, were erupted near the paleoequator, whereas Sites U1347 and U1346 were erupted to the south and north of the paleoequator, respectively. Measured inclinations for Site U1347 differ in sign from those reported previously for the igneous rocks cored in nearby Site 1213, implying that these two sites on Tamu Massif record different polarities. With assumptions for polarity, we arrive at paleolatitude estimates of -9.0° +22.2°/-21.4° for Site U1346, 11.3° 27.4°/-28.5° for Site U1347, -5.0° +20.8°/-20.6° for Site U1349 and 1.6° ±7.7 ° for Site U1350. These results are consistent with prior work indicating a near-equatorial paleolatitude.

Introduction

Oceanic plateaus are massive volcanic edifices that represent extraordinary flux of magma from mantle sources (Duncan and Richards, 1991; Coffin and Eldholm, 1994). These large igneous provinces (LIPs) give insight to mantle dynamics and changes in the mantle over time. The formation and evolution of oceanic plateaus is not well known because many are in remote areas beneath the sea and the relation to tectonic setting has been difficult to determine. Most oceanic plateaus were formed during the Cretaceous Normal Superchron making it hard to relate to the details of ridge tectonics and understand the evolution of these volcanic sources (Heller, 1996). Shatsky Rise is

unique among the largest plateaus because it formed during a time of magnetic reversals, allowing a better understanding of its formation.

Shatsky Rise, located in the northwest Pacific Ocean, is one of the largest oceanic plateaus with an area of $4.8x10^5$ km^2 and a total volume of ~$4.3x10^6$ km^3 (Sager et al., 1999). Magnetic lineations around Shatsky Rise indicate that it formed during the Late Jurassic to Early Cretaceous near a triple junction (Fig. 1; Sager et al., 1999; Nakanishi et al., 1999). It is composed of three main edifices: Tamu, Ori, and Shirshov massifs and a low ridge, Papanin Ridge. Apparently the plateau began formation with the eruption of Tamu Massif, the largest and oldest volcano, and the other massifs and ridge formed subsequently along the path of the triple junction (Sager et al., 1999; Nakanishi et al., 1999; Sager, 2005). The volume and age of Shatsky Rise edifices decreases from southwest to northeast along the plateau. From an analysis of the magnetic anomaly over Tamu Massif, Sager and Han (1993) argued that the Tamu Massif formed rapidly during a single reversed polarity epoch.

Shatsky Rise has characteristics that fit two competing hypotheses for oceanic plateau formation. One, the "plume head" hypothesis, posits that oceanic plateaus form from massive eruptions above the head of a nascent mantle plume, having risen from deep in the mantle to the base of the lithosphere (Coffin and Eldholm, 1994). It predicts a massive initial eruption, as may have occurred with Tamu Massif (Sager and Han, 1993). It also predicts waning of volcanism as the plume head becomes exhausted, and this could explain the reduction in volume of Shatsky Rise with decreasing age (Sager, 2005). Another hypothesis is that plateau volcanism can occur in regions of plate

extension, such as mid-ocean ridges, caused by decompression melting of fertile upper mantle (Foulger, 2007). Because it formed at a triple junction, this explanation also could apply to Shatsky Rise (Sager, 2005). To gain a better understanding of the volcanism and formation mechanism of Shatsky Rise, Integrated Ocean Drilling Program (IODP) Expedition 324 cored at 5 sites on the plateau to obtain volcanic material. Site U1346 was cored on Shirshov massif, Sites U1348 and U1347, on TAMU massif, and Sites U1349 and U1350 on Ori massif (Figure 2.1; Sager et al., 2010).

Basaltic flows were recovered at all sites except Site U1348, where only volcaniclastics were recovered (Figure 2.2) (Sager et al., 2010; 2011a, 2011b). The igneous rocks are vesicular aphyric and phyric basalts with MORB-like chemistry and isotopic signatures (Sager et al., 2010). The basaltic flows consisted of pillow basalts and massive flow basalts, the latter up to ~23 meters thick. Prior to Expedition 324, ocean drilling recovered basalt flows at only one other location, Site 1213 on the south flank of Tamu Massif, where a 47-m section consisting of three massive flows was cored (Shipboard Scientific Party, 2002; Koppers et al., 2010). As of this writing, radiometric dating is available only from these flows, which gave an Ar^{40}/Ar^{39} radiometric date of 144.6 ±0.6 Ma (Mahoney et al., 2005).

Pillow lavas and massive flows both occur at most sites, but appear to show a transition from southwest to northeast on Shatsky Rise. Thick massive flows are found only at sites on Tamu Massif where they make up a large proportion of the core. At Site 1213, the entire cored section consists of three massive flows, whereas at Site U1347, the massive flows make up ~67% of the cored section. At this site the massive flows are

concentrated in two sections where they make up ~100% of the rock (Fig. 2) (Sager et al., 2011b). Massive flows were found at some of the other sites, but they are fewer and thinner (Sager et al., 2010). As a result, there is a trend of increasing proportion of pillow lavas in the cored sections moving northeastward.

In this article we examine the paleomagnetism of samples from lava flows cored from Shatsky Rise to gain an appreciation of the timing of the eruptions and the paleolatitude for Shatsky Rise at the time it formed. The basic premise of the eruption timing study is that changes in magnetization inclination of cored samples versus depth provide a record of the changes in the magnetic field caused by paleosecular variation (PSV). PSV occurs at relatively well-known rates (Johnson et al., 2008; Kent et al., 2010), with changes of ~20-30° in magnetic inclination over periods of hundreds to thousands of years. Thus, changes in magnetization direction can be interpreted to reflect the timing of lava flows. The timing of individual lava flows is poorly known because the most precise radiometric dating in these rock types has an uncertainty on the order of 0.5 Ma, so it is unlikely that this method can distinguish the age variation of flows drilled at a single site. Because of the relatively rapid changes in magnetic inclination caused by PSV, paleomagnetic measurements can be used infer the timing of the individual lava flows. Shatsky Rise is a huge volcanic construct with massive lava flows, thus our hypothesis is that the cored igneous sections were emplaced rapidly. If that is true, measured paleoinclinations should show limited variation caused by PSV.

Our motivation for examining paleolatitude is that the Jurassic paleolatitude of the Pacific plate at the time Shatsky Rise formed is poorly known (Sager, 2006) and thus

new information is important for understanding Pacific tectonic history. Prior paleomagnetic studies indicate that Shatsky Rise formed near the equator (e.g., Sager et al., 2005; Sager, 2006), but Pacific paleomagnetic data are sparse and the apparent polar wander path is poorly defined, especially for the Late Jurassic and Early Cretaceous (Sager, 2006). As a whole, Shatsky Rise took ~21 Myr to form (Nakanishi et al., 1999), so changes in paleolatitude along the plateau are expected.

Because IODP Expedition 324 was a large collaborative effort, parts of the study were done at different sites by different investigators. Here we amalgamate results from several different sources.

Prior Paleomagnetic Studies from Shatsky Rise

Prior to Expedition 324, the only paleomagnetic studies done for Shatsky Rise igneous basement rocks were from Site 1213, where 3 massive basaltic flows were cored (Koppers et al., 2010). 52 samples were measured using AF demagnetization and thermal demagnetization to isolate the primary magnetization (Tominaga et al., 2005). The study showed that many samples from the Site 1213 massive flows produced poor results and the data set as a whole showed relatively high scatter between characteristic magnetization inclinations for different samples. No statistical difference was detected between the mean inclinations of the three eruptive units, suggesting that the eruptions occurred within a short time period. The mean inclination for the site is -9.3° +27.5°/-41.8° (Here and elsewhere, we report 95% confidence limits, which are asymmetric for azimuthally-unoriented samples, see Cox and Gordon (1984)) and this was interpreted as recording eruption slightly north of the equator during a reversed polarity period

possibly correlating to chron M19 on the geomagnetic polarity time scale (Tominaga et al., 2005). Paleomagnetic data were also measured from Early Cretaceous sedimentary rocks deposited atop the igneous basement at Site 1213 (Sager et al., 2005). Data from 22 samples gave a mean paleolatitude of 4.6° +7.2°/-6.9°, which was interpreted as a reversed magnetization acquired in the southern hemisphere. In addition, paleomagnetic samples were measured from a ~100 m section of basalt flows cored from abyssal seafloor at Site 1179, located slightly north of Shatsky Rise (Sager and Horner-Johnson, 2004). The 122 measured samples described 13 independent magnetic groups that indicate a paleolatitude of 1.9° N ±6.8°. Among the important findings of these studies is the fact that Shatsky Rise formed near the equator.

A recent study of magnetic log data from within the borehole of Site U1347 interpreted a change in the sign of the magnetic anomaly in the lower part of the section. The authors take this observation to imply a shift of paleoinclinations from positive to negative in the lower part of the Site U1347 section. This change was interpreted as the result of TAMU Massif moving from the southern hemisphere to the northern hemisphere (Tominaga et al., 2012).

Expedition 324 Measurements Overview

Paleomagnetic measurements were made onboard the D/V *JOIDES Resolution* during Expedition 324 at all cored sites (U1346-U1350). A total of 163 samples were measured during the cruise (Sager et al., 2010). These data are preserved in the IODP SEDIS database (www.iodp.org/access-data-and-samples). Subsequently, 135 samples were measured at Western Washington University from Sites U1347, U1348, and

U1350. In addition, 64 samples from Site U1349 were measured at Doshisha University. Data from these studies are recorded as data reports in the IODP Proceedings (Pueringer et al., in press; Pueringer, M., M. Ooga, and W. Sager, Data report: Paleomagnetism of basalt samples from Expedition 324 Site U1349, Ori Massif, Shatsky Rise, in preparation). Among the findings from these preliminary studies, samples from the Site U1348 volcaniclastic section were found to produce unreliable results, so this site is not considered further. Magnetic measurements were also made by C. Carvallo (Carvallo et al., 2013a, 2013b, both in press) for the purpose of determining paleointensity. Magnetic properties were measured for ~60 samples from Sites U1347, U1349, and U1350 to determine sample suitability for paleointensity study (Carvallo et al., 2013a; 2013b, both in press). These two studies were useful for an understanding of magnetic properties, but did not produce useful paleoinclination measurements that could be used in our study.

Shipboard Measurements

During Expedition 324, samples from every site were measured for paleomagnetic vector data, using both AF and TH demagnetization (Sager et al., 2010). To monitor changes in magnetic mineralogy, bulk susceptibility measurements were made between steps using a Kappa Bridge KLY 4S (geofyzika Brno). AF demagnetization was performed with a D-tech demagnetizer in 2-5 mT steps up to 30 mT and 10-20 mT steps after 30 mT. TH demagnetization was performed in a Schoenstedt Thermal Demagnetizer (model TSD-1) in steps of 25-50 °C up to 500-600 °C. After each step for both AF and TH demagnetized samples, the NRM was measured on a Molspin Minispin magnetometer or on a 2G cryogenic magnetometer (Sager et al.,

2010). The results from Sites U1346, U1347, and U1350 were reported in the IODP Proceedings and are combined here with our shore-based results.

Doshisha University Measurements

M. Ooga measured samples from Site U1349 at Doshisha University (see Pueringer et al., in prep.). The 8 cm^3 cubic samples were cut into 8 specimens and demagnetized using both AF and TH demagnetization. 31 samples were divided into sets of two subsamples, with one of the two demagnetized using AF demagnetization and the other using TH demagnetization. The AF demagnetized samples were demagnetized on a 2G Enterprise 755R demagnetizer in steps of 5 mT from 5-50 mT and steps of 20 mT up to 100 mT. Thermally demagnetized samples were demagnetized on a TDS-1 (Natsuhara Giken) oven in steps of 25-30 °C up to 700 °C. The resulting inclinations from each sample set were close, so in our analysis, each of these 62 paleocolatitudes is the average of the two primary magnetizations determined from both AF and TH demagnetization of subsamples. Of the remaining 3 singular measurements, 2 were demagnetized using AF and the other was TH demagnetized.

Western Washington University Measurements

Onshore measurements for Sites U1346, U1347, and U1350 were made in the Pacific Northwest Paleomagnetism Laboratory in a Lodestar Magnetics Shielded Room, at Western Washington University. The samples were measured for magnetic susceptibility on an AGICO KLY3-S magnetic susceptibility bridge and then the natural remanent magnetization was measured on an AGICO JR6 dual speed spinner magnetometer. Half of the samples were demagnetized using thermal demagnetization

and the other half using AF demagnetization, because it was still unclear after the shipboard study which method produced better results. For samples being TH demagnetized, pilot batches were heated and cooled in an argon atmosphere (so that oxidation of the samples would be minimized) and a regular atmosphere, using an ASC Model TD48 or an ASC Model TD48-SC thermal demagnetizing oven. No significant difference in result from these two techniques was detected, so the rest of the samples were TH demagnetized in air at steps of 40° C from 80° to 500°C and steps of 20-25°C above 500°C. The AF demagnetized samples were demagnetized with a DTech D2000 AF demagnetizer at steps of 5 mT from 5 mT to 60-120 mT. Hysteresis loops from 4 samples from each site were done with a Vibrating Sample Magnetometer (VSM), Princeton Measurements Corporation MicroMag model 3900 (Pueringer et al., in press).

Because there was concern that high scatter in shipboard measurements of Site U1347 massive flows resulted from multidomain magnetic grain behavior, all samples from the massive flows were subjected to low-temperature (77 K) treatments. The samples were dunked in liquid nitrogen for 20 minutes then warmed to air temperature and measured. This low temperature procedure was performed before the samples were demagnetized and the process of dunk, warm, then measure was repeated until there was little change in magnetic intensity after exposure to the liquid nitrogen. Low temperature treatment helps remove the magnetic remanence of multidomain magnetic minerals (Dunlop and Özdemir, 2007). The low temperature treatment appeared to help reduce the scatter for TH demagnetized samples; thus, these massive-flow samples may contain a mixture of SD, PSD, and MD grains (Pueringer et al., in press) with enough MD

behavior to cause magnetization instability and thus give inconsistent magnetization measurements during demagnetization measurements.

Most samples from Sites U1346, U1347, U1349, and U1350 displayed a downward-directed, drill-string overprint (e.g., Audunsson and Levi, 1989), but this bias was removed at 10-15 mT for alternating field (AF) treated samples and 150-250 °C for thermally (TH) demagnetized samples. Both AF and TH demagnetization gave reliable results for most of the samples; although, results were least consistent for Site U1347. Samples showed diverse demagnetization behaviors due to variations in magnetic mineralogy and oxidation state. AF demagnetized samples displayed low (<10 mT) to moderate (>10 mT) median destructive field (MDF) values and were mostly characterized by univectorial decay toward the origin on a Zjiderveld (orthogonal vector) plot. Some of the samples from Sites U1346, U1347, and U1350 showed a small segment of self-reversal behavior at ~300-350 °C during TH demagnetization. This type of behavior is not uncommon in seafloor basaltic flows (e.g., Doubrouvine and Tarduno, 2004; 2005). The reversed directions were removed by higher temperature demagnetization and we were able to use these higher temperature steps to determine the characteristic magnetization direction. Some basalt flow samples showed an increase of magnetic susceptibility at higher TH demagnetization steps, a behavior implying the inversion of titanomagnetite to magnetite during heating (Özdemir and O'Reilly, 1982). The transformation did not appear to change magnetization direction, so the newly formed magnetite appears to inherit the magnetization direction of the original magnetic minerals (Carvallo et al., 2013a, in press; Pueringer et al., in press).

For our vector analyses, all sample characteristic magnetization inclinations were calculated using principle component analysis (PCA) (Kirschvink, 1980; Pueringer et al., in press; in prep.). As a part of this calculation, the maximum angular deviation (MAD) of each sample was determined. The MAD can be used as an indicator of sample magnetization repeatability during demagnetization measurements and data with large values of MAD can be rejected as unreliable. In our analysis, we used MAD = 10° as an upper limit for reliable sample directions. Approximately 24% of the results from Site U1347 were rejected by this criterion. About 2% of the samples from Site U1350 were eliminated for the same reason. However, no samples from Site U1346 and U1349 were eliminated because of large MAD.

Shatsky Rise Basaltic Magnetic Properties

An array of measurements and observations were made on sample subsets from Sites U1346, U1347, U1349, and U1350 by different members of the author team in an effort to characterize the magnetic mineralogy. Standard hysteresis measurements were made on 12 samples from Sites U1346, U1347, and U1350 by Pueringer et al. (2013, in press). Similar hysteresis measurements were made on an additional 60 samples from the same sites plus Site U1349 by Carvallo et al., (2013a, b, both in press). These data give clues about the type of magnetic minerals and their grain size. First-Order Reversal Curve (FORC) diagrams, another type of hysteresis measurement, were made for samples from Sites U1346, U1349, and U1350, to provide a better understanding of magnetic grain size and grain magnetic interaction (Carvallo et al., 2013a, b, both in press). Susceptibility curves in high and low temperatures were measured on samples

from Sites U1347, U1349, and U1350 to understand the magnetic mineral types. In addition, SEM observations were made on thin sections from Sites U1347, U1349, and U1350 (Carvallo et al., 2013a, b, both in press).

Magnetic grains observed in thin section range from 1-2 microns to several tens of microns across, but in samples from Sites U1347 and U1350 the larger grains have been subdivided by alteration into micron-scale grains (Carvallo et al., 2013a, in press). Samples from Sites U1347 and U1350 contain skeletal grains typical of alteration whereas Site U1349 samples contain unbroken and little altered grains. Magnetic grain size determined from the hysteresis and FORC diagram measurements indicate that most samples have grain sizes in the single domain (SD) or pseudo single domain (PSD) range, which is consistent with thin section observations (Carvallo et al., 2013a in press). Hysteresis measurements of samples from Sites U1346 and U1347 are in the PSD range, which could also indicate a mixture of SD and multidomain (MD) grains (Pueringer et al., in press; Day et al., 1977). Thus, from hysteresis and SEM observations, the samples can be characterized as having titanomagnetite grains with a variety of sizes ranging from SD to PSD. Such magnetic grains are usually reliable paleomagnetic recorders.

Low and high-temperature heating/cooling measurements indicate a variety of behaviors from reversible to highly irreversible. Curie temperatures of magnetic grains range from low (~160 °C) to high (550-575 °C), but the most common values are 400-500 °C. This variability suggests that the samples contain a complex mixture of magnetic grains and phases. The thermal magnetic measurements are consistent with

titanomagnetite with varying Ti content and variable oxidation states (Carvallo et al., 2013a, b, both in press).

Methods

For the WWU demagnetization measurements, principal component analysis (PCA) directions (Kirschvink, 1980) were calculated using Remasoft 3.0 software. For each sample, a series of high temperature or high AF field measurements that displayed univectorial decay toward the origin of an orthogonal vector plot (Zjiderfeld plot) was assumed to represent the primary magnetization and used for the PCA determination. PCA directions from the shipboard and Doshisha University studies were compiled as calculated by the authors. For the WWU samples, PCA line fits were calculated both anchored to the origin as well as unanchored (Pueringer et al., in press). Only anchored results were calculated by the other authors. The difference between anchored and unanchored solutions for most samples was observed to be small, so the choice of PCA solution type does not significantly affect the results. Because some samples displayed short sections of partial self-reversal at medium temperature levels (300-350°C) during TH demagnetization, only the measurements at higher temperatures were used for the PCA calculations. For AF-treated samples and TH-treated samples that did not show a self-reversal segment, a number (typically N>4-5) of high demagnetization steps were chosen for the solution (Pueringer et al., in press).

Anchored PCA paleoinclination values for the samples were interpreted using the Cox and Gordon (1984) routine. Because Cox and Gordon recommended using paleocolatitude values for the analysis (rather than paleoinclinations), paleocolatitude

values are shown in this study. Mean paleocolatitudes were calculated for individual lava flows (when possible) or for flow groups having similar inclinations. When possible, outlier measurements were rejected from unit mean paleocolatitude calculations to reduce the uncertainty of the mean. Outliers were characterized as measurements that were outside two standard deviations of the unit mean, calculated without including the outlier value. Outlier paleocolatitudes are marked in gray in Figures 3-6. Adjacent flow unit and flow group means were tested to see if they are statistically distinct using the Z-statistic (Kono, 1980). If they were not distinct, then they were grouped together and tested relative to other adjacent units. Based on the unit means, the average colatitude and its uncertainty were calculated for each site using the statistics of Cox and Gordon (1984). This method is one of several developed for analysis of azimuthally-unoriented paleomagnetic data and the results of the different methods are comparable. Rather than take each statistically-distinct group of flows as an independent measurement of the paleofield, Cox and Gordon (1984) recommended combining groups with similar mean paleocolatitudes and only assuming that groups are independent if group mean paleocolatitudes are separated by ~5-10°. Their reasoning is that magnetic field values are only independent if enough time passed for significant secular variation to occur. In addition, Cox and Gordon (1984) address the problem of underestimating the uncertainty of the mean paleocolatitude for a site when a small number of independent units are sampled. Their method substitutes a model value of between-flow variance for the observed variance when the observed variance is small. This routine also includes an

estimate of the potential systematic error caused by the unknown off-vertical tilt of the borehole.

Results

Site 1346

Sample measurements from Site U1346 show a narrow range of colatitude values, from ~95-105° (Figure 2.3), based on small magnitude negative paleoinclinations and the assumption that the samples are normally magnetized (for simplicity, we make the arbitrary assumption that the magnetization is normal for all sites). No change in the sign of the paleoinclinations is observed, so all of the samples record the same polarity. Based on the distribution of the colatitudes and the flow units described by shipboard scientists (Sager et al., 2010), the igneous section was divided into four different sections for colatitude analysis. Statistical analysis showed that only two units are statistically distinct and the difference in average colatitude is small, ~3.1° (Figure 2.3; Table 2.1). This small difference implies little change in the magnetic field direction between flow groups, so it is unlikely that significant time passed between the groups. By the rationale described in Cox and Gordon (1984), we combine the two units into a single unit average. The average colatitude for the site is 101.0 ° with a 95% confidence of +22.2°/-21.4° (Figure 2.3; Table 2.1).

Site 1347

Sample paleoinclinations from Site U1347 samples are predominantly positive, giving unit mean colatitudes ranging from 73.2-82.5° (normal polarity assumed). Interestingly, the paleoinclinations from nearby Site 1213 are all negative and about the

same magnitude (Tominaga et al., 2005). The simplest explanation is that the two sites record different magnetic field polarities.

Six statistically distinct flow groups were calculated within the cored section (Figure 2.4). Differences between-flow group mean colatitudes range from 2.9-8.0° with the largest changes between groups 2 and 6 and adjacent groups. Although we could divide the section into four separate groups (1, 2, 3-5, 6), within-group colatitude variance is high and implies that these groupings may not represent truly independent measurements of the paleofield. Because of the large scatter and low inter-group mean variation, we take a conservative approach and combine all results into a single unit average. The amount of paleocolatitude change between units is small, implying that the sampled paleofield did not undergo significant secular variation. The average colatitude is 78.6° with a 95% confidence of +27.4°/-28.5° (Figure 2.4; Table 2.1). The large uncertainty of the mean is due in part to the assumption of a single magnetic group and also the large measurement scatter, particularly in the bottom unit (standard error 17.4°). The uncertainty can be reduced somewhat by omitting the results from the lowest flow, which have the greatest scatter. Without this unit, the average colatitude is 79.9° with a 95% confidence interval of +24.0/-24.6°.

Site 1349

Measured paleoinclinations for Site U1349 were mostly small negative values, implying magnetization in the southern hemisphere if the polarity is normal. Statistical analysis indicates that Site U1349 has two distinct groups, which give two mean colatitudes at 92.4° and 97.4°, implying a paleolatitude near the equator (Figure 2.5;

Table 2.1). The difference between the unit means colatitude is only 5°. The difference is small, so we combined both groups into an overall mean for the section. The small difference between the two groups implies that a short time separated the two because the magnetic field did not change by much. The mean colatitude for the site is 95.0° with a 95% confidence interval of +20.8°/-20.6° (Figure 2.5; Table 2.1).

Site 1350

Site U1350 is unusual among Expedition 324 sites because the cored section displays both positive and negative inclinations in nearly equal amounts. To interpret the section, we have to make an assumption about magnetic polarity. We think it unlikely that the section records numerous magnetic reversals; instead, the pattern of paleocolatitudes (Figure 2.6) appears much like published secular variation curves, especially between 170-270 mbsf where mean colatitude values change systematically. Thus we assume that changes in the sign of the paleoinclination result from secular variation. After statistical analysis, Site U1350 was divided into 14 statistically distinct groups (Figure 2.6; Table 2.1). Differences between group means are larger than at other sites, ranging from 0.9-12.0°, with a median difference of 6.0°. Changes are small between colatitudes for groups 3 and 4 as well as 11-14, so we combine these groups. Our final grouping has 10 independent units. From these 10 groups, we obtain a mean site colatitude of 88.4° with a 95% confidence interval of ±7.7 (Figure 2.5; Table 1). In this case, the confidence limits are symmetric because the paleocolatitude is near 90° and the magnitude of the uncertainty is much less because of the assumed 10 independent groups.

Discussion

Because of PSV, magnetic field directions are constantly changing. Periods of little change, such as those we observe between Shatsky Rise lava flows, are rare if much time has passed. Jurassic geomagnetic field behavior is poorly known, so in this discussion we must assume that Jurassic PSV was similar to the recent record. As shown by deep sea and lake sediment cores (which can produce high resolution records) recent PSV displays multiple shifts of paleoinclination during the Holocene (e.g., Creer, 1981; Turner and Thompson, 1981; Gorgoza et al., 2011), with swings of up to 15-30° in 1 kyr (Creer, 1981; Daly and Le Goff, 1996; Lund et al., 2005). Some records suggest that inclination changes can be very rapid, e.g., 6° over a 50 year span (Gorgoza et al., 2011). In the last 5 kyr, sediment records often show 4-6 swings >10° (Creer, 1981). Inclinations in sediment records can remain stable for a time, but it is rare to find periods >500-1000 years in which the field changes <5° (Lund et al., 2005).

Of all the Shatsky Rise sites, Site 1213 shows the least variation. Although the individual sample data show much scatter, all of the flows in this 47-m section seem to record the same inclination. Sites U1346 and U1349 are alike because they both show only two distinct groups with averages 3° and 5° apart, respectively. The recent PSV records suggest that the longest periods of small PSV change (<5° colatitude) are ~500-1000 yr, so we hypothesize that the cored sections of Sites 1213, U1346, and U1349 erupted in periods <100-1000 years because of the small change between magnetic groups. Site U1347 shows a bit more variation, but not much. Groups 1 and 3-5 all have closely similar averages of 78.3-82.5°, which suggests little PSV. Groups 2 and 6 depart

slightly from average, but not by much. Groups 2 and 6 both have larger uncertainties because group 2 has only a few samples and group six shows a large amount of scatter. Thus one explanation is that the observed differences are simply random scatter in measurements. The change of direction between units shows no systematic trend as might be expected for secular variation recorded by successive flow groups. It is thus plausible that all of these flows record essentially the same paleoinclination and thus only a small amount of time passed in between flows (e.g., <100-1000 years). The six group means have a standard deviation of 3.7° (2.7° without the bottom unit), which is much less than the 9.4° expected from field models (Cox and Gordon, 1984). Thus secular variation has not been averaged. From the results of Sites 1213, U1346, U1347, and U1349, we surmise that most lava flow emplacement at Shatsky Rise sites occurs rapidly. The rapid eruption is similar to the Deccan Traps eruptions, where single eruptive events are 40-180 m thick with very little paleoinclination variation (Chenet et al., 2008).

Site U1350 is the different site. Both the top ~40 m and bottom ~50 m of the section show consistent colatitudes, implying rapid lava accumulation, but the middle section, between ~190-270 m, shows large systematic variations with the appearance of PSV. Differences between flow groups in this middle section are typically 6-7° with an overall range of ~15° (78.2-94.3°). It seems that more time has passed in this ~173-m section than at other sites. Even with the observed variation, the between-flow standard error is only ~4.9°, which is less than the expected 9.0° from a PSV model (Harrison, 1980; from Cox and Gordon, 1984). These observations imply that the elapsed time is on

the order of 10^3-10^4 years, but probably not on the order of 10^5 years, which would average out PSV and record the full range of inclination variation. All together we conclude that Shatsky Rise lava sections build rapidly, but at some locations on the flanks of some edifices (i.e., Site U1350), significant time can pass between lava flows. At Site U1350, there are sections that show rapid accumulation and sections that appear to take longer, implying pulses of greater and lesser lava output. Similar observations are made on Hawaiian volcanoes where summit eruptions can emplace a thick section in a short time but flank flows are erupted with greater time gaps in between (Stopler et al., 2009; Sharp et al., 1996).

The paleolatitudes of all the sites put Shatsky Rise near the equator at the time of its formation. Before interpreting these data, we must note that the uncertainty of the mean paleolatitudes is high. This is largely a result of the small number of independent magnetic units for all sites but U1350. The Cox and Gordon (1984) analysis places a floor of ~9° for the standard error of the mean (implying ±18° 95% confidence interval). Additional uncertainty from measurement errors and off-vertical tilt expand the 95% confidence interval. As a result, the 95% uncertainty for paleocolatitudes for Sites U1346, U1347, and U1349 is 21°-27°. Such large uncertainties make unique interpretations difficult. In addition, because of the low paleolatitudes, we cannot make a unique interpretation of magnetic polarity, which also complicates interpretations about paleolatitude. We can propose a plausible interpretation, but it must be based on assumptions about polarity and hemisphere and other information.

Pacific plate paleomagnetic data indicate that since Early Cretaceous time (~123 Ma), the Pacific plate has drifted northward by ~40° (Sager, 2006; 2007). This amount of drift suggests that Shatsky Rise (currently at 30-38° N latitude; Fig. 1) traveled to its current site from slightly south of the equator. Prior to that time, Pacific paleomagnetic poles are uncertain, but evidence suggests 10-15° of southward motion from late Jurassic to Early Cretaceous time (Larson et al., 1992; Larson and Sager, 1992; Sager, 2006). In contrast, a model of Pacific plate motion relative to the hotspots (Wessel et al., 2006) implies that the Pacific plate had little latitudinal motion prior to ~100 Ma (Sager, 2007). Thus it is possible that Shatsky Rise formed slightly south of the equator and simply drifted northward or it is possible that it formed north of the equator and drifted southward during the Late Jurassic and Early Cretaceous before turning back to the north at ~123 Ma.

From our paleomagnetic data, Ori Massif seems to have formed nearest the equator. Site U1349 samples have mostly shallow negative inclinations, giving a paleolatitude of -5.0° and U1350 has samples with mostly shallow positive inclinations that give a paleolatitude of 1.6° (assuming normal polarity for both). The difference between the two sites at Ori massif is negligible due to the large standard error for both paleocolatitudes, so this puts Ori Massif at the equator at the time of eruption. Because of the shallow inclinations, this observation is true even if we assume that either section is reversed polarity instead. Site U1346, on Shirshov Massif, gave consistently negative paleoinclinations, which indicate a paleolatitude of -11.0° assuming a normal polarity. The two sites on Tamu Massif, 1213 and U1347, gave nearly equal inclinations but with

different signs. Again assuming normal polarity, the paleolatitude of Site U1347 is 11.35° and that for Site 1213 is -4.5° (Tominaga et al., 2005). Although it is possible that a long time passed (millions of years – enough for ~15° of latitudinal drift) in between the eruption of these two sequences, a simpler explanation is that the two sites recorded different magnetic polarity periods. This interpretation still requires the passage of time, but not so much. If this interpretation is correct, then the conclusion of Sager and Han (1993) that Tamu Massif formed entirely during one period of reversed polarity is incorrect.

Tominaga et al. (2012) concluded that Tamu massif drifted from the southern hemisphere to the northern hemisphere during the formation of the Site U1347 section because the vertical component of the magnetic field measured by downhole logs changes at a depth of ~260 meters below sea floor (mbsf). They correlated paleoinclinations from the lower sections of Site U1347 to Site 1213. We measured paleoinclinations within the Site U1347 section that are consistently positive, which is at odds with the interpretations of Tominaga et al. (2012). Our data imply that the entire Site U1347 section formed in the same hemisphere. We interpret the difference in paleoinclination sign between Sites 1213 and U1347 as a change in polarity without the necessity of significant tectonic motion in between. Tominaga et al. (2012) also concluded that the entire section is normally magnetized, based on the sign of the vertical magnetic field in the borehole. This conclusion seems plausible and implies that the Site 1213 lava are reversed in magnetic polarity.

Figure 7 shows colatitude arcs for Sites U1346, U1347, U1349, and U1350 compared with Pacific paleomagnetic poles. Sites U1349 and U1350, on Ori Massif, show little distinction between reverse and normal polarity, implying a formation at the equator. The normal polarity colatitude arc for Site U1347, Tamu Massif, is more consistent with Pacific paleomagnetic data, which would put it in the northern hemisphere at the time of formation. This also coincides with the normal polarity interpretation based on magnetic logging data (Tominaga et al., 2012). For Site U1346, Shirshov Massif, a reversed polarity is more consistent with Pacific paleomagnetic data, implying that it formed in the northern hemisphere as well. The uncertainties on these paleocolatitudes are large enough that these inferences are weak.

Because the actual polarity of our igneous samples is unknown, we must make assumptions about the paleoposition of Shatsky Rise in order to interpret paleolatitudes and magnetic polarity. Currently, Site U1346 is 1.8° north of Ori Massif, whereas Sites 1213 and U1347 are 4.5° and 3.6° south of Ori Massif. Ori Massif formed at the equator, so if Shatsky Rise had little latitudinal motion during its formation, we could interpret the Shirshov Massif paleomagnetic data as reversed polarity formed slightly north of the equator. Further, we would interpret the Tamu Massif Site U1347 samples as reversed polarity, formed slightly south of the equator and the Site 1213 samples as recording a normal polarity at the same location. However, the latter interpretation is the opposite of that implied by the magnetic logging data (Tominaga et al., 2012). It is also possible that Shatsky Rise drifted 10-15° southward during its formation. If the Jurassic paleomagnetic pole of Larson and Sager (1992) is correct, Shatsky Rise has drifted ~30°

northward since its formation at ~145 Ma, which would imply that Tamu Massif formed slightly north of the equator. That interpretation further implies that the Site U1347 lava flows acquired their magnetizations in the northern hemisphere during a normal polarity period, but Site 1213 flows were magnetized during a reversed polarity period. The near-equatorial results from Site U1349 and U1350 indicate that Shatsky Rise reached the equator by the time it formed. In this scenario, Site U1346 lavas would be magnetized during a normal polarity period, slightly south of the equator prior to the turnaround in drift.

A problem with all of our interpretations, as mentioned above, is that the uncertainties of all paleolatitudes are large owing to the small number of units sampled. Our interpretations of the polarity and paleolatitudes at each of these sites are merely a plausible scenario. The Site U1350 paleocolatitude is much better constrained, because it is based on 10 independent flow groups.

Conclusions

(1) Samples from Sites U1346, U1347, and U1349 did not display substantial colatitude variation between units, implying that the cored sections were erupted during a short period of time, i.e., <100-1000 years. The Site U1350 section is the only one that displays significant and systematic variation between flow units that could be interpreted as PSV. This finding implies emplacement over a period of >1000 years. However, the between-unit standard error for Site U1350 is smaller than modeled variation, implying

that the total eruptive period was too small to completely average PSV and is thus $<10^5$ yr.

(2) Sites 1213 and U1347A are both on Tamu Massif and give paleoinclinations of similar values but different signs. We interpret that a reversal occurred between the formations of the two sites. This contradicts published findings that Tamu Massif formed during a single polarity period.

(3) Sites U1349 and U1350 have site paleolatitudes of -5.0° and 1.6° implying that Ori Massif formed at the equator.

(4) If we assume that Shatsky Rise drifted southward before turning around at ~123 Ma, then Site U1347 flows (Tamu Massif) formed in the northern hemisphere during normal polarity, Site 1213 flows (Tamu Massif) were erupted at the same location during reversed polarity, and Site U1346 flows (Shirshov Massif) formed in the southern hemisphere during normal polarity. Alternate polarity interpretations for Sites 1213, U1346, and U1347 can be made, assuming that the north-south component of tectonic drift was negligible for Shatsky Rise during its formation, but this infers a polarity for the Site U1347 section that is at odds with those made from magnetic logging data.

CHAPTER IV

SUMMARY AND CONCLUSIONS

To get a better understanding of the formation of Shatsky Rise, and oceanic plateau located in the northwestern Pacific Ocean, IODP Expedition 324 drilled 5 sites. Two sites were corded on Tamu Massif (U1347 and U1348), two sites on Ori Massif (U1349 and U1350), and one site on Shirshov Massif (U1346). Paleomagnetic measurements were performed shipboard during the Expedition and onshore afterward to get a better constrain the timing and paleolatitude of the eruptions. Timing of the eruptions will be related to the PSV of the geomagnetic field, where changes of 20-30° magnetic inclination can occur over 100-1000s of years. Basaltic flows were recovered at all sites except Site U1348, where only volcaniclastics were recovered. The basaltic flows consisted of pillow basalts and massive flow basalts that had magnetic minerals consistent with titanomagnetite ranging in the single to pseudo-single domain range. Results from paleomagnetic measurement from Site U1348 were not reliable and were not interpreted in this study. This study was an amalgamation of results from different sources.

Samples from each site were divided into half and demagnetized using AF and TH demagnetization. AF demagnetized samples displayed two different behaviors: a low MDF behavior of <10 mT and a moderate MDF behavior of 10-20 mT. TH demagnetized samples displayed three different behaviors: a rapid decrease in magnetic intensity after moderate temperature steps, a more linear decrease in magnetic intensity

throughout the demagnetization process, and some samples displayed a segment of self-reversal behavior at 300-350° C. Using the PCA, characteristic magnetic inclinations were calculated. Individual flow units were calculated from sample colatitudes using the Cox and Gordon (1984) method. Site paleolatitudes were calculated (assuming normal polarity) from statistically distinct flow units at each site.

Site U1346 on Shirshov Massif displayed two distinct flow units and had a site paleolatitude of -11.0° +22.2°/-21.4°. Site U1349 on Ori Massif displayed two distinct flow units with a site paleolatitude of -5.0° +20.8°/-20.6°. Site U1350 on Ori Massif display 14 distinct units with a paleolatitude of 1.6° ±7.7 °. Site U1347 on Tamu Massif displayed 6 distinct units with a paleolatitude of 11.3° 27.4°/-28.5°. Site 1213 from a different study was also drilled on Tamu Massif and had a paleolatitude of -4.5°. The difference of the paleolatitude signs at the siteson Tamu Massif was interpreted as a reversal in the magnetic field in-between the formation of the sites. Sites U1346, U1347, and U1349 had little variation between flow units, which implies a rapid eruptive time frame of <100-1000 years. Site U1350 displays more variation between flow units, which implies a longer eruptive time frame of 10^3-10^4 years. Due to the low latitudes of the measurement unique interpretations of polarity cannot be made, but based off the paleolatitude and colatitude arcs of Sites U1350 and U1349, imply that Ori Massif formed at the equator and Tamu Massif (Sites U1347 and 1213) and Shrishov Massif (Site U1346) formed north and south of the equator respectively.

REFERENCES

Audunsson, H., Levi, S., 1989, Drilling-induced remanent magnetization in basalt drill cores: Geophysical Journal International, v. 98, p. 622–623.

Beaman, M., Sager, W. W., Acton, G. D., Lanci, L., and Peres, J., 2007, Improved Late Cretaceous and early Cenozoic paleomagnetic apparent polar wander path for the Pacific plate: Earth and Planetary Science Letters, v. 262, p. 1-20.

Carvallo, C., & Camps, P., 2013a, Data report: Magnetic properties of basalts from Shatsky Rise: Proceedings of the Integrated Ocean Drilling Program, v. 324: Tokyo, Integrated Ocean Drilling Program Management International, Inc.), in press.

Carvallo, C., Camps, P., Ooga, M., Fanjat, G., & Sager, W.W., 2013b, Palaeointensity determinations and rock magnetic properties on basalts from Shatsky Rise: New evidence for a Mesozoic dipole low: Geophysical Journal International, in press.

Chenet, A. L., Fluteau, F. Courtillot, V., Gérard, M., and Subbarao, K. V., 2008, Determination of rapid Deccan eruptions across the Cretaceous-Tertiary boundary using paleomagnetic secular variation: Results from a 1200-m-thick section in the Mahabaleshwar escarpment, Journal of Geophysical Research, v. 113, B04101, doi:10.1029/2006JB004635.

Coffin, M.F., and Eldholm, O., 1994, Large igneous provinces: crustal structure, dimensions, and external consequences: Reviews of Geophysics, v. 32, p. 1–36.

Cox, A., and Gordon, R. G., 1984, Paleolatitudes determined from paleomagnetic data from vertical cores: Reviews of Geophysics, v. 22, p. 47-72.

Creer, K. M., 1981, Long-period geomagnetic secular variations since 12,000 yr B.P.: Nature, v. 292, p. 208-212.

Daly, L., and LeGoff, M., 1996, An updated and homogeneous world secular variation database: I. Smoothing of the archeomagnetic results: Physics of the Earth and Planetary Interiors, v. 93, p. 159-190.

Day, R., Fuller, M., and Schmidt, V. A., 1977, Hysteresis properties of titanomagnetites: grain-size and compositional dependence: Physics of the Earth and Planetary Interiors, v. 13, p. 260-267.

Doubrovine, P. V., and Tarduno, J. A., 2004, Self-reversed magnetization carried by titanomaghemite in ocean basalts: Earth and Planet Science Letters, v. 222, p. 959-969..

Doubrovine, P. V. and Tardnuno, J. A., 2005, On the compositional field of self-reversing titanomaghemite: Constraints from Deep Sea Drilling Project Site 307: Journal of Geophysical Research, v. 110, 12 p., B11104, doi:10.1029/2005JB003865.

Duncan, R.A., Richards, M.A., 1991, Hotspots, mantle plumes, flood basalts and true polar wander: Reviews of Geophysics, v. 29, p. 31–50.

Dunlop, D. J., 2002a. Theory and application of the Day plot (Mrs/Ms vs. Hcr/Hc), 1. Theoretical curves and tests using titanomagnetite data. J. Geophys. Res., 107:10.1029/2001JB000486.

Dunlop, D. J., 2002b. Theory and application of the Day plot (Mrs/Ms vs. Hcr/Hc), 2. Application to data for rocks, sediments, and soils. J. Geophys. Res., 107:10.1029/2001JB000487.

Dunlop, D. J., and Özdemir, O., 2007, Magnetizations in rocks and minerals: Geomagnetism, Treatise on Geophysics, v. 5, p. 277-336.

Foulger, G.R., 2007, The "plate" model for the genesis of melting anomalies. *in* Foulger, G.R., and Jurdy, D.M., eds., Plates, Plumes, and Planetary Processes: Boulder, Colorado, Geological Society of America Special Paper 430, p. 1-28.

Fuller, M., Molina-Garza, R., Touchard, Y., and Kidane, T., 2006. Paleomagnetic records from carbonate legs in the southern oceans and attendant drilling and coring related effects. Phys. Earth Planet. Int., 156:242-260.

Gogorza, C. S., Sinito, A. M. Ohlendorf, C. Kastner, S., and Zolitschka, B., 2011, Paleosecular variation and paleointensity records for the last millennium from southern South America (Laguna Potrok Aike, Santa Cruz, Argentina): Physics of the Earth and Planetary Interiors, v. 184, p. 41-50.

Harrison, C. G. A., 1980, Secular variation and excursions of the magnetic earth's magnetic field: Journal of Geophysical Research, v. 85, p. 3511-3522.

Heller, P.L., Anderson, D.L., Angevine, C.L., 1996, Is the middle Cretaceous pulse of rapid sea-floor spreading real or necessary?: Geology, v. 24, p. 491–494.

Johnson, C., Constable, C. G., Tauxe, L., Barendregt, R., Brown, L. L., Coe, R. S., Layer, P., Mejia, V., Opdyke, N. D., Singer, B. S., Staudigel, H., and Stone, D. B., 2008,

Recent investigations of the 0-5 Ma geomagnetic field recorded by lava flows: Geochemistry, Geophysics, Geosystems, v. 9, 31 p., doi:10.1029/2007GC001696.

Kirschvink, J., 1980, The least squares line and plane and the analysis of palaeomagnetic data: Geophysical Journal of the Royal Astronomical Society, v. 62, p. 699-718.

Kent, D. V., Wang, H., and Rochette, P., 2010, Equatorial paleosecular variation of the geomagnetic field from 0 to 3 Ma lavas from the Galapagos Islands: Physics of the Earth and Planetary Interiors, v. 183, p. 404-412.

Kono, M., 1980, Paleomagnetism of DSDP Leg 55 basalts and implications for the tectonics of the Pacific plate:Initial Reports of the Deep Sea Drilling Project, v. 55: Washington, DC, U.S. Government Printing Office, p. 737–752.

Koppers, A. A. P., Sano, T., Natland, J. H., Widdowson, M., Almeev, R., Greene, A. R., Murphy, D. T., Delacour, A., Miyoshi, M., Shimizu, K., Li, S., Hirano, N., Geldmacher, J., and the Expedition 324 Scientists, 2010, Massive basalt flows on the southern flank of Tamu Massif, Shatsky Rise: A reappraisal of ODP Site 1213 basement units: Proceedings of the Integrated Ocean Drilling Program, v. 324, Tokyo, Integrated Ocean Drilling Program Management International, Inc..doi:10.2204.iodp.proc.324.2010.

Larson, R.L., and Sager, W.W., 1992, Skewness of magnetic anomalies M0 to M29 in the northwestern Pacific: Proceedings of the Ocean Drilling Program, Scientific Results, v. 129: College Station, Texas, Ocean Drilling Program, p. 471–481.

Larson, R.L., Steiner, M.B., Erba, E., and Lancelot, Y., 1992, Paleolatitudes and tectonic reconstructions of the oldest Pacific portion of the Pacific plate: A comparative study: Proceedings of the Ocean Drilling Program, Scientific Results, v. 129: College Station, Texas, Ocean Drilling Program, p. 615–631.

Lund, S. P., Schwartz, M., Keigwin, L., and Johnson, T., 2005, Deep-sea sediment records of the Laschamp geomagnetic field excursion (~41,000 calendar years before present): Journal of Geophysical Research, v. 110, B04101, doi:10.1029/2003JB002943.

Mahoney, J. J., Duncan, R. A., Tejada, M. L. G., Sager, W. W., and Bralower, T. J., 2005, Jurassic-Cretaceous boundary age and mid ocean ridge type mantle source for Shatsky Rise: Geology, v. 33, p. 185-188.

Nakanishi, M., Sager, W. W., and Klaus, A., 1999, Magnetic lineations within Shatsky Rise, northwest Pacific Ocean: Implications for hot spot-triple junction interaction and oceanic plateau formation: Journal of Geophysical Research, v. 104, p. 7539-7556.

Özdemir, Ö., and O'Reilly, W., 1982, Magnetic hysteresis properties of synthetic monodomain titanomaghemites: Earth and Planetary Science Letters, v. *57*, p. 437-447.

Pueringer, M., Sager, W., and Housen, B., in press, Data report: Paleomagnetic measurements of igneous rocks from Shatsky Rise Expedition 324, Proceedings of the Integrated Ocean Drilling Program, v. 324.

Sager, W.W., 2005, What built Shatsky Rise, a mantle plume or ridge tectonics?, in Foulger, G.R., Natland, J.H., Presnall, D.C., and Anderson, D.L., eds., Plates, plumes, and paradigms: Boulder, Colorado, Geological Society of America, Special Paper 388, p. 721–733.

Sager, W.W., 2006, Cretaceous paleomagnetic apparent polar wander path for the Pacific plate calculated from Deep Sea Drilling Project and Ocean Drilling Program basalt cores: Physics of the Earth and Planetary Interiors, v. 156, p. 329–349..

Sager, W. W., Evans, H. F., and Channell, J. E. T., 2005, Paleomagnetism of Early Cretaceous (Berriasian) sedimentary rocks, Hole 1213B, Shatsky Rise, i*n* Proceedings of the Ocean Drilling Program, Scientific Results, v. 198: College Station, TX, Ocean Drilling Program, 14 p.

Sager, W., and Han, H. C., 1993, Rapid formation of the Shatsky Rise oceanic plateau inferred from its magnetic anomaly: Nature, v. 364, p. 610-613.

Sager, W.W., and Horner-Johnson, B.C., 2004, Paleomagnetism of basaltic rocks cored at ODP Site 1179: implications for mid-Cretaceous Pacific plate paleolatitude and paleomagnetic pole: Proceedings of the Ocean Drilling Program, v. 191, p. 1–20.

Sager, W., Kim, J., Klaus, A., Nakanishi, M. and Khankishieva, L., 1999, Bathymetry of Shatsky Rise, northwest Pacific Ocean: Implications for ocean plateau development at a triple junction: Journal of Geophysical Research, v. 104, p. 7557-7576.

Sager, W. W., Sano, T., and Geldmacher, J., 2011a, How do oceanic plateaus form? Clues from drilling Shatsky Rise: EOS, Transactions of the American Geophysical Union, v. 92, p. 37-44.

Sager, W. W., Sano, T., Geldmacher, J., and the Expedition 324 Scientists, 2010, Proceedings of the Integrated Ocean Drilling Program, v. 324, Tokyo, Integrated Ocean Drilling Program Management International, Inc.

Sager, W. W., Sano, T., Geldmacher, J., and the Expedition 324 Scientists, 2011b, IODP Expedition 324: Ocean drilling at Shatsky Rise gives clues about oceanic plateau formation: Scientific Drilling, v. 12, p. 24-31.

Sharp, W. D., Turrin, B. D., Renne, P. R., & Lanphere, M. A., 1996, The $^{40}Ar/^{39}Ar$ and K/Ar dating of lavas from the Hilo 1-km core hole, Hawaii Scientific Drilling Project: Journal of Geophysical Research, v. 101, p. 607-616.

Shipboard Scientific Party, 2002, Site 1213, *in* Bralower, T. J., Premoli Silva, I., Malone, M. J., et al., Proceedings of the Ocean Drilling Program, Initial Reports, v. 198: College Station, Texas, Ocean Drilling Program, 110 p.

Stolper, E. M., DePaolo, D. J., and Thomas, D. M., 2009, Deep drilling into a mantle plume volcano: the Hawaii Scientific Drilling Project: Scientific Drilling, v. 7, p. 4-14.

Tauxe, L., 1998. Paleomagnetic principles and practice. Dordrecht, The Netherlands: Kluwer Academic Publishers.

Turner, G. M., and Thompson R., 1981, Lake sediment record of the geomagnetic secular variations in Britain during Holocene times: Geophysical Journal of the Royal Astronomical Society, v. 65, p. 703-725.

Tominaga, M., Evans, H. F., and Iturrino G., 2012, "Equator Crossing" of Shatsky Rise?: New insights on Shatsky Rise tectonic motion from the downhole magnetic architecture of the uppermost lava sequences at Tamu Massif: Geophysical Research Letters., v. 39, L21301, doi:10.1029/2012GL052967.

Tominaga, M., Sager, W.W., and Channell, J.E.T., 2005, Paleomagnetism of the igneous section, Hole 1213B, Shatsky Rise: Proceedings of the Ocean Drilling Program, Scientific Results, v. 198: College Station, Texas,Ocean Drilling Program, p. 1–15.

Wessel, P., Y. Harada, and Kroenke L. W., 2006, Towards a self-consistent, high-resolution absolute plate motion model for the Pacific: Geochemistry, Geophysics, Geosystems, v. 7, Q03L12, doi:10.1029/2005GC001000.

APPENDIX A

FIGURES AND TABLES FOR MANUSCRIPT #1

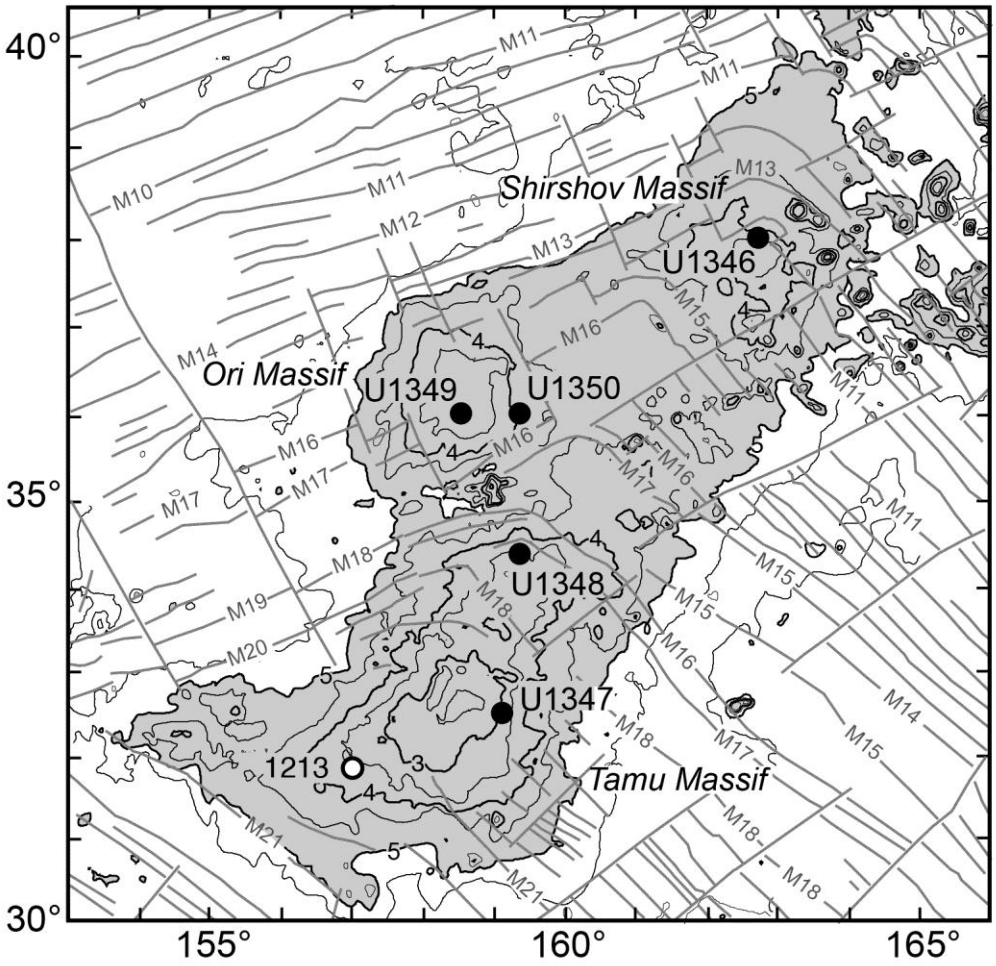

Figure 1.1. Map of Shatsky Rise showing the location of IODP Expedition 324 sites (U1346-U1350) and ODP Site 1213. Depths above 5 km are shaded. Gray lines show magnetic lineations and fracture zones (Nankanishi et al., 1999).

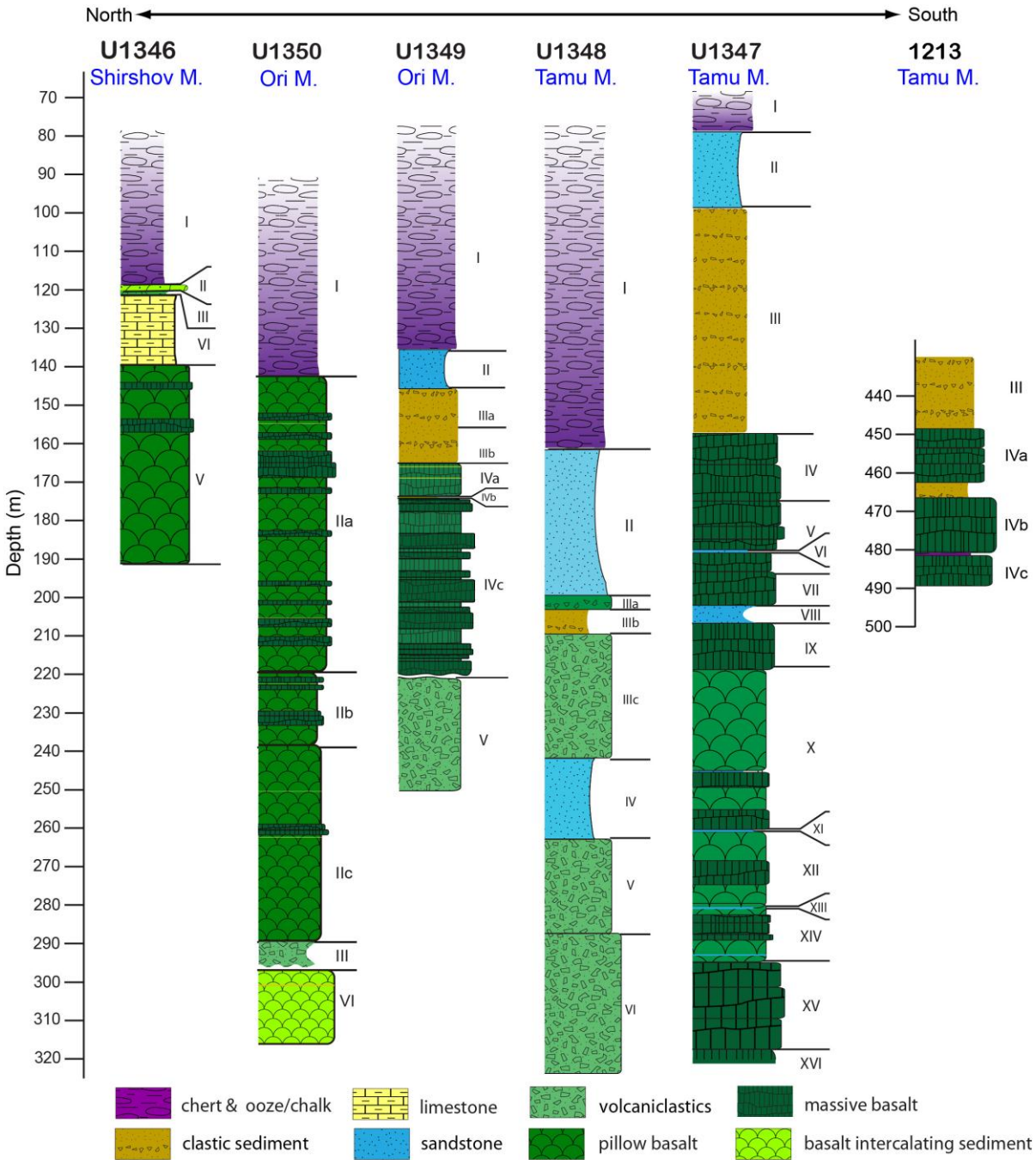

Figure 1.2. Graphic lithology sections for IODP Expedition 324 sites and ODP Site 1213. Roman numerals are lithologic unit numbers; units are described in the IODP Proceedings (Sager et al., 2010).

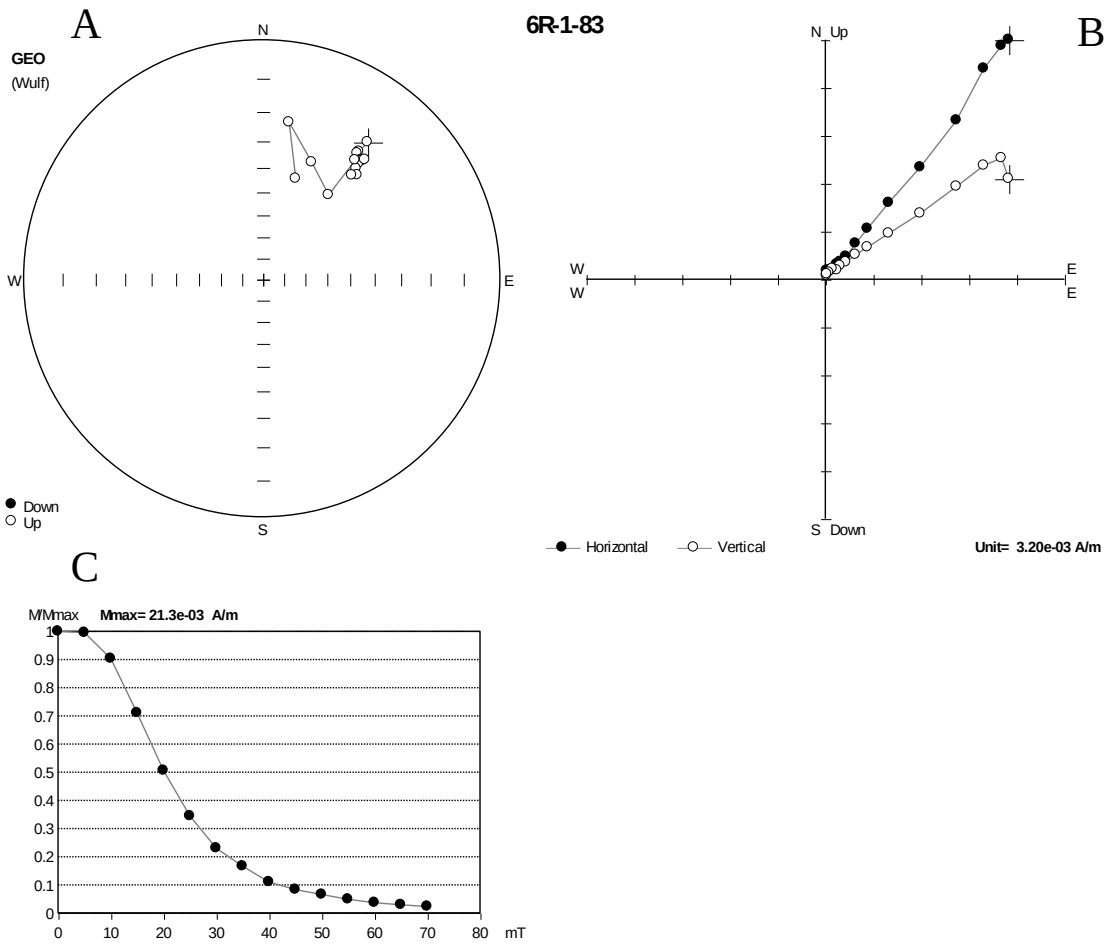

Figure 1.3. Sample 324-U1346A-6R-1, 83-85 cm AF demagnetization. A) equal angle spherical projection, B) Zijderveld plot, C) magnetic intensity versus demagnetization step. This sample exhibits higher MDF behavior typical of many AF demagnetized samples at site.

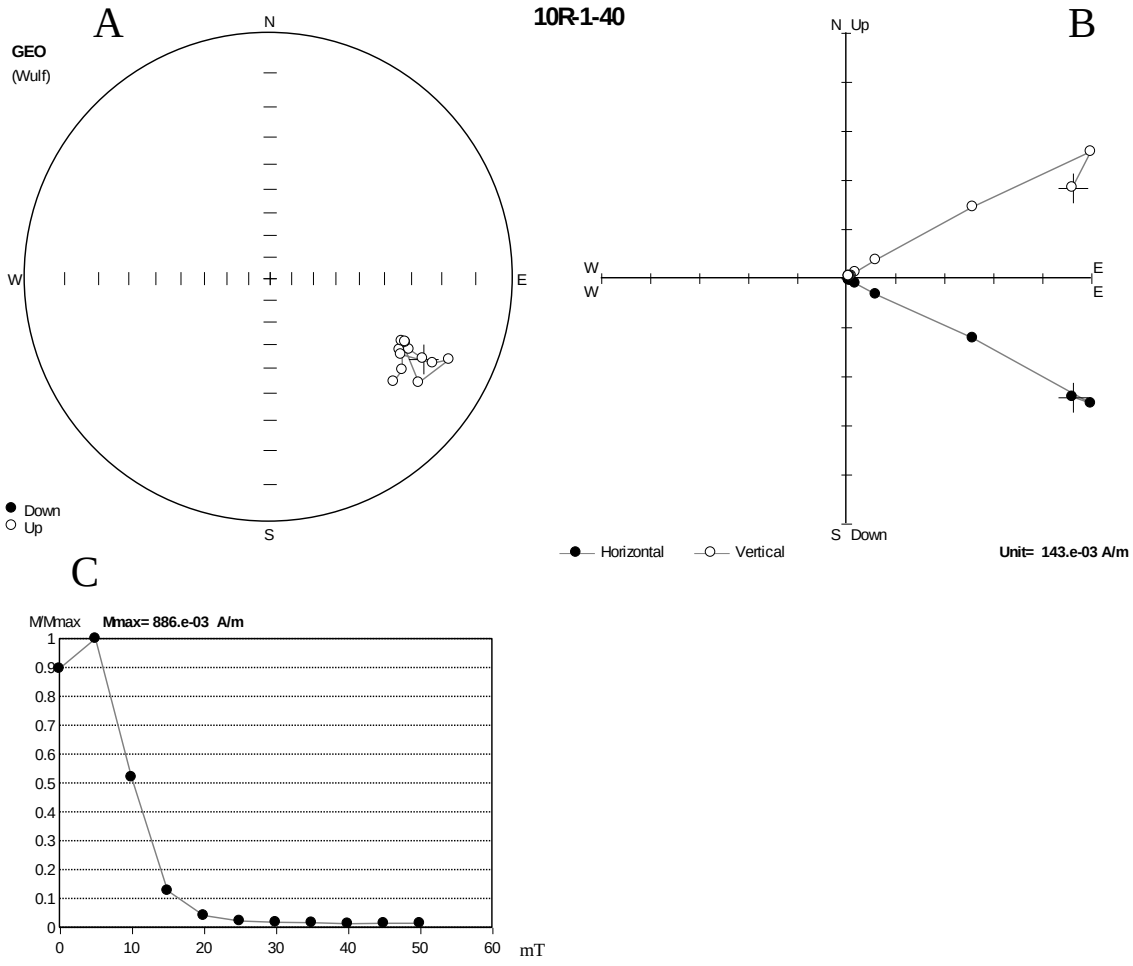

Figure 1.4. Sample 324-U1346A-10R-1, 40-42 cm AF demagnetization. A) Equal angle spherical projection, B) Zijderveld plot, C) magnetic intensity versus demagnetization step. This sample displays low MDF behavior during demagnetization. Despite the low MDF, the weak magnetizations at higher demagnetization steps are consistent.

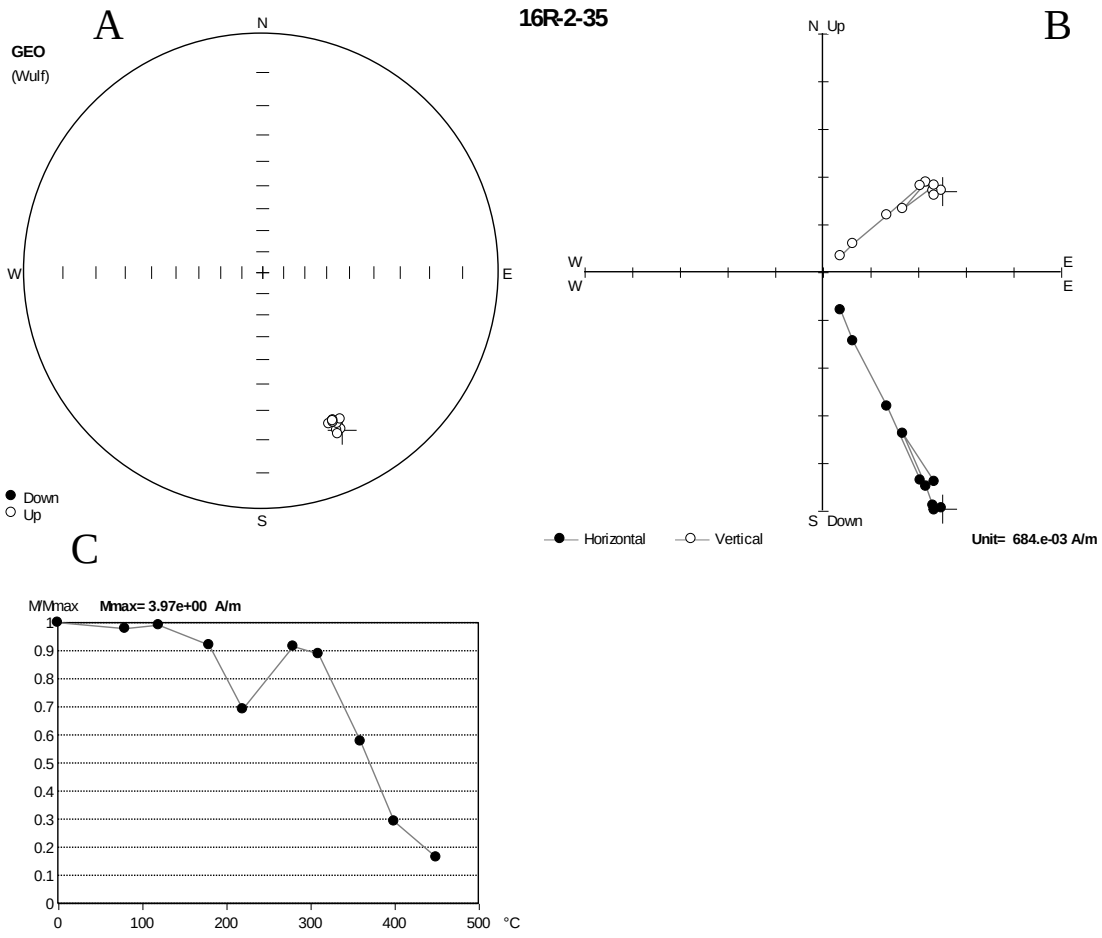

Figure 1.5. Sample 324-U1346A-16R-2, 35-37 cm thermal demagnetization. A) Equal angle spherical projection, B) Zijderveld plot, C) magnetic intensity versus demagnetization step. This example shows large overprint behavior typical of thermally demagnetized samples at site. It also shows a segment of partial self-reversal in the demagnetization path.

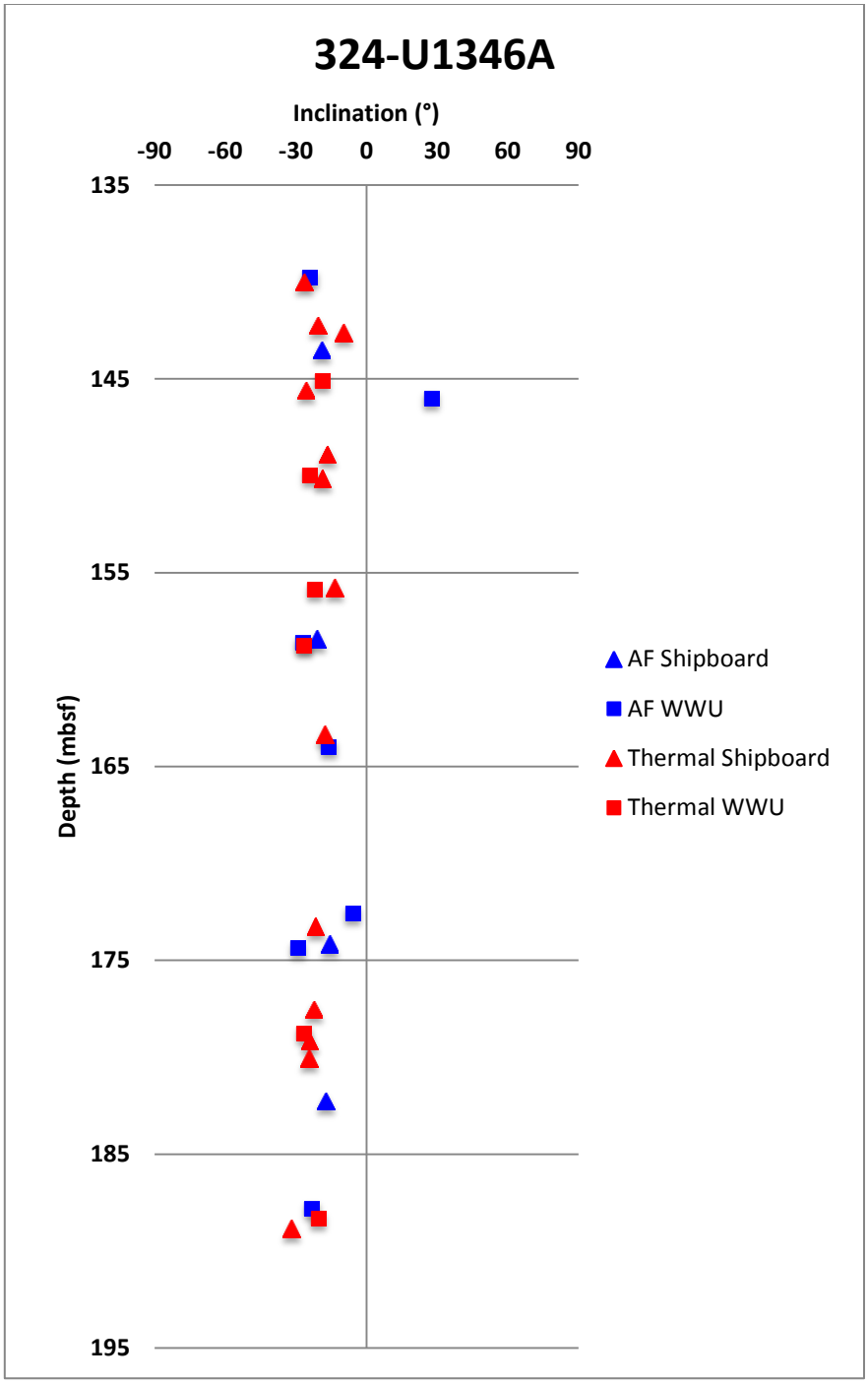

Figure 1.6. Site U1346 sample principal component inclinations versus depth. In blue are the AF demagnetized results and in red are the thermally demagnetized results. The triangles are samples measured shipboard during Expedition 324 and the squares are samples measured at WWU.

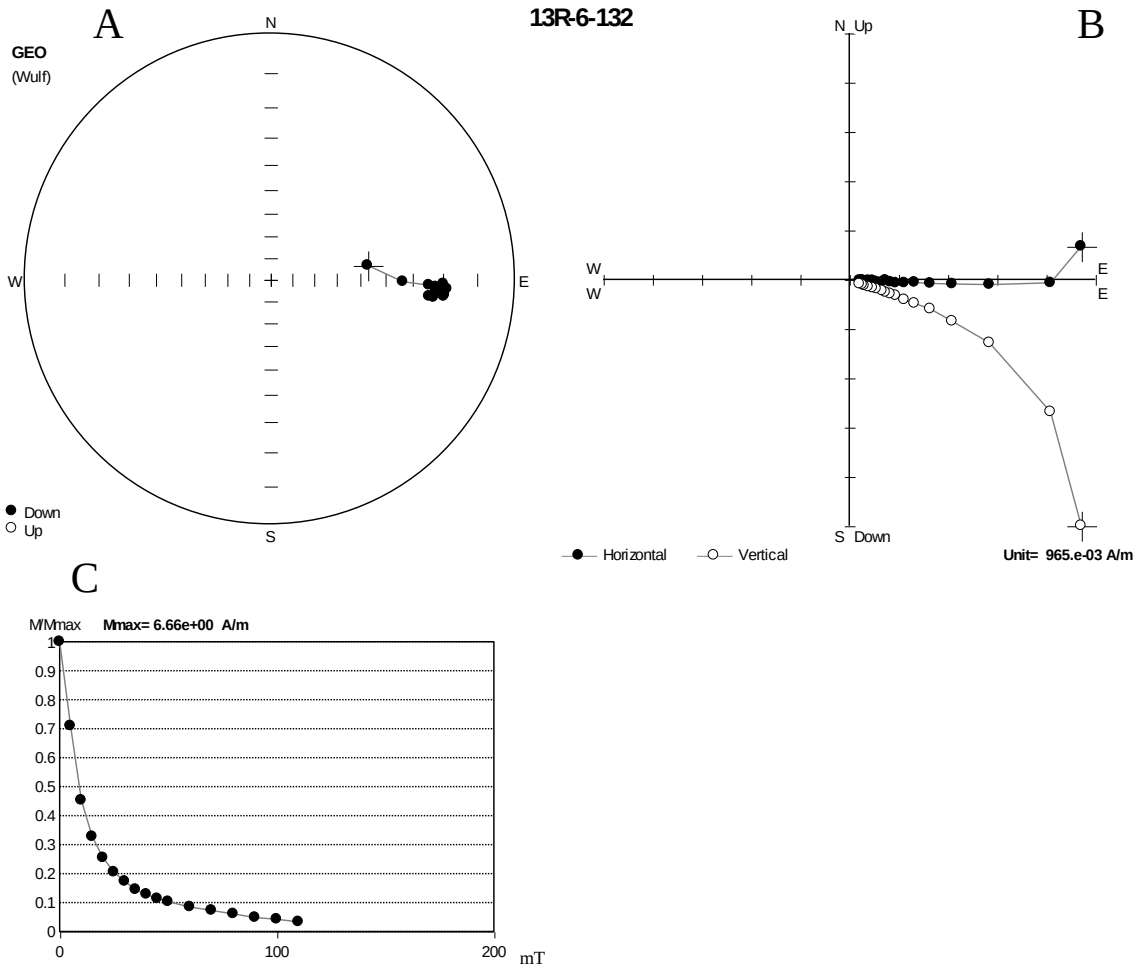

Figure 1.7. Sample 324-1347A-13R-6, 132-134 cm AF demagnetization. A) Equal angle spherical projection, B) Zijderveld plot, C) magnetic intensity versus demagnetization step. This sample exhibits high MDF behavior during AF demagnetization.

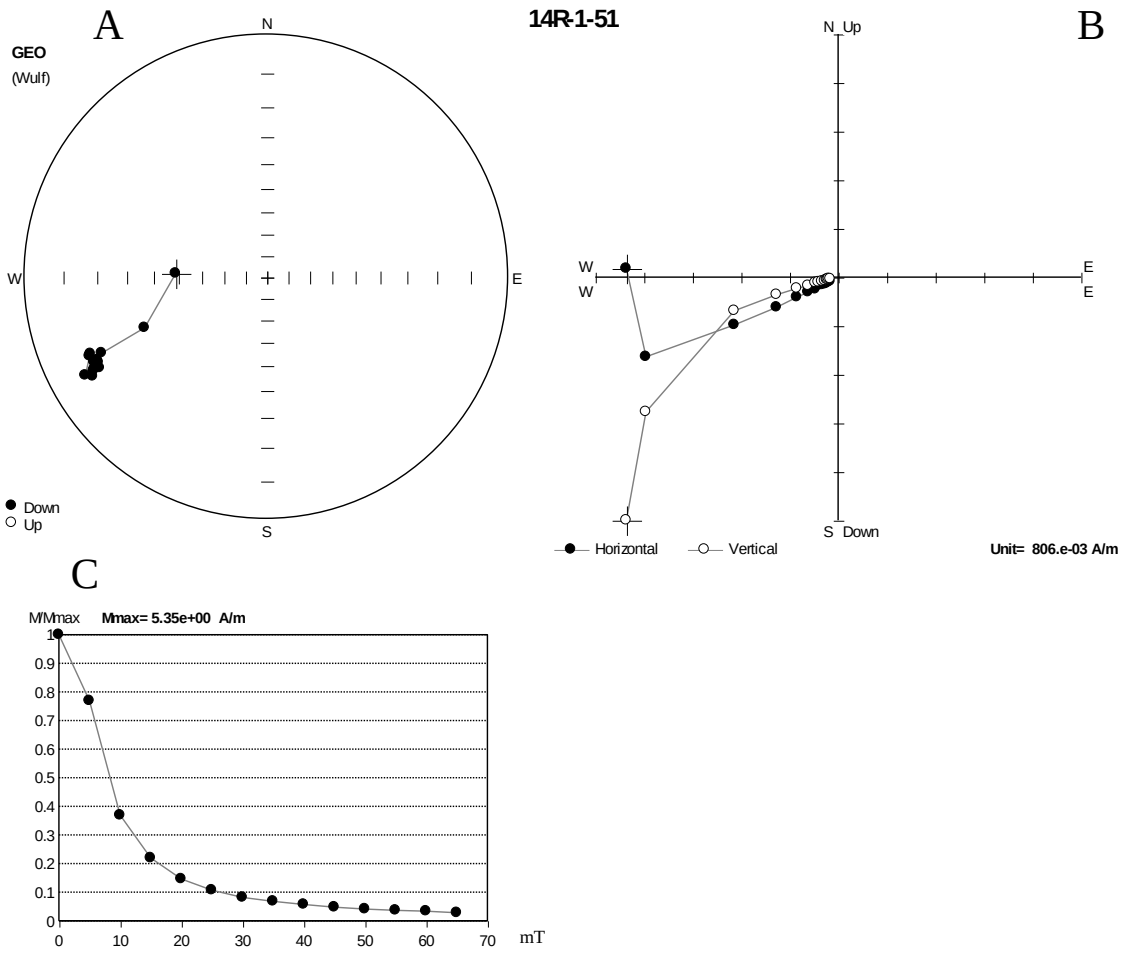

Figure 1.8. Sample 324-1347A-14R-1, 51-53 cm AF demagnetization. A) Equal angle spherical projection, B) Zijderveld plot, C) magnetic intensity versus demagnetization step. This sample shows an example of low MDF behavior during AF demagnetization . Despite the low MDF, the weak magnetizations at higher demagnetization steps <60 mT are consistent.

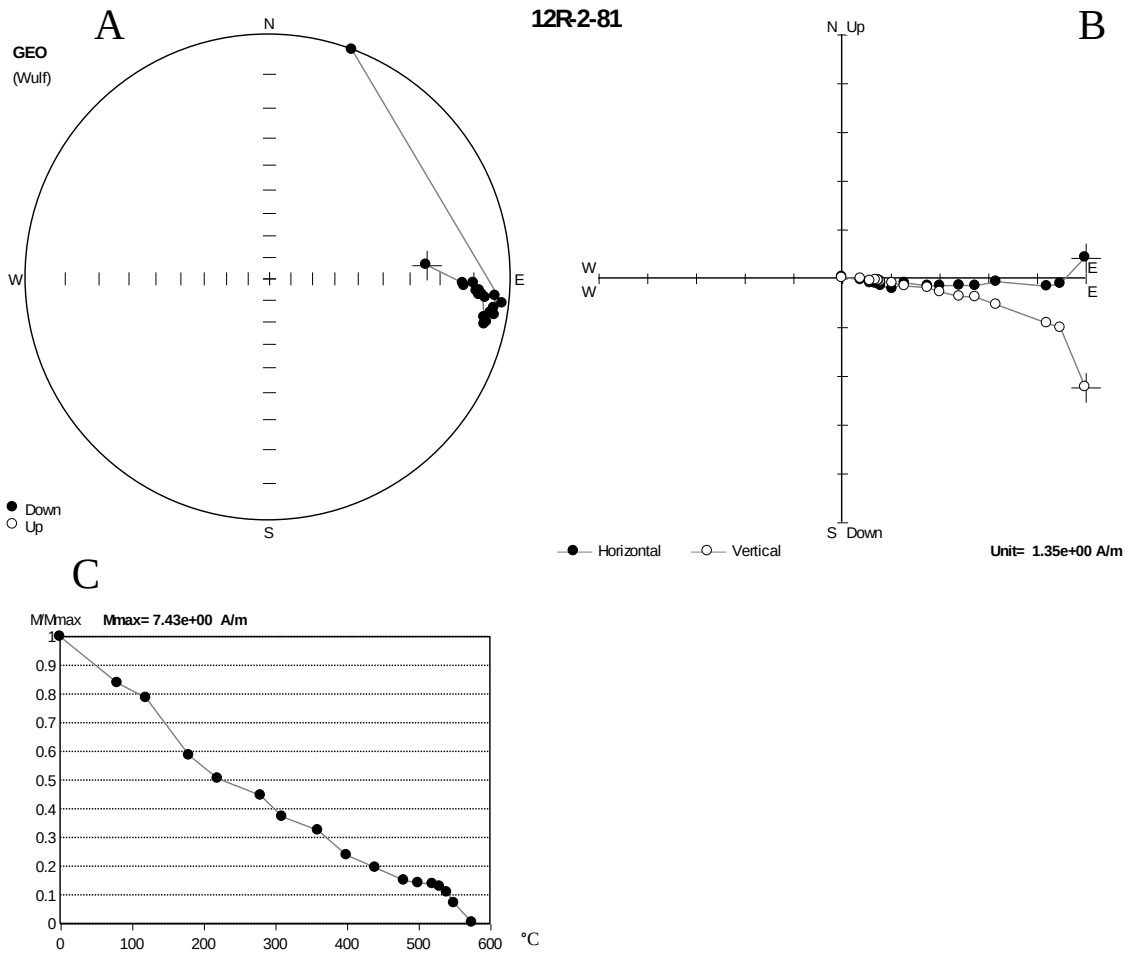

Figure 1.9. Sample 324-1347A-12R-2, 81-83 cm thermal demagnetization. A) Equal angle spherical projection, B) Zijderveld plot, C) magnetic intensity versus demagnetization step. This sample exhibits a linear decay of magnetization with increased heating. The last step at 575°C is inconsistent because sample was fully demagnetized at that temperature.

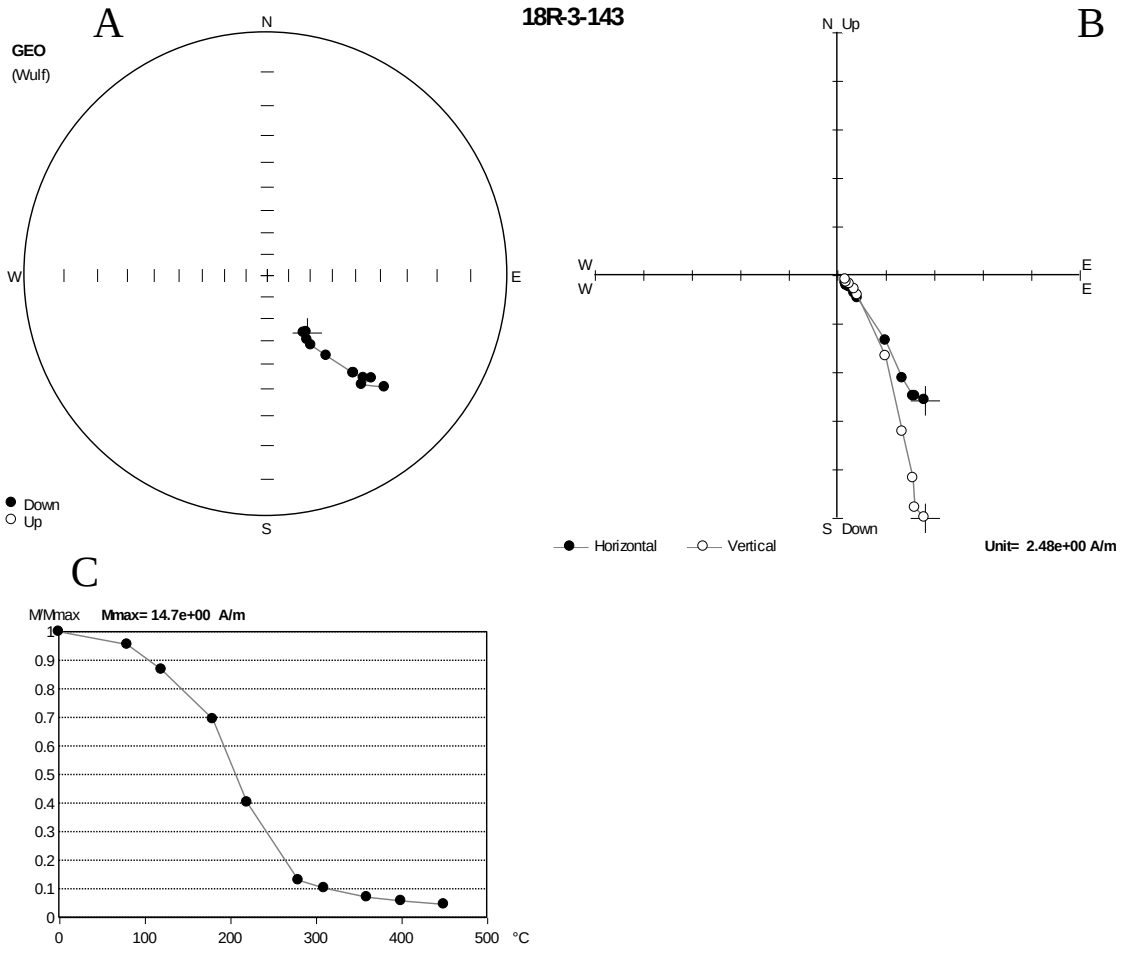

Figure 1.10. Sample 324-1347A-18R-3, 143-145 cm thermal demagnetization. A) equal angle spherical projection, B) Zijderveld plot, C) magnetic intensity versus demagnetization step. This sample displays a significant drop in magnetization intensity at moderate heating steps.

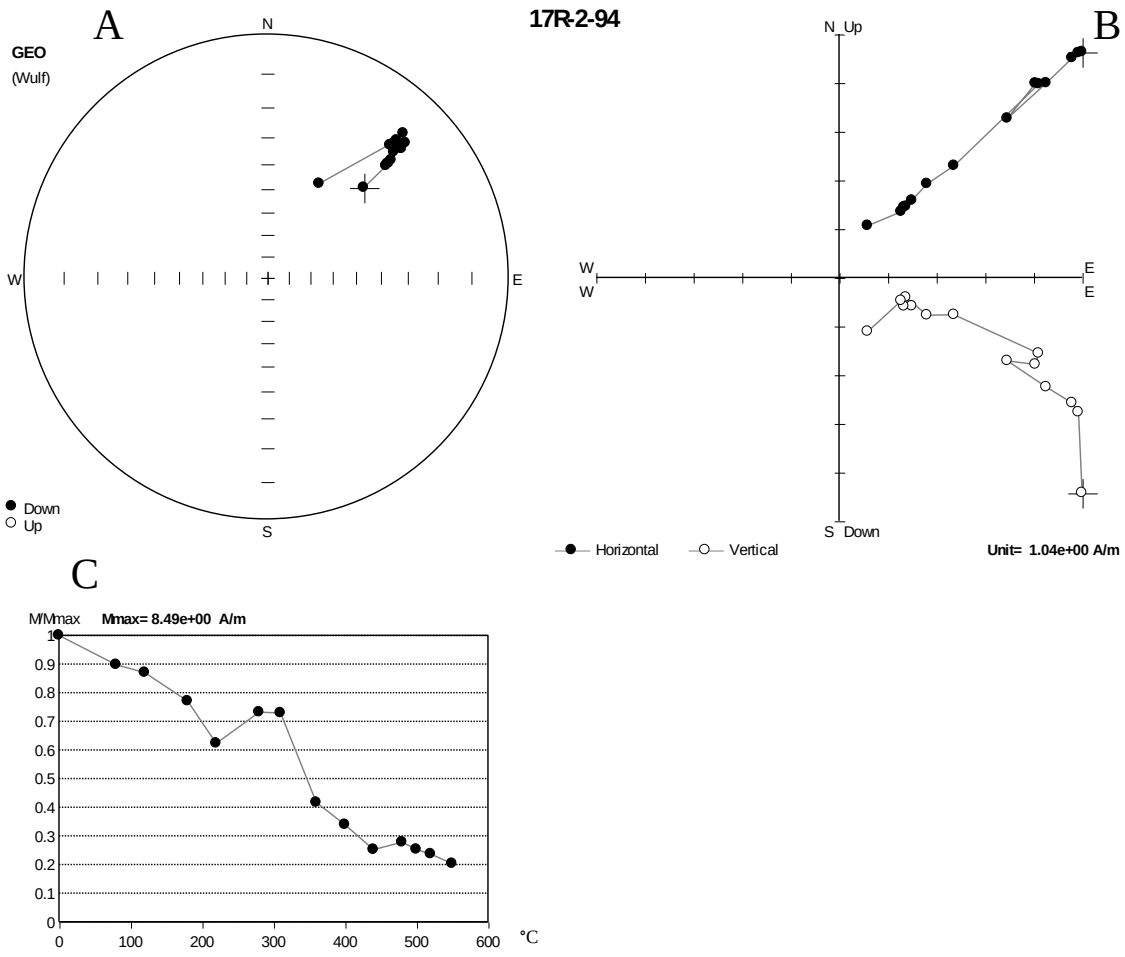

Figure 1.11. Sample 324-1347A-17R-2, 94-96 cm thermal demagnetization. A) Equal angle spherical projection, B) Zijderveld plot, C) magnetic intensity versus demagnetization step. This sample shows an example of a small self-reversal at moderate heating steps. Note that demagnetized magnetization directions are consistent through the self-reversed section except at 550°C.

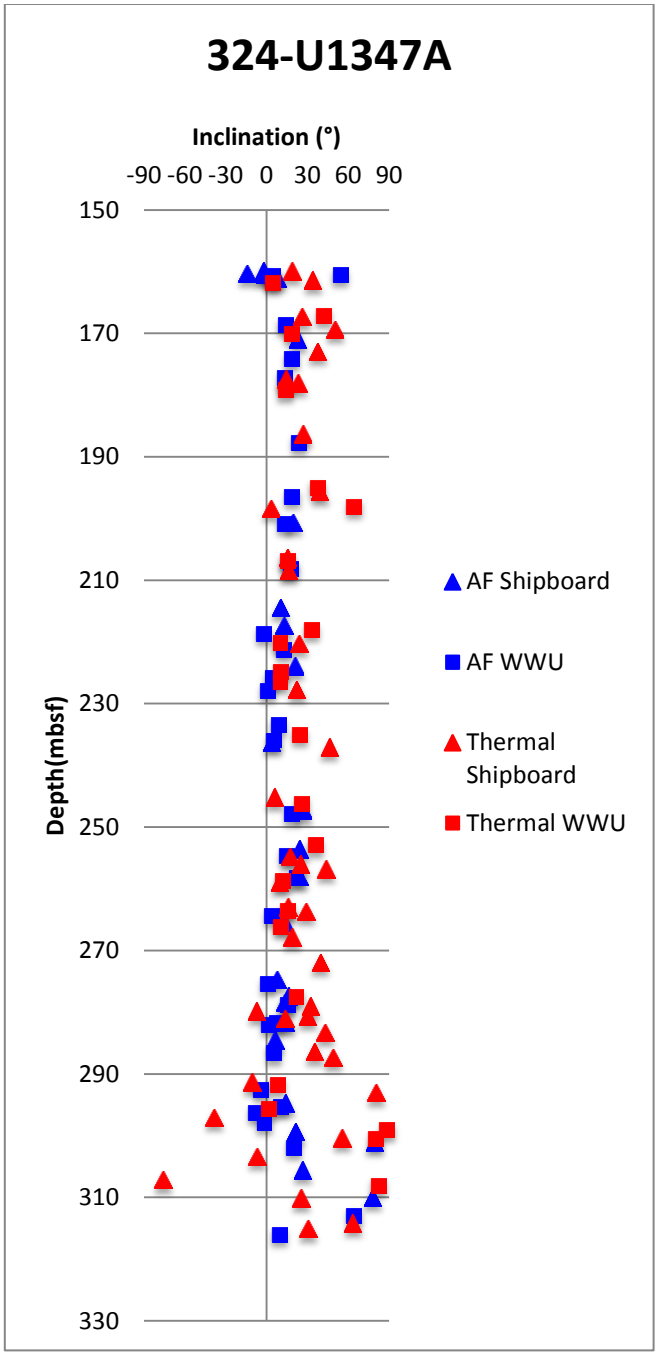

Figure 1.12. Site U1347 sample principal component inclinations versus depth. In blue are the AF demagnetized results and in red are the thermally demagnetized results. Triangles are samples measured shipboard and squares are samples measured at WWU.

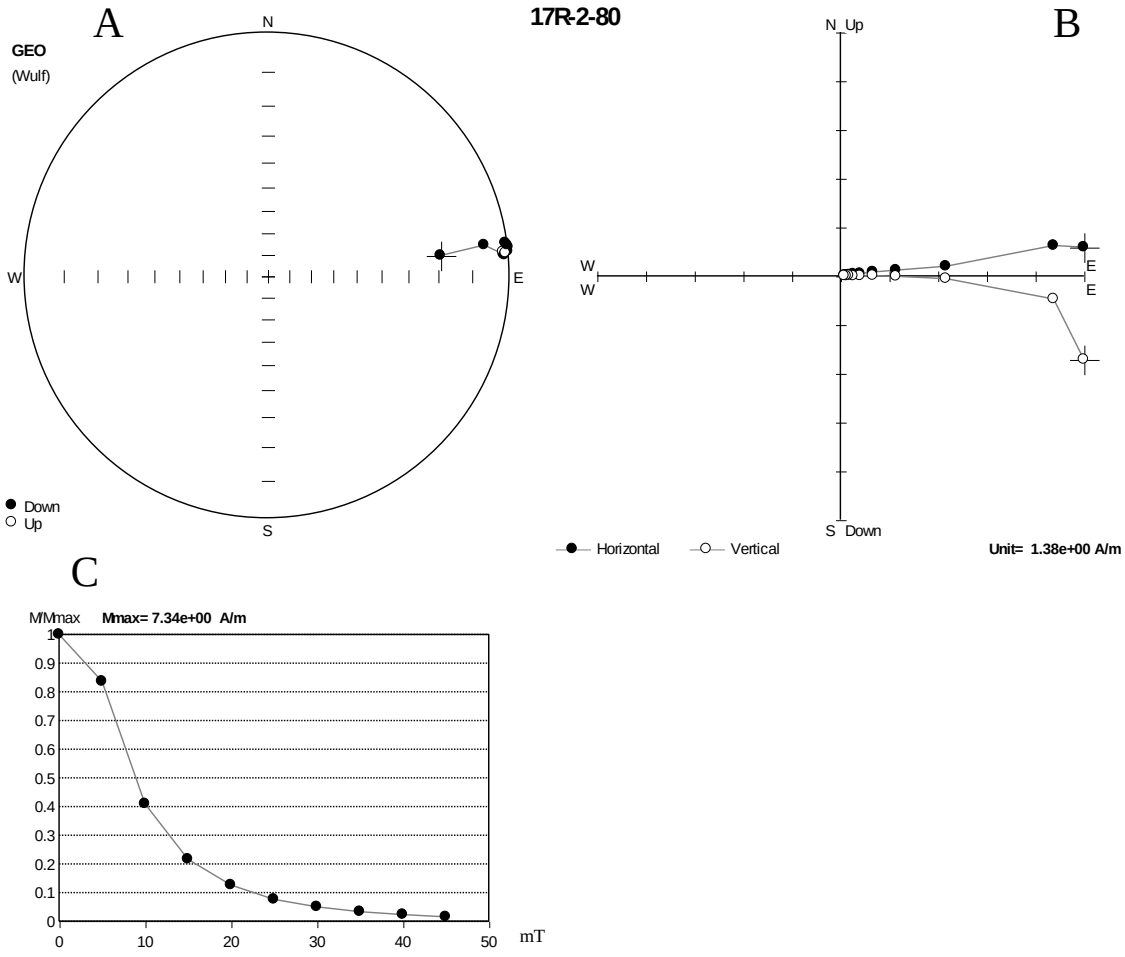

Figure 1.13. Sample 324-1350A-17R-2, 80-82 cm AF demagnetization. A) Equal angle spherical projection, B) Zijderveld plot, C) magnetic intensity versus demagnetization step. This sample exhibits low MDF behavior during AF demagnetization. Once the overprint is removed the inclination changes from positive to negative.

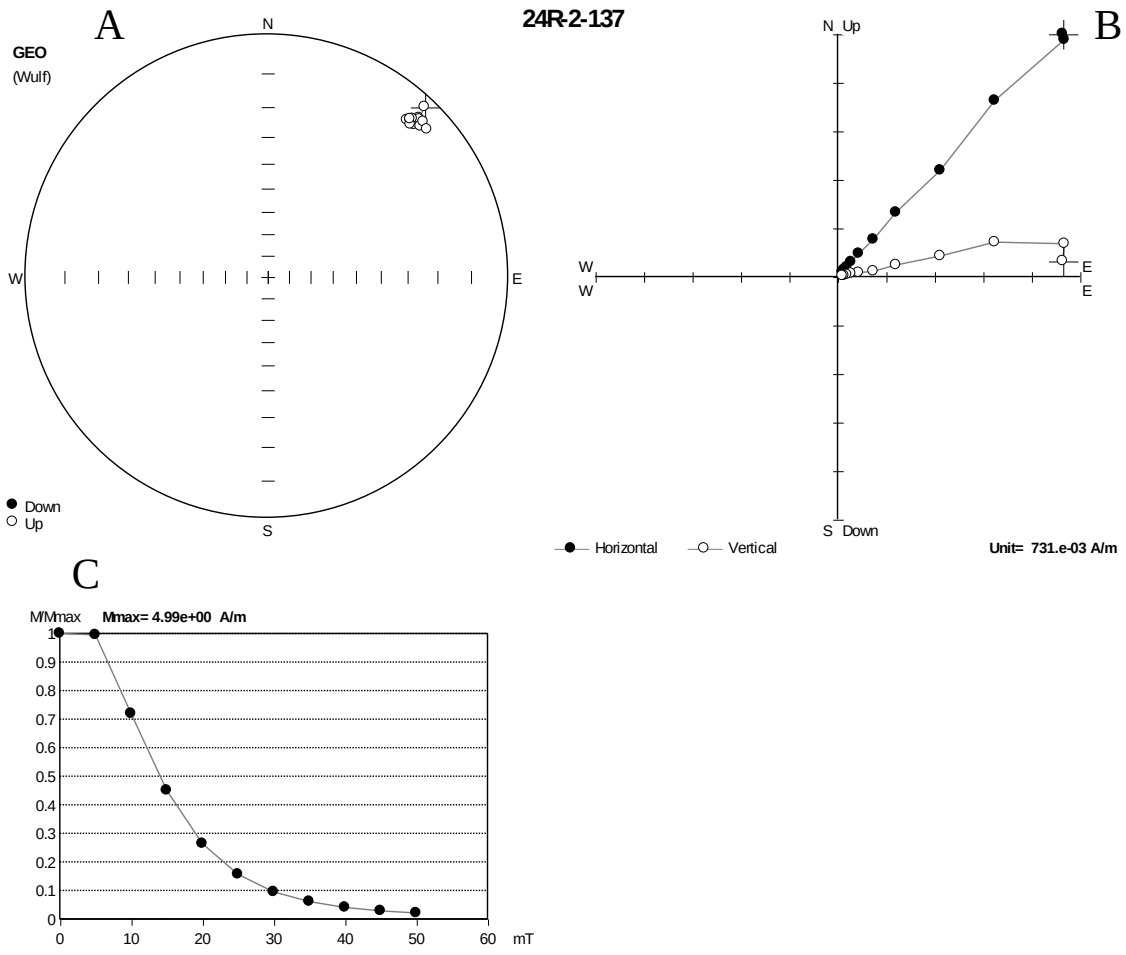

Figure 1.14. Sample 324-1350A-24R-2, 137-139 cm AF demagnetization. A) Equal angle spherical projection, B) Zijderveld plot, C) magnetic intensity versus demagnetization step. This sample displays higher MDF behavior during AF demagnetization.

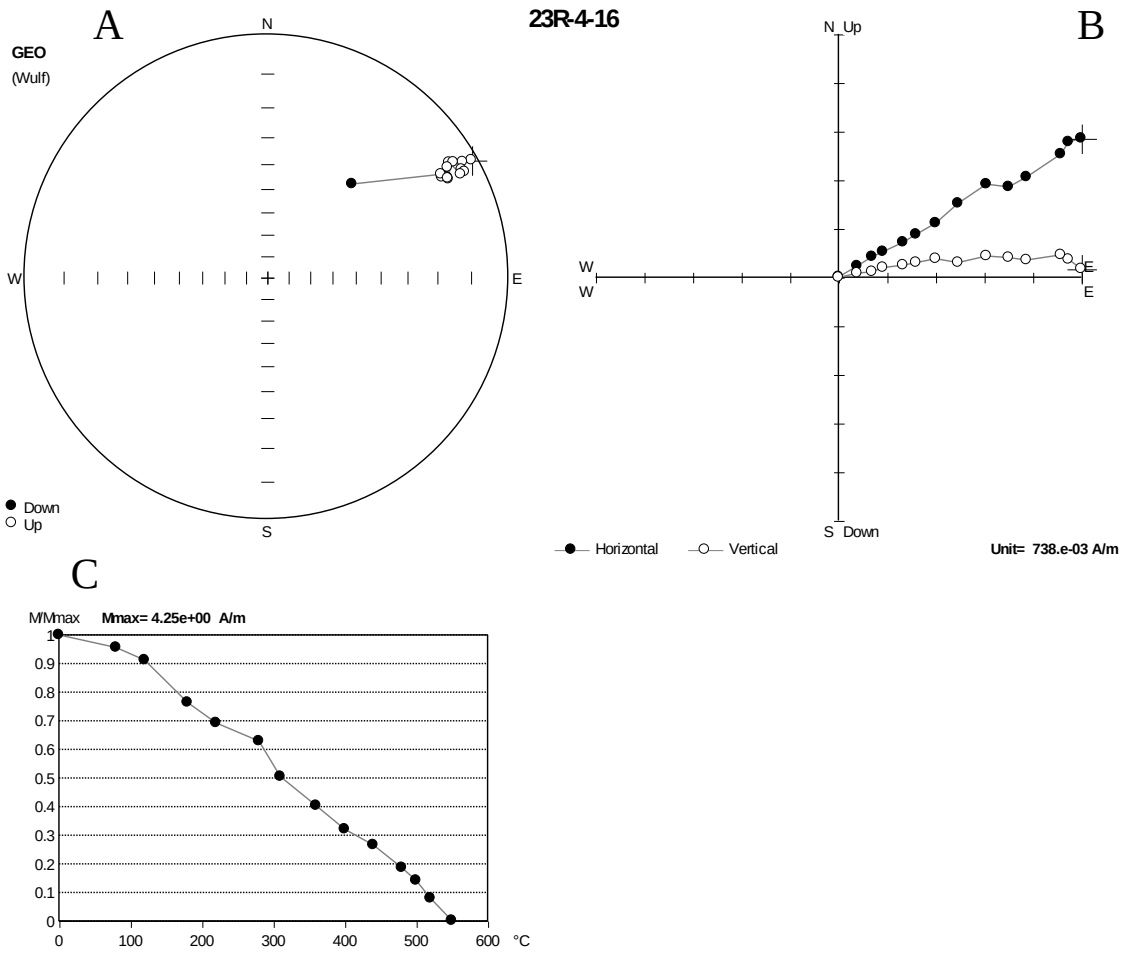

Figure 1.15. Sample 324-1350A-23R-4, 16-18 cm thermal demagnetization. A) Equal angle spherical projection, B) Zijderveld plot, C) magnetic intensity versus demagnetization step. This sample shows linear decay of magnetization intensity with increased temperature.

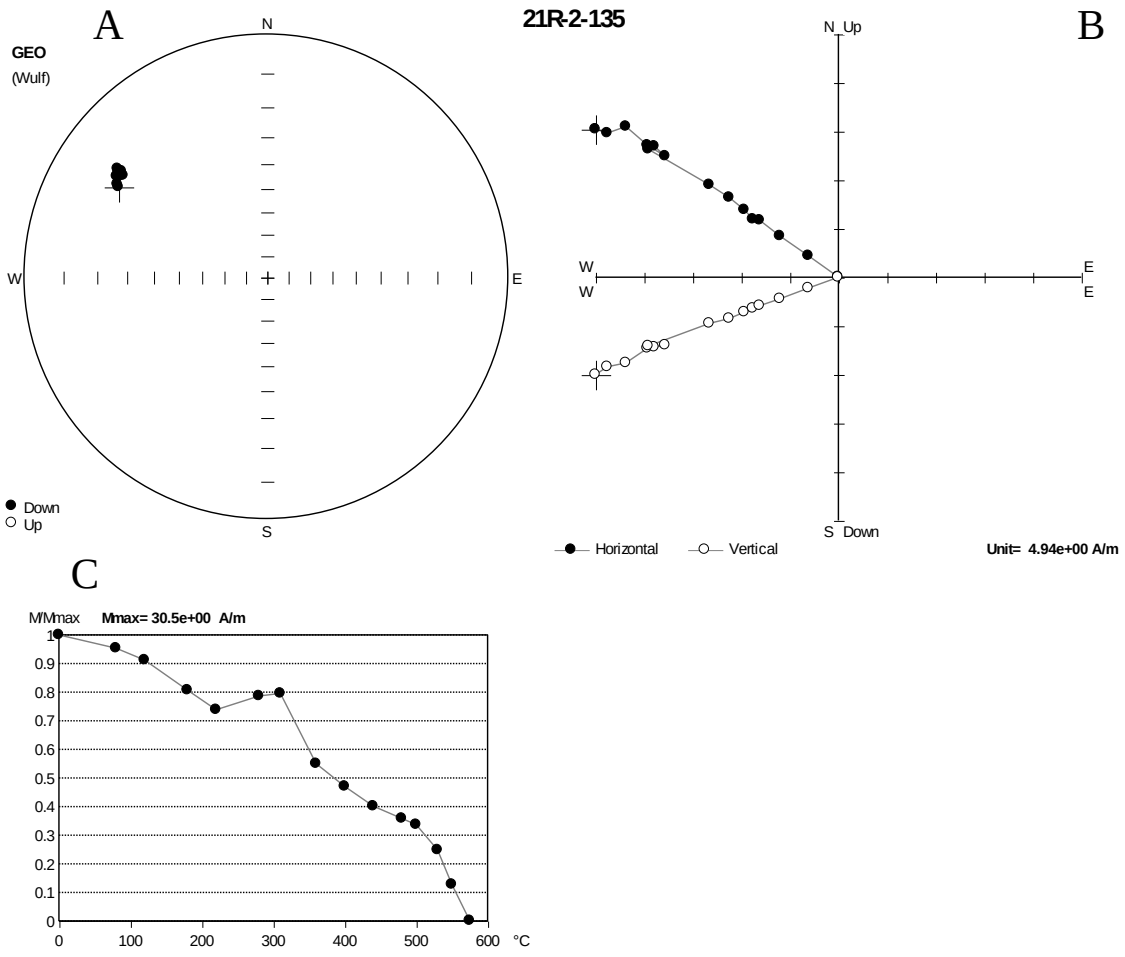

Figure 1.16. Sample 324-1350A-21R-2, 135-137 cm thermal demagnetization. A) Equal angle spherical projection, B) Zijderveld plot, C) magnetic intensity versus demagnetization step. This sample displays a small self-reversal during thermal demagnetization at moderate temperature steps.

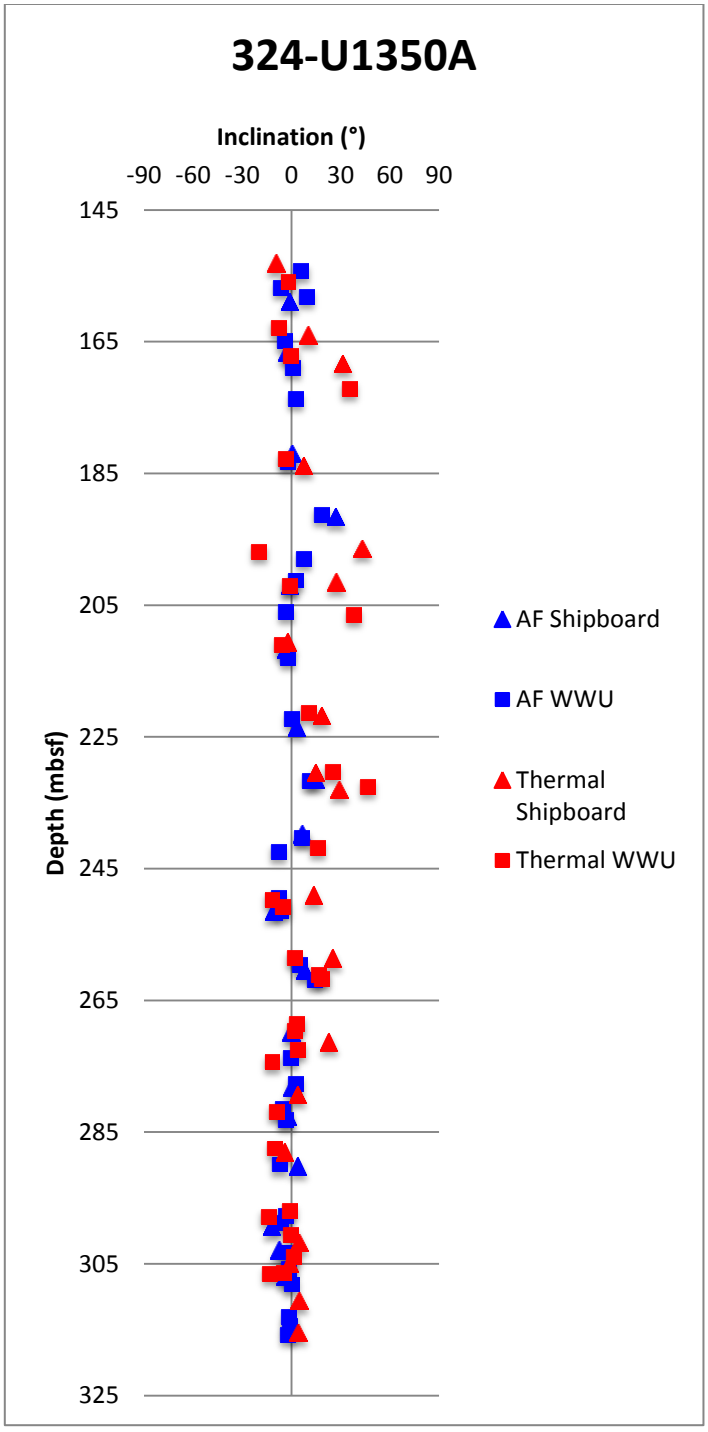

Figure 1.17. Site U1350 sample principal component inclinations versus depth. In blue are the AF demagnetized results and in red are the thermally demagnetized results. Triangles are samples measured shipboard and the squares are samples measured at WWU.

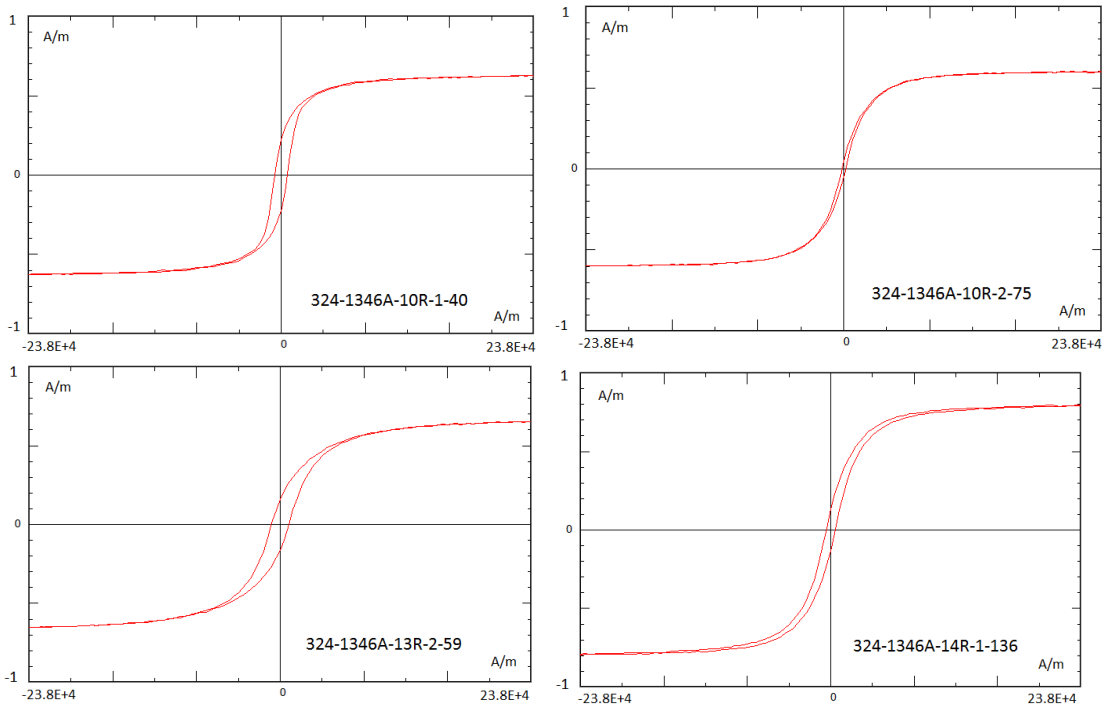

Figure 1.18. Hysteresis loops for Site U1346 samples. The vertical axis is magnetization, M, in A/m units and the horizontal axis is the magnetizing field, H, in A/m.

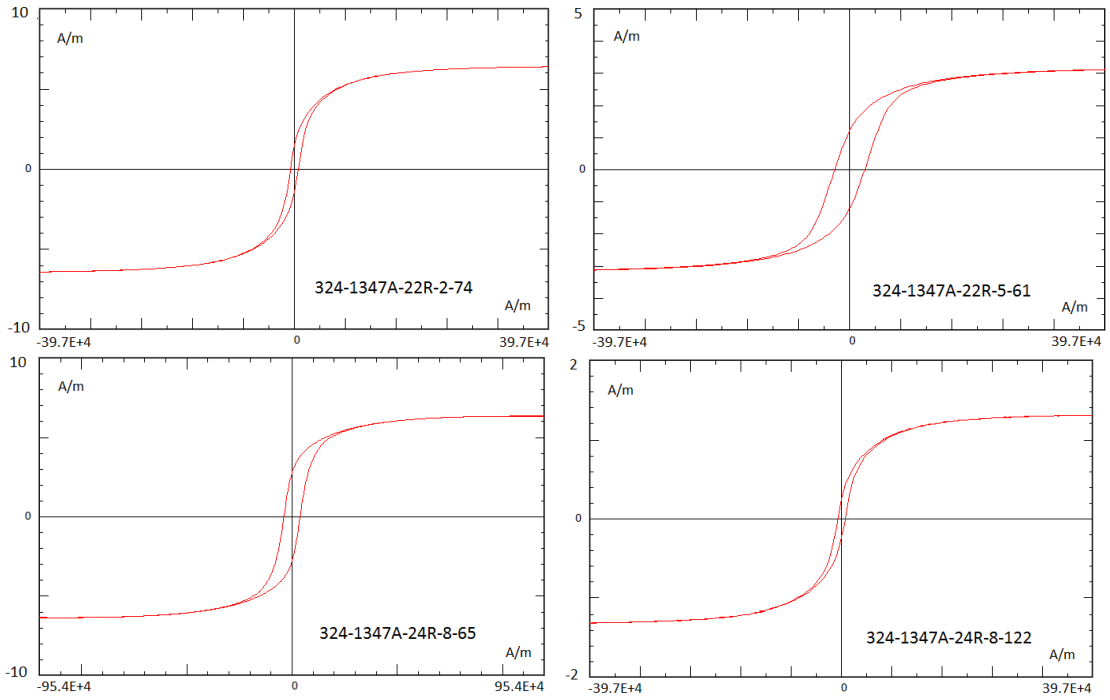

Figure 1.19. Hysteresis loops for Site U1347. The vertical axis is magnetization, M, in A/m units and the horizontal axis is the magnetizing field, H, in A/m.

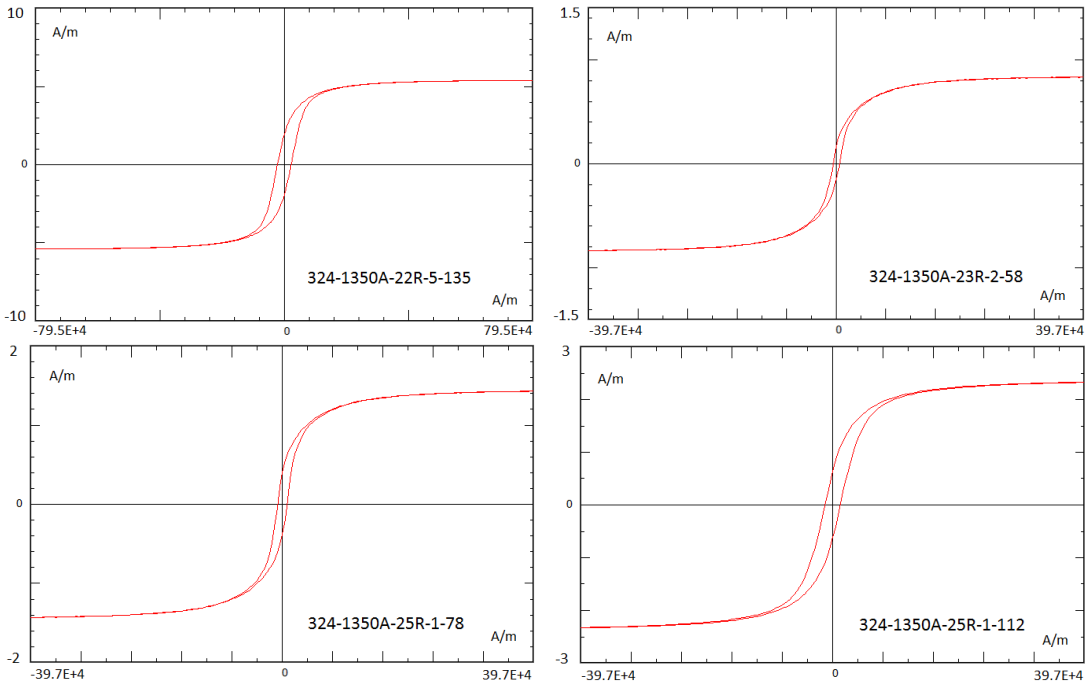

Figure 1.20. Hysteresis loops for Site U1350. The vertical axis is magnetization, M, in A/m units and the horizontal axis is the magnetizing field, H, in A/m.

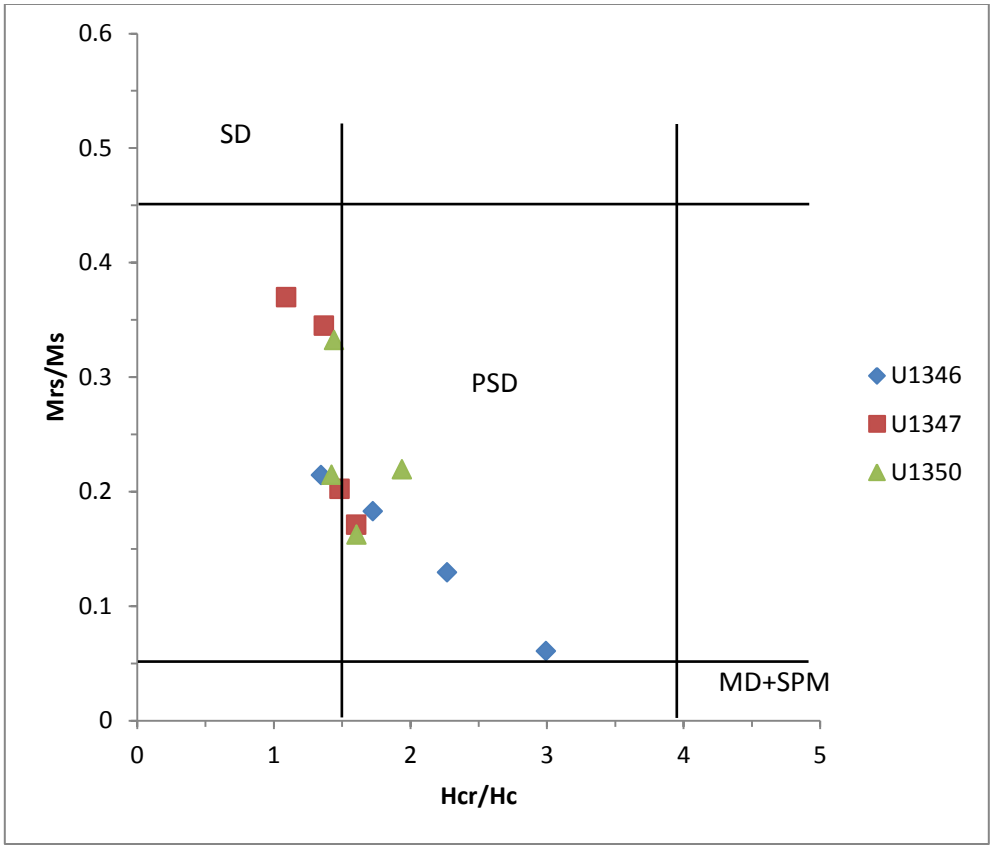

Figure 1.21. Day plot (Day et al., 1977) for Expedition 324 basalt samples. SD = single-domain; PSD = pseudo single-domain; MD+SPM = multidomain and superparamagnetic.

Table 1.1. Site U1346 discrete sample paleomagnetic results.

Core/sect	Int	Depth	Unit #	Lithologic Unit	Location	Treat	Steps	N	Inc (Anc)	MAD (Anc)	Inc	MAD
6R-1,	83-85	139.73	19	Highly vesicular basalt	WWU	AF	25-60	8	-24	3	-23.4	2.8
6R-1,	111–113	140.01	20	Vesicular aphyric basalt	Shipboard	TH	300–475	6	-26.4	1.7		
7R-1,	53.5–55.5	142.24	22	Aphyric amygdaloidal pillow basalt	Shipboard	TH	300–475	6	-20.5	2.4		
7R-1,	92–94	142.62	23	Aphyric amygdaloidal pillow basalt	Shipboard	TH	300–425	4	-9.8	2.3		
7R-2,	39–41	143.5	23	Aphyric amygdaloidal pillow basalt	Shipboard	AF	10–60	8	-19	0.8		
7R-3,	49-51	145.1	24	Aphyric amygdaloidal pillow basalt	WWU	TH	310-450	4	-18.9	1.9	-18.6	2.4
7R-4,	12–14	145.59	26	Aphyric amygdaloidal pillow basalt	Shipboard	TH	300–425	4	-25.7	1.5		
7R-4,	53-55	146	26	Aphyric amygdaloidal pillow basalt	WWU	AF	20-50	7	27.6	1.1	27.7	1.2
8R-1,	136-138	149.96	31	Vesicular aphyric basalt	WWU	TH	280-450	5	-24	2.2	-23.7	2.5
8R-2,	11–13	150.13	31	Vesicular aphyric basalt	Shipboard	TH	200–525	9	-18.9	3		
9R-1,	104.5-106.5	155.875	32	Vesicular/amygdaloidal aphyric basalt	WWU	TH	220-450	6	-21.9	4.9	-21.1	6.1
9R-2,	95–98	155.78	32	Vesicular/amygdaloidal aphyric basalt	Shipboard	TH	300–450	5	-13.4	3.3		
10R-1,	21.5–23.5	158.42	34	Aphyric amygdaloidal basalt	Shipboard	AF	10–100	11	-20.8	3.6		

10R-1,	40-42	158.6	34	Aphyric amygdaloidal basalt	WWU	AF	10-50	9	-26.9	1.1	-26.9	1
10R-2,	75-77	158.74	35	Aphyric amygdaloidal basalt	WWU	TH	310-440	4	-26.5	6	-26.2	6.4
11R-1,	35–37	163.35	36	Aphyric pillow basalt	Shipboard	TH	300–450	6	-17.7	6.2		
11R-1,	97-99	163.97	37	Aphyric pillow basalt	WWU	AF	15-55	9	-16.1	1.8	-15.8	1.8
13R-1,	5-7	172.55	37	Aphyric pillow basalt	WWU	AF	25-50	6	-5.9	2.9	-4	1.7
13R-1,	76–78	173.26	38	Aphyric amygdaloidal pillow basalt	Shipboard	TH	300–500	8	-21.5	3		
13R-2,	38–41	174.15	39	Aphyric amygdaloidal pillow basalt	Shipboard	AF	10–100	11	-15.7	1.6		
13R-2,	59-61	174.36	40	Aphyric amygdaloidal pillow basalt	WWU	AF	20-55	10	-29.1	1.3	-29.2	1.3
14R-1,	14–16	177.54	40	Aphyric amygdaloidal pillow basalt	Shipboard	TH	300–500	7	-22.3	1.6		
14R-1,	136-138	178.76	45	Aphyric amygdaloidal basalt	WWU	TH	400-540	7	-26.5	4	-26.2	4.3
14R-2,	32–34	179.16	46	Aphyric amygdaloidal basalt	Shipboard	TH	100–525	11	-24.1	1.7		
14R-2,	121–123	180.05	47	Aphyric amygdaloidal basalt	Shipboard	TH	100–475	9	-24.3	2.2		
15R-1,	6–9	182.26	50	Aphyric amygdaloidal basalt	Shipboard	AF	10-80	10	-17.2	0.7		
16R-1,	78-80	187.78	52	Aphyric amygdaloidal basalt	WWU	AF	25-55	7	-23.1	2.9	-24	1.7
16R-2,	35-37	188.31	54	Aphyric amygdaloidal basalt	WWU	TH	310-450	4	-20.5	0.7	-20.6	0.9
16R-2,	89–91	188.85	56	Aphyric amygdaloidal basalt	Shipboard	TH	300–525	9	-31.8	3.4		

Core/sec= Core and section, Int= Interval of the section, Depth=mbsf, Unit#= flow unit #, Treat = demagnetization treatment type, AF= Alternating Field demagnetization (mT), TH= Thermal demagnetization (°C), N= # of points in used in principle component calculation, Steps= Demagnetization steps used for principle component calculation, Inc= Inclination of primary magnetization, Dec= declination of primary magnetization, MAD= Maximum angular deviation (°), Anc = values determined with PCA solution anchored to origin.

Table 1.2. Site U1347 discrete sample paleomagnetic results.

Core/sect	Int	Depth	Unit #	Lithologic Units	Location	Treat	Steps	N	Inc (Anc)	MAD (Anc)	Inc	MAD
12R-1,	20.5–22.5	159.9	4	Aphyric Basalt	Shipboard	AF	12–100	10	-2.3	4.9		
12R-1,	33–35	159.93	4	Aphyric Basalt	Shipboard	TH	475–600	6	18.8	12.3		
12R-1,	69–71	160.29	4	Aphyric Basalt	Shipboard	AF	12–100	10	-14.2	1.2		
12R-1,	78–80	160.38	4	Aphyric Basalt	Shipboard	AF	25–100	7	-1.40	3.7		
12R-1,	93-95	160.53	4	Aphyric Basalt	WWU	TH	310-520	7	54.1	4.4	56.3	3.2
12R-1,	104-106	160.64	4	Aphyric Basalt	WWU	AF	25-60	7	4.4	2.9	4.4	2.9
12R-2,	2-4	160.96	4	Aphyric Basalt	WWU	AF	20-65	10	4.1	3.3	3.8	2.9
12R-2,	9–11	161.03	4	Aphyric Basalt	Shipboard	AF	10–100	11	7.9	3.3		
12R-2,	42–44	161.36	4	Aphyric Basalt	Shipboard	TH	400–600	10	34	4.7		
12R-2,	81-83	161.75	4	Aphyric Basalt	WWU	TH	480-550	6	4.6	6.2	4.6	6.2
13R-1,	7-9	167.07	4	Aphyric Basalt	WWU	TH	310-520	7	42	7.5	46.6	3.6
13R-1,	24–26	167.24	4	Aphyric Basalt	Shipboard	TH	500–600	5	26.1	5.8		
13R-2,	14-16	168.63	4	Aphyric Basalt	WWU	AF	20-60	8	13.7	3.5	15.5	3.4
13R-2,	90–92	169.39	4	Aphyric Basalt	Shipboard	TH	500–600	5	50.2	5.7		

13R-3,	23-25	170.05	4	Aphyric Basalt	WWU	TH	360-520	6	18.4	6.8	18.5	9.6
13R-4,	2–4	170.96	4	Aphyric Basalt	Shipboard	AF	15–120	11	23	2.5		
13R-6,	13–15	172.95	4	Aphyric Basalt	Shipboard	TH	500–600	5	37.5	8.8		
13R-6,	132-136	174.14	4	Aphyric Basalt	WWU	AF	40-110	9	18.5	3.2	17.5	3.5
14R-1,	51-53	177.11	5	Amygdaloidal Basalt	WWU	AF	30-65	8	13.3	5.1	14.0	6.8
14R-1,	84-86	177.44	5	Amygdaloidal Basalt	WWU	TH	360-550	9	14.3	11.2	14.5	13.6
14R-1,	145–147	178.05	5	Amygdaloidal Basalt	Shipboard	TH	350–600	10	23.3	11		
14R-2,	110-112	179.17	5	Amygdaloidal Basalt	WWU	TH	310-520	7	13.8	1.4	13.8	1.5
15R-1,	13–15	186.33	5	Amygdaloidal Basalt	Shipboard	TH	500–600	5	26.7	5.5		
15R-2,	15-17	187.62	7	Amygdaloidal Basalt	WWU	AF	20-80	10	23.7	1.2	23.6	1.3
16R-1,	21-23	195.01	9	Amygdaloidal Basalt	WWU	TH	360-520	6	37.3	4.2	35.4	5.7
16R-1,	89–91	195.69	9	Amygdaloidal Basalt	Shipboard	TH	500–600	5	39.1	7.3		
16R-2,	14-16	196.44	9	Amygdaloidal Basalt	WWU	AF	30-70	7	18.6	4.2	18.3	4.8
16R-3,	29-31	198.07	9	Amygdaloidal Basalt	WWU	TH	280-450	5	64.3	6.4	68.2	4.9
16R-4,	10–12	198.37	9	Amygdaloidal Basalt	Shipboard	TH	475–600	6	3.2	27.1		
16R-5,	107–109	200.65	9	Amygdaloidal Basalt	Shipboard	AF	20–100	8	19.3	1.4		
16R-5,	116-118	200.74	9	Amygdaloidal Basalt	WWU	AF	25-60	7	13.2	3.3	13.1	4.0
17R-2,	54–56	206.37	11	Plagioclase Phyric Basalt	Shipboard	TH	425–600	8	15.6	4.5		
17R-2,	94-96	206.77	11	Plagioclase Phyric Basalt	WWU	TH	310-520	7	15.1	3	15.4	3.4

17R-3,	86-88	208.15	11	Plagioclase Phyric Basalt	WWU	AF	20-70	9	18	1.4	18.1	1.4
17R-3,	107–109	208.36	11	Plagioclase Phyric Basalt	Shipboard	TH	500–600	5	16	4.7		
18R-1,	44–46	214.44	11	Plagioclase Phyric Basalt	Shipboard	AF	10–100	11	10.2	4.3		
18R-3,	75–77	217.34	11	Plagioclase Phyric Basalt	Shipboard	AF	10–100	11	12.9	1.1		
18R-3,	143-145	218.01	13	Aphyric Amygdaloidal Basalt	WWU	TH	280-450	5	33	5.4	27.3	4.6
18R-4,	54-56	218.58	14	Aphyric Amygdaloidal Basalt	WWU	AF	35-120	11	-2	1.4	-2.1	1.5
18R-5,	66-68	220.12	17	Sparsel Plagioclase-phyric Basalt	WWU	TH	280-450	5	9.9	2.1	10.9	2.3
18R-5,	82–84	220.28	17	Sparsel Plagioclase-phyric Basalt	Shipboard	TH	400–550	7	24.2	11.8		
18R-6,	34-36	221.24	19	Sparsel Plagioclase-phyric Basalt	WWU	AF	30-100	10	12.5	1.9	12.6	2.2
19R-1,	32–34	223.92	20	Aphyric Basalt	Shipboard	AF	15–80	8	20.8	9		
19R-1,	117-119	224.77	22	Aphyric Basalt	WWU	TH	280-450	6	10.3	2.6	10.9	4.1
19R-2,	100-102	225.88	26	Aphyric Basalt	WWU	AF	25-120	13	4.2	1.8	4.3	1.8
19R-3,	14-16	226.44	26	Aphyric Basalt	WWU	TH	280-450	5	10	2.4	11.8	3.0
19R-4,	8–10	227.7	29	Aphyric Basalt	Shipboard	TH	375–600	10	22.3	8.3		
19R-4,	20-22	227.82	29	Aphyric Basalt	WWU	AF	35-100	9	0.9	1.1	1.2	1.3
20R-1,	22-24	233.42	30	Plagioclase Phyric Basalt	WWU	AF	25-100	11	8.7	2.5	8.8	2.7
20R-2,	44-46	235.08	33	Plagioclase Phyric Basalt	WWU	TH	280-450	5	24.3	2.4	25.9	2.1

20R-3,	5-7	235.9	33	Plagioclase Phyric Basalt	WWU	AF	25-100	11	5.5	2.7	5.8	3.0
20R-3,	46–48	236.31	34	Plagioclase Phyric Basalt	Shipboard	AF	25–100	7	3.8	3.9		
20R-3,	118–120	237.03	34	Plagioclase Phyric Basalt	Shipboard	TH	200–600	14	46.3	6.1		
21R-3,	72–74	245.21	37	Plagioclase Phyric Basalt	Shipboard	TH	300–500	9	5.9	5.9		
21R-3,	14–16	247.39	37	Plagioclase Phyric Basalt	Shipboard	AF	10–100	11	26.6	1.5		
21R-4,	12-14	246.11	37	Plagioclase Phyric Basalt	WWU	TH	310-450	4	25.8	3.8	33.2	2.6
21R-4,	121–123	253.61	40	Aphyric Basalt	Shipboard	AF	12–60	8	24.3	1.2		
21R-5,	65-67	247.9	41	Aphyric Basalt	WWU	AF	30-50	5	18.8	8.5	15.3	9.2
22R-1,	51-53	252.91	41	Aphyric Basalt	WWU	TH	280-450	5	35.8	3.5	37.1	4.5
22R-2,	74-76	254.6	42	Amygdaloidal Basalt	WWU	AF	15-45	7	14.7	1	14.8	1.0
22R-2,	95–97	254.81	42	Amygdaloidal Basalt	Shipboard	TH	475–600	6	17.5	12.2		
22R-3,	70–72	255.97	42	Amygdaloidal Basalt	Shipboard	TH	475–600	6	25	17.9		
22R-4,	12–14	256.84	42	Amygdaloidal Basalt	Shipboard	TH	150–600	10	43.8	5.6		
22R-4,	135–137	258.06	42	Amygdaloidal Basalt	Shipboard	AF	10–80	10	24.2	0.9		
22R-5,	9-11	258.19	42	Amygdaloidal Basalt	WWU	AF	25-60	8	21.8	6.5	23.8	6.7
22R-5,	61-63	258.71	44	Plagioclase Phyric Basalt	WWU	TH	500-550	5	11.8	5	12.6	9.5
22R-5,	86–88	258.96	46	Plagioclase Phyric Basalt	Shipboard	TH	200–600	13	9.7	6.2		
23R-2,	76–78	262.98	48	Sparsel Plagioclase-phyric Basalt	Shipboard	TH	425–600	8	15.9	7		
23R-2,	134-136	263.56	48	Sparsel Plagioclase-phyric Basalt	WWU	TH	220-450	5	15.2	2.6	15.9	2.8

23R-3,	9–11	263.72	49	Sparsel Plagioclase-phyric Basalt	Shipboard	TH	200–600	13	29.3	3		
23R-3,	34–36	265.38	49	Sparsel Plagioclase-phyric Basalt	Shipboard	AF	20–120	9	13	3.5		
23R-3,	62-64	264.26	50	Sparsel Plagioclase-phyric Basalt	WWU	AF	30-80	11	3.8	1.7	3.9	1.7
23R-4,	103-105	266.07	53	Sparsel Plagioclase-phyric Basalt	WWU	TH	280-450	5	10.7	3.4	13.2	5.1
23R-6,	96–98	267.79	53	Sparsel Plagioclase-phyric Basalt	Shipboard	TH	450–600	7	18.7	5.7		
24R-1,	34–36	271.94	53	Sparsel Plagioclase-phyric Basalt	Shipboard	TH	350–600	11	39.7	19		
24R-3,	61–63	274.7	53	Sparsel Plagioclase-phyric Basalt	Shipboard	AF	10–100	11	8	1.6		
24R-3,	136-138	275.45	56	Sparsel Plagioclase-phyric Basalt	WWU	AF	40-75	8	0.8	2.4	.7	3.0
24R-5,	41–43	277.38	57	Sparsel Plagioclase-phyric Basalt	Shipboard	AF	20–140	9	16.4	2.5		
24R-5,	49-51	277.46	57	Sparsel Plagioclase-phyric Basalt	WWU	TH	280-450	5	21.7	6.6	20.6	6.8
24R-6,	30–32	278.45	60	Sparsel Plagioclase-phyric Basalt	Shipboard	AF	15–100	9	13.6	1.7		
24R-6,	69-71	278.84	60	Sparsel Plagioclase-phyric Basalt	WWU	AF	30-55	6	15.4	7.8	18.4	7.0
24R-6,	90–92	279.05	60	Sparsel Plagioclase-phyric Basalt	Shipboard	TH	200–600	10	32.3	6.4		
24R-7,	45–47	279.81	61	Sparsel Plagioclase-phyric	Shipboard	TH	450–600	7	-7.1	0.7		

				Basalt								
24R-8,	24–26	280.64	62	Sparsel Plagioclase-phyric Basalt	Shipboard	TH	400–600	9	30.2	5.2		
24R-8,	65-67	281.05	64	Sparsel Plagioclase-phyric Basalt	WWU	TH	360-550	9	13.5	14.9	14.3	16.2
24R-8,	127-129	281.67	65	Sparsel Plagioclase-phyric Basalt	WWU	AF	25-60	8	7.7	2.7	7.8	3.0
25R-1,	44–46	281.64	65	Sparsel Plagioclase-phyric Basalt	Shipboard	AF	15–100	9	13.9	2.9		
25R-1,	84-86	282.04	65	Sparsel Plagioclase-phyric Basalt	WWU	AF	45-80	8	1.5	5.3	2.2	7.4
25R-2,	81–83	283.31	67	Sparsel Plagioclase-phyric Basalt	Shipboard	TH	350–575	10	43.2	8.6		
25R-3,	65–67	284.53	68	Sparsel Plagioclase-phyric Basalt	Shipboard	AF	20–80	7	6.2	4.3		
25R-4,	102–104	286.4	69	Sparsel Plagioclase-phyric Basalt	Shipboard	TH	450–600	9	35.3	3.9		
25R-4,	125-127	286.63	70	Sparsel Plagioclase-phyric Basalt	WWU	AF	25-75	11	5.2	1.3	5.3	1.2
25R-5,	59–61	287.34	71	Sparsel Plagioclase-phyric Basalt	Shipboard	TH	300–600	13	48.9	4.6		
26R-1,	58–60	291.28	79	Sparsel Plagioclase-phyric Basalt	Shipboard	TH	475–600	6	-10.4	12.8		
26R-1,	103-105	291.73	79	Sparsel Plagioclase-phyric Basalt	WWU	TH	310-450	4	8	2.3	9.3	3.3
26R-2,	29-31	292.49	81	Sparsel Plagioclase-phyric Basalt	WWU	AF	25-65	9	-4	2.9	-2.6	3.1

26R-2,	84–86	293.04	81	Sparsel Plagioclase-phyric Basalt	Shipboard	TH	150–350	6	80.4	4.6		
27R-2,	23–25	294.74	81	Sparsel Plagioclase-phyric Basalt	Shipboard	AF	20–80	7	14.1	5.1		
27R-2,	78-80	295.29	81	Sparsel Plagioclase-phyric Basalt	WWU	AF	20-65	10	10.3	4.2	7.1	3.4
27R-3,	8-10	295.69	81	Sparsel Plagioclase-phyric Basalt	WWU	TH	360-450	3	1.4	7.9	43.5	26.3
27R-3,	65-67	296.24	81	Sparsel Plagioclase-phyric Basalt	WWU	AF	30-50	5	-7.9	3.4	-3.2	14.2
27R-4,	63–65	297.1	81	Sparsel Plagioclase-phyric Basalt	Shipboard	TH	450–600	9	-38.7	44.8		
27R-5,	4-6	297.9	81	Sparsel Plagioclase-phyric Basalt	WWU	AF	25-65	9	-1.7	2.8	-1.0	3.2
27R-5,	120-122	299.06	81	Sparsel Plagioclase-phyric Basalt	WWU	TH	120-310	5	88.5	1.6	88.3	1.5
27R-6,	22-24	299.37	81	Sparsel Plagioclase-phyric Basalt	WWU	AF	15-45	7	21.4	10.6	24.1	11.0
27R-6,	123–125	300.38	81	Sparsel Plagioclase-phyric Basalt	Shipboard	TH	150–325	5	55.6	7.2		
28R-1,	8-10	300.48	81	Sparsel Plagioclase-phyric Basalt	WWU	TH	220-450	6	80.3	2.2	81.0	1.4
28R-1,	67–69	301.07	81	Sparsel Plagioclase-phyric Basalt	Shipboard	AF	12–60	8	79.3	4.5		
28R-2,	28-30	301.92	81	Sparsel Plagioclase-phyric Basalt	WWU	AF	20-45	6	19.9	7.1	20.9	7.7
28R-3,	44–46	303.39	81	Sparsel Plagioclase-phyric	Shipboard	TH	450–550	7	-6.9	14.1		

				Basalt								
28R-5,	16–18	305.61	81	Sparsel Plagioclase-phyric Basalt	Shipboard	AF	20–50	5	26.5	9.5		
28R-6,	49–51	307.15	81	Sparsel Plagioclase-phyric Basalt	Shipboard	TH	425–600	8	-75.7	22.6		
28R-7,	13-15	308.11	81	Sparsel Plagioclase-phyric Basalt	WWU	TH	180-310	6	82.1	1.9	82.2	1.7
28R-8,	80–82	310.04	81	Sparsel Plagioclase-phyric Basalt	Shipboard	AF	7–60	10	77.8	10.2		
29R-1,	23–25	310.13	81	Sparsel Plagioclase-phyric Basalt	Shipboard	TH	350–600	11	25.4	25.1		
29R-3,	68-70	312.89	81	Sparsel Plagioclase-phyric Basalt	WWU	AF	15-40	6	64.2	4.6	65.4	3.5
29R-4,	57–59	314.22	81	Sparsel Plagioclase-phyric Basalt	Shipboard	TH	150–325	5	63.4	4.1		
29R-4,	142–144	315.07	82	Sparsel Plagioclase-phyric Basalt	Shipboard	TH	350–600	11	30.7	2.6		
29R-5,	86-88	316.01	82	Sparsel Plagioclase-phyric Basalt	WWU	AF	35-55	5	9.3	7.4	5.3	10.3

Core/sec= Core and section, Int= Interval of the section, Depth=mbsf, Unit#= flow unit #, Treat = demagnetization treatment type, AF= Alternating Field demagnetization (mT), TH= Thermal demagnetization (°C), N= # of points in used in principle component calculation, Steps= Demagnetization steps used for principle component calculation, Inc= Inclination of primary magnetization, Dec= declination of primary magnetization, MAD= Maximum angular deviation (°), Anc = values determined with PCA solution anchored to origin.

Table 1.3. Site U1350 discrete sample paleomagnetic results.

Core/sect	Int	Depth	Unit #	Lithologic Units	Location	Treat	Steps	N	Inc (Anc)	MAD (Anc)	Inc	MAD
7R-1,	53–55	153.13	2	Aphyric Basalt Flow	Shipboard	TH	150–550	14	-9.5	2.6		
7R-1,	104-106	153.64	2	Aphyric Basalt Flow	WWU	TH	280-530	7	-1.1	2.8	-.5	3.0
7R-2,	21-23	154.25	2	Aphyric Basalt Flow	WWU	AF	15-40	6	5.8	3	6.3	3.1
8R-1,	18–20	155.48	4	Aphyric Basalt Flow	Shipboard	TH	325–550	10	-30.9	9.9		
8R-1,	63-65	155.93	4	Aphyric Basalt Flow	WWU	TH	400-530	5	-2	2.8	-3.3	3.4
8R-2,	4-6	156.8	6	Massive Basalt	WWU	AF	25-55	7	-6.7	1.7	-6.5	1.8
8R-3,	4-6	158.11	7	Massive Basalt	WWU	AF	25-45	5	9.1	1.9	9.0	2.4
8R-3,	85–87	158.92	7	Massive Basalt	Shipboard	AF	7–100	12	-1.3	1.6		
9R-1,	58-60	162.88	9	Aphyric vesicular basalt	WWU	TH	220-500	8	-8	2.8	-7.8	3.1
9R-2,	69–71	164.04	9	Aphyric vesicular basalt	Shipboard	TH	150–550	14	10	6.3		
9R-3,	51-53	164.93	9	Aphyric vesicular basalt	WWU	AF	15-60	10	-4.4	1.6	-4.4	1.7
9R-4,	89–91	166.62	10	Aphyric massive basalt	Shipboard	AF	10–100	11	-2.8	0.9		
9R-5,	9-11	167.07	10	Aphyric massive basalt	WWU	TH	220-500	8	-0.3	3.3	0.0	3.8
9R-6,	4–6	168.33	10	Aphyric massive basalt	Shipboard	TH	100–500	13	31.2	9.3		
9R-6,	67-69	168.96	10	Aphyric massive basalt	WWU	AF	20-60	9	1	7.3	.5	8.3

10R-1,	21-23	172.11	11	Aphyric massive basalt	WWU	TH	280-440	5	35.2	8.9	39.9	4.2
10R-2,	38-40	173.73	12	Aphyric massive basalt	WWU	AF	15-50	8	2.5	1.0	2.5	1.0
11R-1,	51–53	182.01	12	Aphyric massive basalt	Shipboard	AF	10–80	10	0.5	0.6		
11R-1,	128-130	182.78	13	Aphyric massive basalt	WWU	TH	440-530	4	-3.6	1.8	-4.7	5.2
11R-2,	14-16	183.16	14	Aphyric massive basalt	WWU	AF	20-45	6	-2.4	2.6	-2.8	2.7
11R-2,	77–79	183.79	14	Aphyric massive basalt	Shipboard	TH	150–550	14	7.6	6.2		
12R-1,	8-10	191.18	14	Aphyric massive basalt	WWU	AF	25-50	6	18.3	2.7	17.5	2.6
12R-1,	50–52	191.6	15	Plagioclase phryic massive basalt	Shipboard	AF	10–80	11	27	1.1		
13R-1,	50–52	196.4	16	Plagioclase phryic massive basalt	Shipboard	TH	150–550	14	43	4.9		
13R-1,	100-102	196.9	16	Plagioclase phryic massive basalt	WWU	TH	310-500	6	-19.7	5.2	-19.1	5.6
13R-2,	55-57	197.88	17	Plagioclase phryic massive basalt	WWU	AF	30-50	5	7.3	3.9	7.3	4.7
14R-1,	52-54	201.22	20	plagioclase phryic massive basalt	WWU	AF	35-65	7	2.5	2	2.0	1.8
14R-1,	78–80	201.48	20	plagioclase phryic massive basalt	Shipboard	TH	300–550	9	27.3	9.5		
14R-2,	9–11	201.96	20	plagioclase phryic massive basalt	Shipboard	AF	10–80	10	-1	1.3		
14R-2,	21-23	202.08	20	plagioclase phryic massive basalt	WWU	TH	440-550	7	-1.2	1	-1.0	1.1
15R-1,	53-55	206.03	25	Plagioclase phryic massive	WWU	AF	25-50	6	-3.3	2.7	-4.1	2.7

				basalt								
15R-1,	101-103	206.51	25	Plagioclase phryic massive basalt	WWU	TH	280-440	5	38.1	5.3	37.8	6.1
16R-1,	35–37	210.65	27	Plagioclase phryic massive basalt	Shipboard	TH	300–575	12	-2.3	2		
16R-2,	5-7	211.07	27	Plagioclase phryic massive basalt	WWU	TH	310-530	7	-6	1.9	-5.3	2.2
16R-2,	72–74	211.74	27	Plagioclase phryic massive basalt	Shipboard	AF	15–100	10	-3.5	1.8		
16R-3,	105-107	213.01	28	Aphyric massive basalt	WWU	AF	25-55	7	-2.5	1.7	-2.4	1.9
17R-1,	138-140	221.28	30	Phyric massive basalt	WWU	TH	360-530	6	10.2	1.3	10.6	1.5
17R-2,	34–36	221.74	30	Phyric massive basalt	Shipboard	TH	150–575	15	18.3	3.3		
17R-2,	80-82	222.2	30	Phyric massive basalt	WWU	AF	25-45	5	0.4	1.7	0.5	2.0
17R-3,	72–74	223.52	34	Phyric massive basalt	Shipboard	AF	10–80	11	3	0.7		
18R-1,	72-74	230.22	36	Aphyric massive basalt	WWU	TH	280-440	5	24.9	4.1	23.7	4.2
18R-1,	97–99	230.47	36	Aphyric massive basalt	Shipboard	TH	150–575	51	14.8	3.4		
18R-2,	50–52	231.44	37	Aphyric vesicular basalt	Shipboard	AF	7–60	11	14.5	0.9		
18R-2,	73-75	231.67	37	Aphyric vesicular basalt	WWU	AF	30-55	6	11	2.2	10.9	2.2
18R-3,	12-14	232.56	37	Aphyric vesicular basalt	WWU	TH	400-500	4	46.6	4.6	60.6	8.0
18R-3,	60–62	233.04	37	Aphyric vesicular basalt	Shipboard	TH	200–575	14	29	1.9		
19R-1,	68–70	239.78	38	Aphyric massive basalt	Shipboard	AF	10–60	10	6.3	0.7		
19R-1,	119-121	240.29	39	Aphyric massive basalt	WWU	AF	30-55	6	6.3	2.8	6.5	3.4

19R-2,	125-127	241.78	44	Aphyric massive basalt	WWU	TH	280-480	6	16	3.4	16.0	3.8
19R-3,	37-39	242.33	44	Aphyric massive basalt	WWU	AF	25-50	6	-8.1	2.4	-8.7	2.4
20R-1,	31–33	249.01	46	Aphyric massive basalt	Shipboard	TH	350–575	10	13.4	4.5		
20R-1,	65-67	249.35	46	Aphyric massive basalt	WWU	AF	25-50	6	-8	2	-8.0	2.3
20R-1,	95-97	249.65	47	Aphyric massive basalt	WWU	TH	480-550	6	-11.8	6.3	-11.1	8.7
20R-2,	67-69	250.7	49	Aphyric massive basalt	WWU	TH	440-575	6	-5.6	3.3	-5.7	4.2
20R-2,	132-134	251.35	50	Aphyric massive basalt	WWU	AF	25-50	6	-6.3	2.5	-6.6	2.9
20R-3,	4–6	251.44	50	Aphyric massive basalt	Shipboard	AF	7–60	11	-11	1.4		
21R-1,	23-25	258.53	51	Aphyric massive basalt	WWU	TH	360-550	8	1.6	4	0.6	4.6
21R-1,	35–37	258.65	51	Aphyric massive basalt	Shipboard	TH	325–575	11	25.1	3		
21R-1,	137-139	259.67	52	Aphyric massive basalt	WWU	AF	30-50	5	5	1.1	4.9	1.3
21R-2,	67–69	260.47	52	Aphyric massive basalt	Shipboard	AF	7–80	12	7.9	1.1		
21R-2,	135-137	261.15	53	Phyric massive basalt	WWU	TH	440-575	6	16.7	1.2	16.7	1.4
21R-3,	48–50	261.71	53	Phyric massive basalt	Shipboard	TH	250–575	13	18.6	3.5		
21R-3,	64-66	261.87	54	Phyric massive basalt	WWU	AF	25-45	5	14.1	1.6	14.2	1.9
22R-1,	67-69	268.47	57	Aphyric massive basalt	WWU	TH	360-550	7	3.5	5.9	2.6	7.3
22R-2,	68-70	269.54	59	Phyric massive basalt	WWU	TH	360-550	7	1.9	3.2	1.9	3.7
22R-2,	97–99	269.84	59	Phyric massive basalt	Shipboard	AF	12–100	11	-0.3	1.9		
22R-3,	113–115	271.3	62	Phyric massive basalt	Shipboard	TH	150–525	13	22.8	3.3		
22R-4,	87-89	272.43	65	Phyric massive basalt	WWU	TH	360-520	6	4.1	1.6	4.3	1.9

22R-5,	71-73	273.69	69	Phyric massive basalt	WWU	AF	15-55	9	-0.5	1.6	-0.5	1.7
22R-5,	135-137	274.33	70	Phyric massive basalt	WWU	TH	360-540	8	-11.7	1	-11.8	1.2
23R-1,	22-24	277.62	71	Phyric massive basalt	WWU	AF	25-60	8	2.4	2.8	2.0	3.3
23R-1,	78–80	278.18	72	Phyric massive basalt	Shipboard	AF	15–80	9	0.4	2.1		
23R-2,	49–51	279.31	74	Phyric massive basalt	Shipboard	TH	425–575	7	3.6	3.8		
23R-3,	125-127	281.43	78	Phyric massive basalt	WWU	AF	25-50	6	-5.1	1.7	-4.9	1.9
23R-4,	16-18	281.84	79	Phyric massive basalt	WWU	TH	360-520	6	-9.3	1.4	-9.3	1.7
23R-4,	92–94	282.6	81	Phyric massive basalt	Shipboard	AF	10–100	12	-2.5	3.3		
23R-5,	6-8	283.13	81	Phyric massive basalt	WWU	AF	40-65	6	-3.6	3.4	-4.4	2.1
24R-1,	42-44	287.42	84	Phyric massive basalt	WWU	TH	400-520	5	-10	1.2	-10.5	1.2
24R-1,	109–111	288.09	85	Phyric massive basalt	Shipboard	TH	150–550	14	-4.1	1.7		
24R-2,	137-139	289.85	89	Phyric massive basalt	WWU	AF	30-50	5	-7.5	1.9	-7.7	1.7
24R-3,	31–33	290.18	90	Phyric massive basalt	Shipboard	AF	12–80	10	3.8	1		
25R-1,	24–26	296.94	92	Phyric massive basalt	Shipboard	TH	325–550	10	-1.2	2.1		
25R-1,	102-104	297.72	94	Phyric massive basalt	WWU	AF	25-50	6	-3.5	3.1	-3.2	3.4
25R-1,	112-114	297.82	94	Phyric massive basalt	WWU	TH	440-540	6	-14.2	3.6	-14.8	4.1
25R-2,	60-62	298.8	100	Phyric massive basalt	WWU	AF	25-45	5	-6.3	1.6	-6.7	1.1
25R-2,	119–121	299.39	101	Phyric massive basalt	Shipboard	AF	12–80	10	-12	1.1		
25R-3,	83-85	300.53	107	Phyric massive basalt	WWU	TH	360-520	6	-0.4	1.5	0.3	1.4
25R-4,	71–73	301.75	114	Phyric massive basalt	Shipboard	TH	150–550	14	4.9	2.6		

25R-5,	57–59	302.88	119	Phyric massive basalt	Shipboard	AF	10–80	11	-7.5	0.8		
25R-5,	92-93	303.24	120	Phyric massive basalt	WWU	AF	15-45	7	-3.1	1.8	-3.0	1.8
25R-6,	31-33	303.95	124	Phyric massive basalt	WWU	TH	360-520	6	1.1	1.4	1.3	1.2
25R-7,	13–15	304.92	130	Plagioclase phryic massive basalt	Shipboard	TH	150–550	14	-1	1.6		
25R-7,	91-93	305.69	133	Plagioclase phryic massive basalt	WWU	AF	20-45	6	-1.8	1.3	-1.8	1.5
25R-8,	13-15	306.31	138	Phyric massive basalt	WWU	TH	400-520	5	-4.8	2.4	-4.3	2.6
26R-1,	28-30	306.48	141	Phyric massive basalt	WWU	TH	360-520	6	-13.2	3	-13.1	3.4
26R-1,	78–80	306.98	142	Phyric massive basalt	Shipboard	AF	10–80	10	-3.7	1.2		
26R-2,	40-42	308.07	145	Phyric massive basalt	WWU	AF	20-45	6	0	2.2	-0.2	2.3
26R-4,	27–29	310.54	156	Phyric massive basalt	Shipboard	TH	150–550	14	4.7	1.9		
26R-6,	12-14	313.11	170	Phyric massive basalt	WWU	AF	25-45	5	-1.5	1.4	-2.2	0.8
26R-7,	13-15	314.35	176	Phyric massive basalt	WWU	AF	10-45	8	-0.8	1.2	-0.8	1.3
26R-8,	11–13	315.4	181	Phyric massive basalt	Shipboard	TH	150–550	14	4.2	3.3		
26R-8,	43-45	315.72	183	Phyric massive basalt	WWU	AF	15-45	7	-2.2	0.7	-2.2	0.7

Core/sec= Core and section, Int= Interval of the section, Depth=mbsf, Unit#= flow unit #, Treat = demagnetization treatment type, AF= Alternating Field demagnetization (mT), TH= Thermal demagnetization (°C), N= # of points in used in principle component calculation, Steps= Demagnetization steps used for principle component calculation, Inc= Inclination of primary magnetization, Dec= declination of primary magnetization, MAD= Maximum angular deviation (°), Anc = inclination and MAD calculated with PCA anchored to origin.

Table 1.4. Change in magnetic intensity for Site U1346 samples exposed to low temperature.

Sample	NRM (A/m)	Final Treatment (A/m)	Difference (A/m)
324-1346A-10R-1-40	0.7939578	0.8383466	-0.0443888
324-1346A-13R-1-5	5.023386	4.476896	0.54649
324-1346A-14R-2-61	7.284539	7.53081	-0.246271
324-1346A-8R-1-136	2.201227	2.233674	-0.032447

NRM = natural remanent magnetization, Final treatment = magnetization after treatment, Difference= Change in magnetic intensity after low temperature treatment.

Table 1.5. Change in magnetic intensity for Site U1347 samples exposed to low temperature.

Sample	NRM (A/m)	Final Treatment (A/m)	Difference (A/m)
324-1347A-12R-1-104	6.457623	5.589212	0.868411
324-1347A-12R-1-93	10.64612	7.832816	2.813304
324-1347A-12R-2-2	9.301645	7.749846	1.551799
324-1347A-12R-2-81	7.425827	6.582811	0.843016
324-1347A-13R-1-7	28.55399	24.54669	4.0073
324-1347A-13R-2-14	18.1069	15.43503	2.67187
324-1347A-13R-3-23	2.443297	1.75616	0.687137
324-1347A-13R-6-132	6.660135	5.684901	0.975234
324-1347A-14R-1-51	5.346083	5.071538	0.274545
324-1347A-14R-1-84	4.709289	4.065169	0.64412
324-1347A-14R-2-110	12.78436	12.33045	0.45391
324-1347A-15R-2-15	9.015858	8.905195	0.110663
324-1347A-16R-1-21	11.26987	7.752251	3.517619
324-1347A-16R-2-14	2.904789	3.204076	-0.299287
324-1347A-16R-3-29	21.21839	16.06144	5.15695
324-1347A-17R-2-94	8.486825	7.968557	0.518268
324-1347A-17R-3-86	11.31072	11.95533	-0.64461
324-1347A-18R-4-54	14.40937	14.54716	-0.13779
324-1347A-18R-5-66	15.05357	15.12779	-0.07422
324-1347A-19R-3-14	11.05138	10.43994	0.61144
324-1347A-20R-3-5	18.67779	17.79944	0.87835
324-1347A-22R-1-51	6.169935	6.180655	-0.01072
324-1347A-23R-3-62	7.31836	7.324684	-0.006324
324-1347A-24R-3-85	10.50195	10.69873	-0.19678
324-1347A-25R-4-125	5.925217	5.867009	0.058208
324-1347A-27R-1-74	11.75117	10.03269	1.71848

324-1347A-27R-2-78	30.20828	27.10314	3.10514
324-1347A-27R-3-65	36.50219	31.22339	5.2788
324-1347A-27R-3-8	22.35934	18.9618	3.39754
324-1347A-27R-4-21	42.73839	37.46225	5.27614
324-1347A-27R-5-120	40.83969	34.88108	5.95861
324-1347A-27R-5-4	16.10062	13.57387	2.52675
324-1347A-27R-6-22	43.13919	38.71886	4.42033
324-1347A-28R-1-8	47.05337	39.69799	7.35538
324-1347A-28R-2-28	29.97382	21.3394	8.63442
324-1347A-28R-7-13	36.96296	31.47984	5.48312
324-1347A-29R-3-68	40.63422	30.69756	9.93666
324-1347A-29R-4-106	5.137402	3.44652	1.690882
324-1347A-29R-5-86	21.93399	20.89856	1.03543

NRM= natural remanent magnetization, Final treatment = magnetization after treatment, Difference= Change in magnetic intensity after low temperature treatment.

Table 1.6. Change in magnetic intensity for Site U1350 samples exposed to low temperature.

Sample	NRM (A/m)	Final Treatment (A/m)	Difference (A/m)
324-1350A-10R-1-21	2.411866	1.550677	0.861189
324-1350A-10R-2-38	11.40671	10.87379	0.53292
324-1350A-11R-1-128	11.56806	11.24633	0.32173
324-1350A-11R-2-14	8.225491	7.434386	0.791105
324-1350A-12R-1-8	12.942	11.93875	1.00325
324-1350A-13R-1-100	2.660902	2.642366	0.018536
324-1350A-13R-2-55	3.312793	2.976592	0.336201
324-1350A-14R-1-52	9.380261	9.083776	0.296485
324-1350A-14R-2-21	15.53609	15.22137	0.31472
324-1350A-15R-1-101	4.161899	2.483586	1.678313
324-1350A-15R-1-53	10.91826	10.81105	0.10721
324-1350A-16R-2-5	4.97177	4.883144	0.088626
324-1350A-16R-3-105	28.40388	27.63965	0.76423
324-1350A-17R-1-138	7.755056	7.904107	-0.149051
324-1350A-17R-2-80	7.337282	7.192962	0.14432
324-1350A-18R-1-72	7.233298	7.08787	0.145428
324-1350A-18R-2-73	9.623877	9.124878	0.498999
324-1350A-18R-3-12	11.5659	10.93472	0.63118
324-1350A-19R-3-37	7.64713	7.538495	0.108635
324-1350A-25R-2-60	13.6832	14.35444	-0.67124
324-1350A-25R-8-13	8.880822	9.255874	-0.375052
324-1350A-26R-7-13	5.783753	5.813596	-0.029843
324-1350A-7R-1-104	8.251514	7.987822	0.263692
324-1350A-7R-2-21	6.876147	4.708694	2.167453
324-1350A-8R-1-63	5.380948	4.708907	0.672041
324-1350A-8R-2-114	5.542608	4.760651	0.781957

324-1350A-8R-2-4	18.05796	17.79073	0.26723
324-1350A-8R-3-4	6.411388	6.373217	0.038171
324-1350A-9R-1-58	4.343018	3.821636	0.521382
324-1350A-9R-3-51	3.436306	3.27055	0.165756
324-1350A-9R-5-9	1.794046	1.55129	0.242756
324-1350A-9R-6-67	2.235285	1.641615	0.59367

NRM = Natural remanent magnetization; Final treatment = magnetization after treatment, Difference= Change in magnetic intensity after low temperature treatment.

Table 1.7. Sample hysteresis parameters.

Sample	Mrs	Ms	Mrs/Ms	Hcr	Hc	Hcr/Hc
324-1346A-10-1-40	0.0002229	0.00104	0.214327	99.08	73.63	1.345647
324-1346A-10-2-75	0.00004817	0.000794	0.060645	62.85	20.99	2.994283
324-1346A-13-2-59	0.0001591	0.00087	0.182874	178.2	103.3	1.725073
324-1346A-14-1-136	0.0001329	0.001028	0.12928	121.3	53.44	2.269835
324-1347A-22-2-74	0.001471	0.007274	0.202227	114.4	77.23	1.48129
324-1347A-22-5-61	0.001212	0.003515	0.344808	401	293.4	1.366735
324-1347-24-8-65	0.002789	0.007543	0.369747	416	381.2	1.091291
324-1347A-24-8-122	0.0002504	0.001464	0.171038	116.9	72.85	1.604667
324-1350A-22-5-135	0.001937	0.005828	0.332361	393.2	272.7	1.441878
324-1350A-23-2-58	0.0001644	0.001013	0.16229	101.2	63.03	1.605585
324-1350A-25-1-78	0.0003982	0.001855	0.214663	130.7	91.73	1.424834
324-1350A-25-1-112	0.0006395	0.002915	0.219383	284.1	146.5	1.939249

Mrs = saturation remanent magnetization, Ms = saturation magnetization, Hcr = remanent coercivity, Hc = coercivity.

APPENDIX B

FIGURES AND TABLES FOR MANUSCRIPT #2

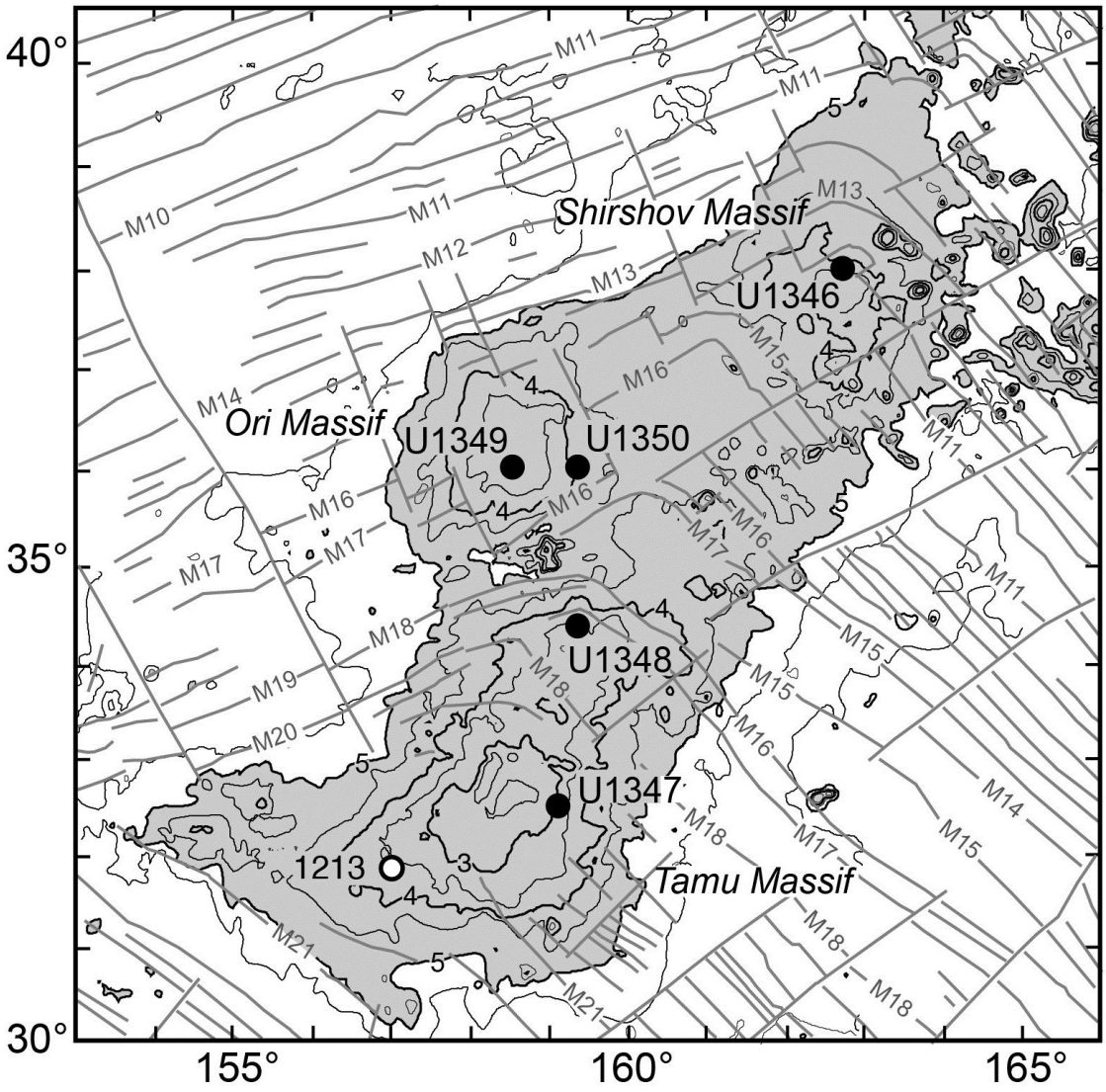

Figure 2.1. Map showing the location of IODP Expedition 324 sites (U1346-U1350) and ODP Site 1213. Bathymetry contours on Shatsky Rise (shaded gray) are shown at 500-m intervals. Gray lines show magnetic lineations and fracture zones from Nakanishi et al. (1999).

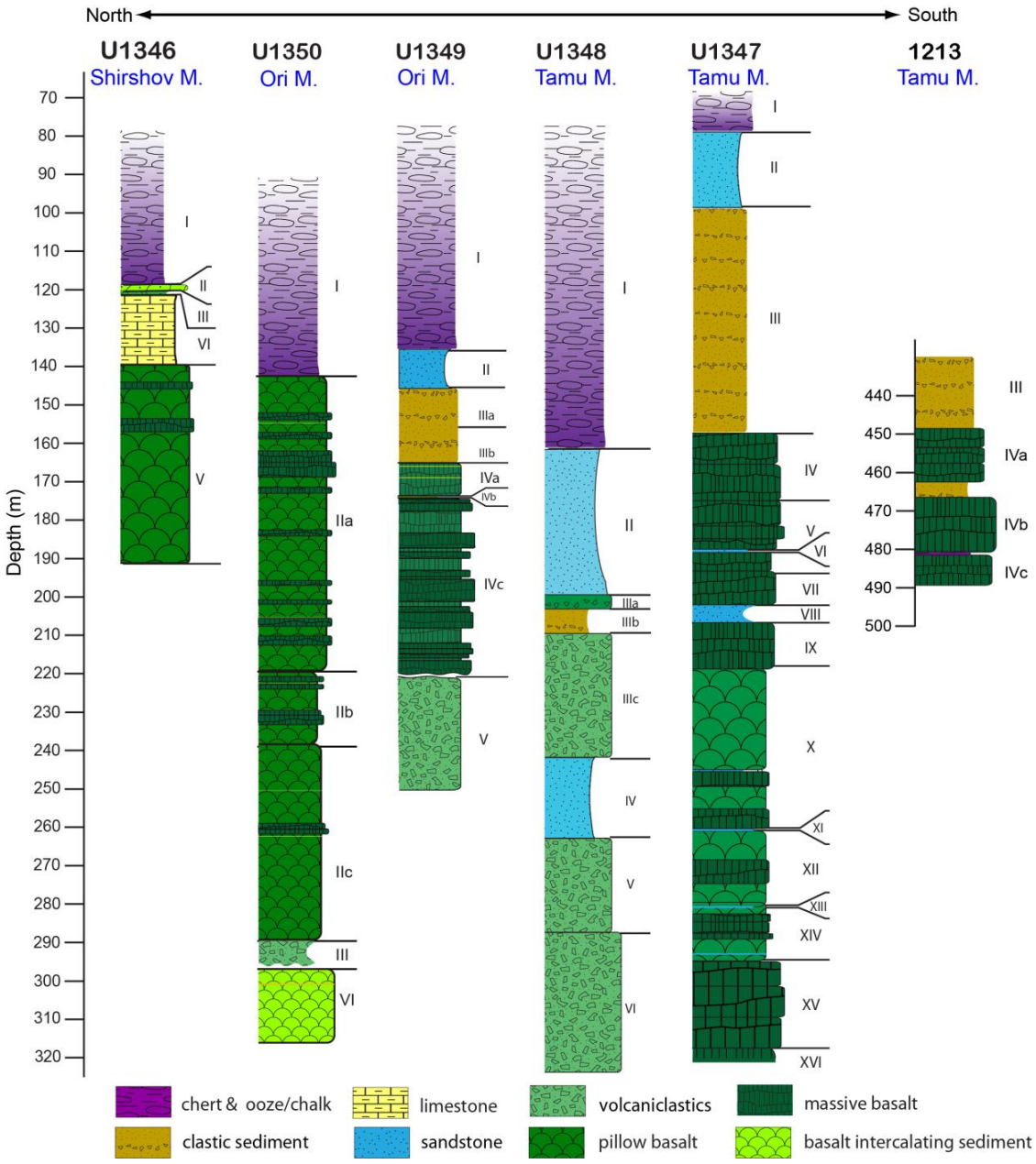

Figure 2.2. Graphic lithology sections for IODP Expedition 324 sites and ODP Site 1213. Green shaded lithologies are igneous in nature. Roman numerals denote units described in the cruise report (Sager et al., 2010).

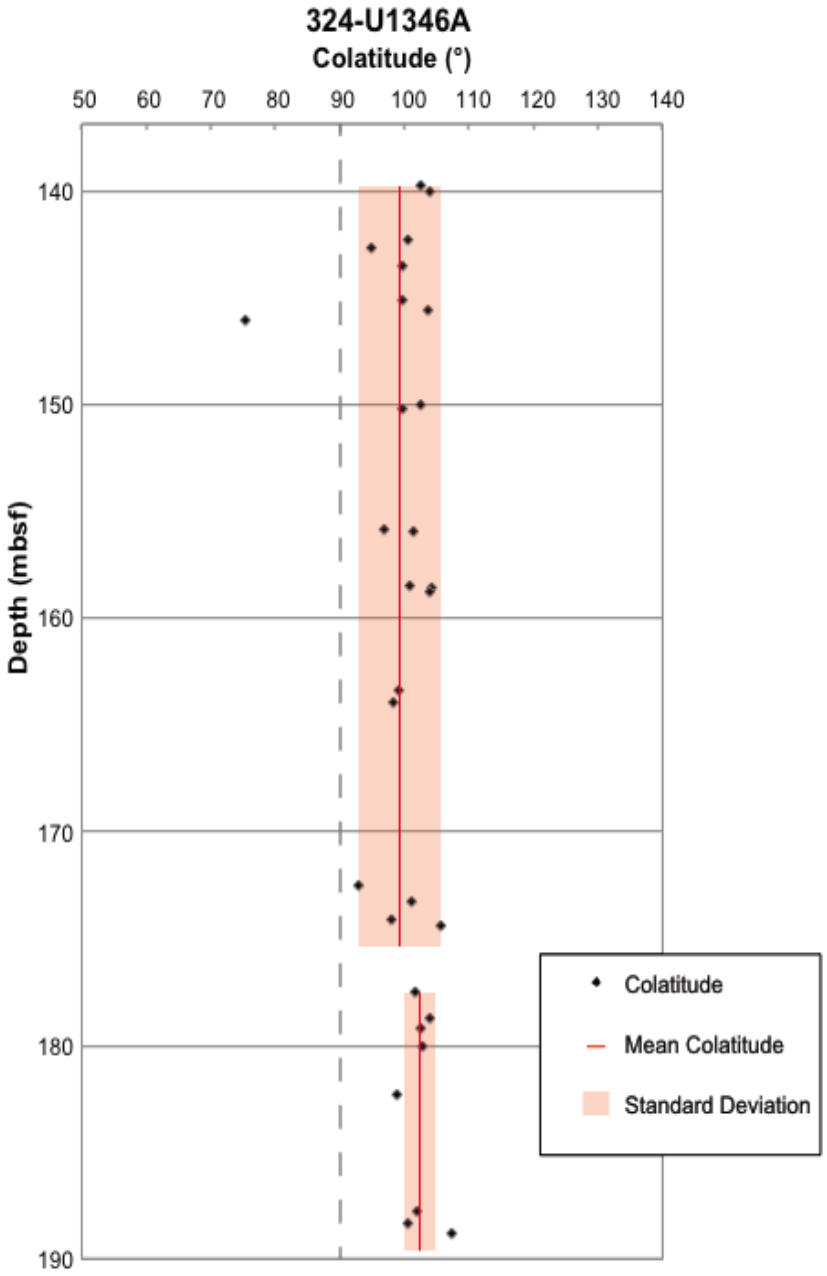

Figure 2.3. Colatitude versus depth (meters below seafloor, mbsf) for Site U1346. Red lines are group mean colatitudes and the shaded areas show the standard error for each mean colatitude. The dashed gray line represents 90° colatitude, the equator. Mean colatitude values are given in Table 2.1.

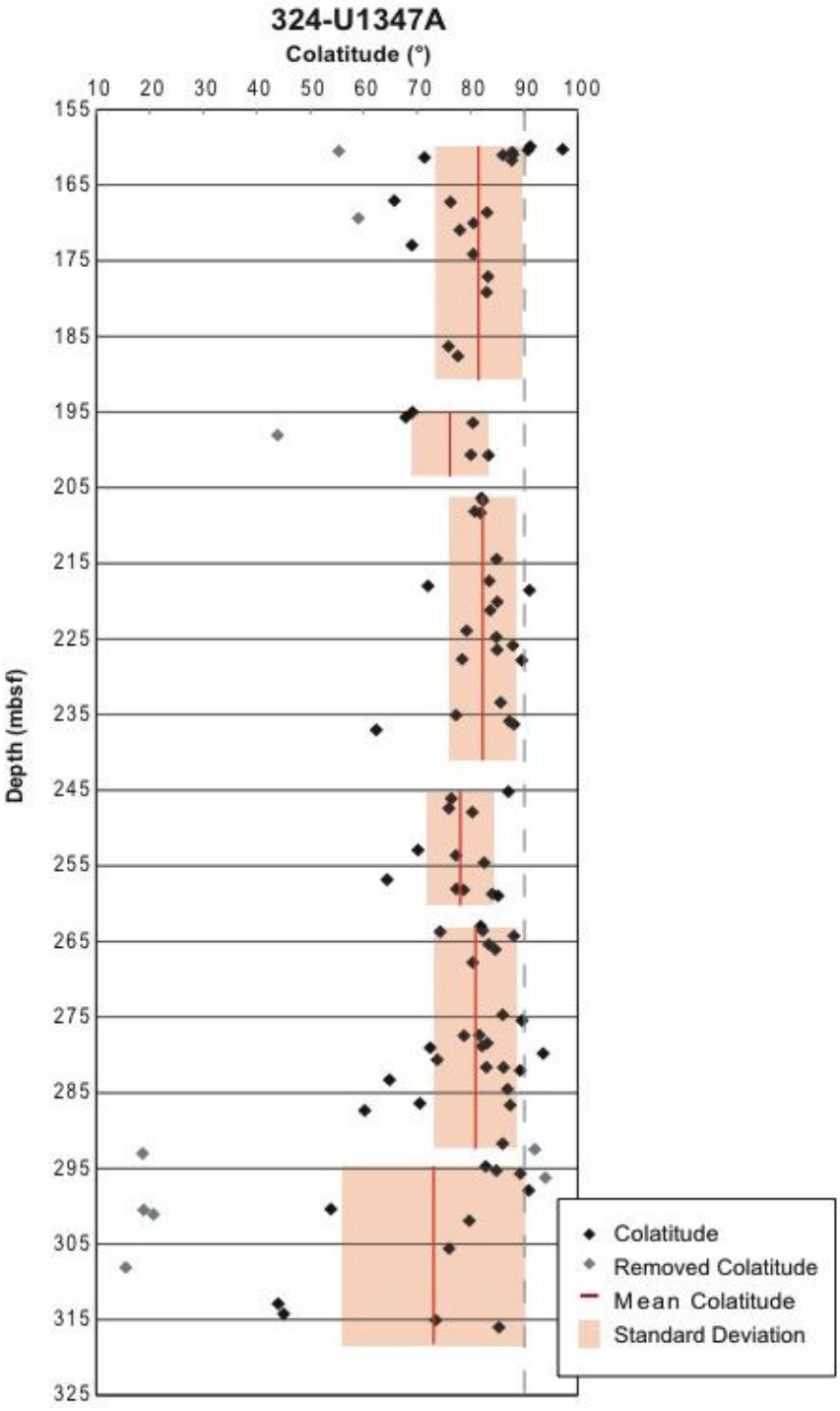

Figure 2.4. Colatitude versus depth for Site U1347. The gray diamonds are colatitudes that were considered outliers (and not used for calculation of the mean). Plot conventions as in Figure 2.3.

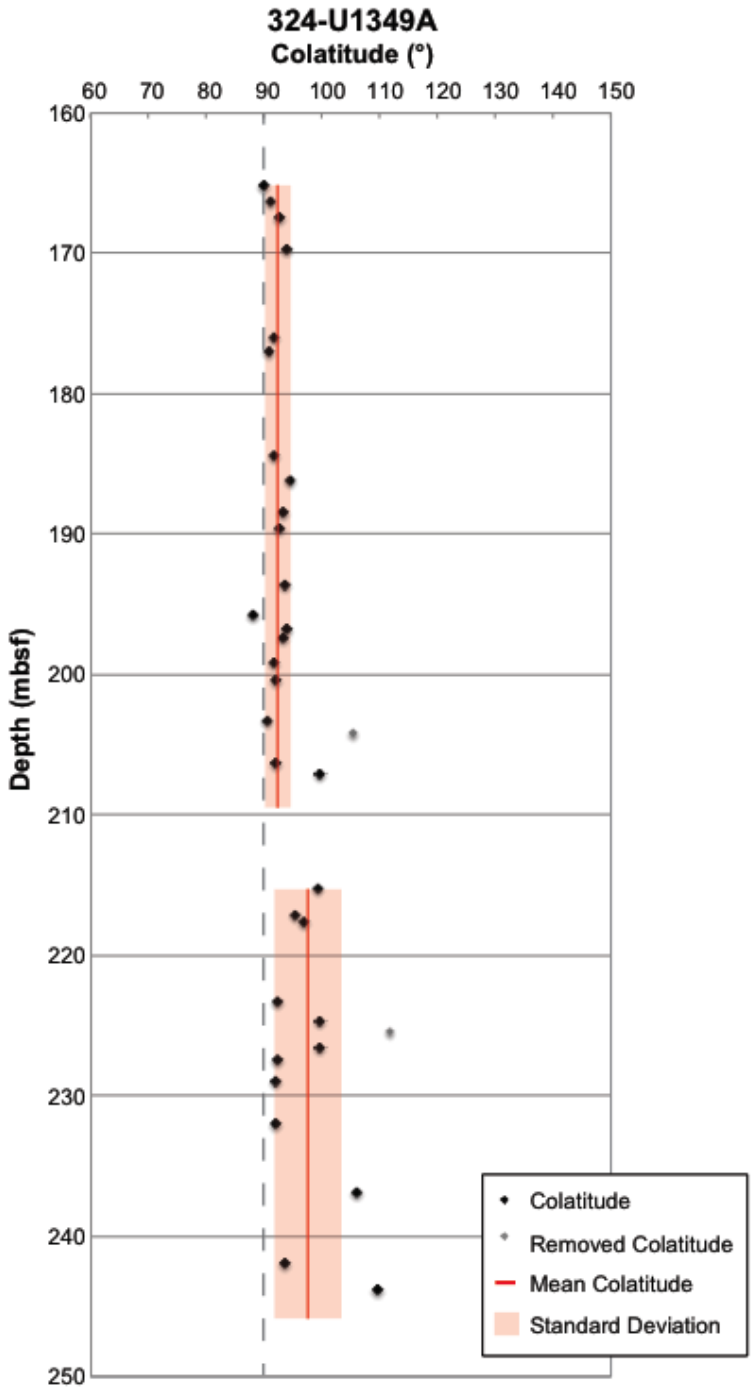

Figure 2.5. Colatitude versus depth for Site U1349. Plot conventions as in Figures 2.3 and 2.4.

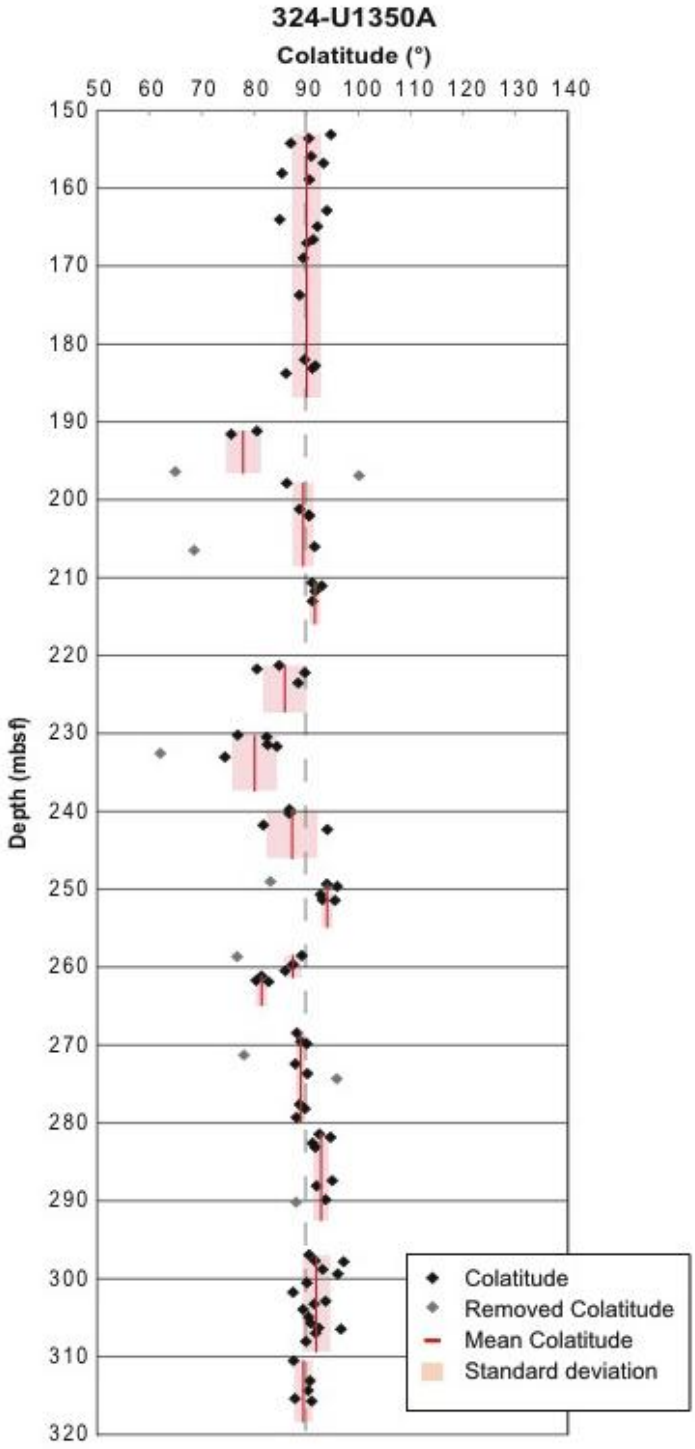

Figure 2.6. Colatitude versus depth for Site U1350. Plot conventions as in Figures 2.3 and 2.4.

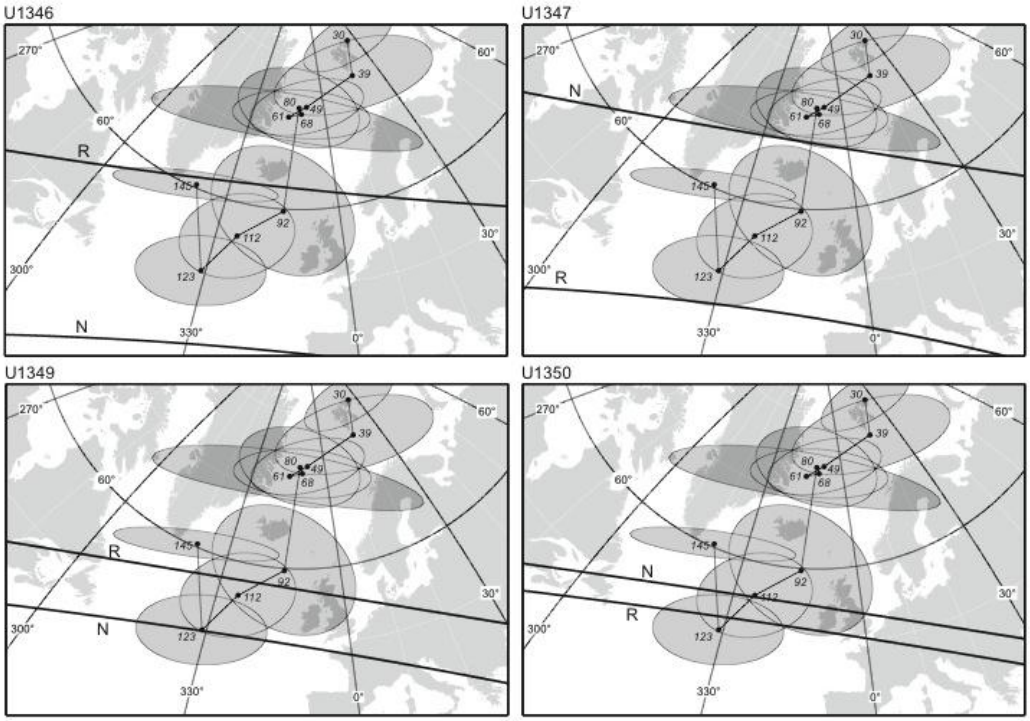

Figure 2.7. Colatitude arcs for Shatsky Rise sites compared to Pacific plate paleomagnetic poles. Pacific plate paleomagnetic poles (Sager, 2006; Beaman et al., 2007) are shown as small, filled circles. Gray ellipses show 95% confidence regions for the poles. Numbers in italics are mean ages for the poles in Ma. Thick arcs labeled N and R show the mean colatitude for the Shatsky Rise site assuming normal and reversed polarity, respectively.

Table 2.1. Statistically distinct unit average colatitudes and site average colatitude.

Site	Unit #	Depth (mbsf)	Average Colatitude(°)	Standard Error(°)	95% Confidence
U1346	1	139.73 – 174.36	99.3	6.3	
U1346	2	177.54 – 188.85	102.4	2.5	
	Average		101.0	10.7	+22.2°/-21.4°
U1347	1	159.9 – 187.62	81.7	8.1	
U1347	2	195.01 – 200.74	76.2	7.1	
U1347	3	206.37 – 237.03	82.5	6.4	
U1347	4	245.21 – 258.96	78.3	6.4	
U1347	5	262.98 – 291.73	81.2	7.9	
U1347	6	294.74 – 316.01	73.2	17.4	
	Average		78.7	13.6	+27.4°/-28.5°
	Average (top 5 units)		79.9	11.9	+24.0°/-24.6°
U1349	1	165.12 – 206.99	92.4	2.3	
U1349	2	215.25 – 243.75	97.4	5.7	
	Average		95.0	10.2	+20.8°/-20.6°
U1350	1	153.13 – 183.79	90.2	2.8	
U1350	2	191.18 – 191.6	78.2	3.5	
U1350	3	197.88 – 206.03	89.6	2.1	
U1350	4	210.65 – 213.01	91.8	0.9	
U1350	5	221.28 – 223.52	85.9	4.1	
U1350	6	230.22 – 233.04	80.2	4.3	
U1350	7	239.78 – 242.33	87.4	5.0	
U1350	8	249.35 – 251.44	94.3	1.4	
U1350	9	258.53 – 260.47	87.6	1.6	
U1350	10	261.15 – 261.87	81.6	1.2	
U1350	11	268.47 – 279.31	89.1	0.9	
U1350	12	281.43 – 289.85	93.0	1.5	
U1350	13	296.94 – 308.07	92.1	2.7	
U1350	14	310.54 – 315.72	89.6	1.7	
	Average		88.4	3.6	+7.7°/-7.7°